



Faculteit Wetenschappen
Departement Fysica

Iterative reconstruction for mobile chest tomosynthesis

Iteratieve reconstructie voor mobiele tomosynthese van de thorax

Proefschrift voorgelegd tot het behalen van de graad van

Doctor in de Wetenschappen

aan de Universiteit Antwerpen, te verdedigen door

Jeroen CANT

Academische Promotor:
Prof. dr. Jan Sijbers

Industriële Promotor:
Gert Behiels (Agfa HealthCare NV)

Antwerpen, 2016

Doctoral committee

Prof. dr. Sandra Van Aert
Prof. dr. Paul M. Parizel
Prof. dr. Jan Sijbers

Other jury members

Prof. dr. Luca Bertolaccini
Prof. dr. Johan Nuyts
Gert Behiels

Contact information:

Jeroen Cant

✉ iMinds-Vision Lab, Dept. of Physics
University of Antwerp (CDE)
Universiteitsplein 1, Building N1
B-2610 Wilrijk, Belgium

☎ +32(0)3 265 22 45

📞 +32 (0)486 69 38 33

✉ jeroen.cant2@uantwerpen.be

🌐 <http://visielab.uantwerpen.be>

Jeroen Cant

Agfa HealthCare IMG R&D
Septestraat 27
B-2640 Mortsel, Belgium

+32(0)3 444 62 62

jeroen.cant@agfa.com

<http://www.agfahealthcare.com>

Table of Contents

Voorwoord	iii
Table of Contents	v
Samenvatting	vii
Summary	ix
1 Introduction	1
1.1 X-ray imaging	3
1.1.1 X-ray generation	3
1.1.2 X-ray interaction with matter	6
1.1.3 X-ray detection	7
1.2 From planigraphy to digital tomosynthesis	10
1.2.1 Planigraphy	11
1.2.2 Tomosynthesis	13
1.2.3 Clinical applications of tomosynthesis	16
1.3 Tomosynthesis reconstruction	16
1.3.1 Deblurring	16
1.3.2 Analytical reconstruction algorithms	19
1.3.3 Iterative reconstruction techniques	19
1.3.4 Challenges in chest tomosynthesis reconstruction	20
References	21
2 Limited view reconstruction	23
2.1 Introduction	24
2.2 Total Variation Regularization	26
2.3 Experiment	27
2.4 Conclusion	28
References	31
3 Continuous tomosynthesis	31
3.1 Introduction	32
3.2 Methods	33
3.3 Experiments	37
3.3.1 Resolution phantoms	37
3.3.2 Forbild phantom	39
3.3.3 Synchrotron measurements	40
3.3.4 Continuous tomosynthesis	40

TABLE OF CONTENTS

3.4	Results	41
3.4.1	Resolution phantoms	41
3.4.2	Forbild phantom	43
3.4.3	Synchrotron measurements	49
3.4.4	Continuous tomosynthesis	51
3.5	Discussion	52
3.6	Conclusion	54
3.7	Linearization of forward projector	54
	References	55
4	Mobile chest tomosynthesis in the ICU	57
4.1	Introduction	58
4.2	Material and methods	60
4.3	Results	64
4.4	Discussion	65
	References	73
5	Geometry parameter estimation	73
5.1	Introduction	74
5.2	Geometric inaccuracies	75
5.3	Method	82
5.3.1	Plane-based raw data redundancy criterion	82
5.3.2	Truncation weighting	84
5.3.3	Robust cost function for linear tube motion	85
5.4	Experiments	86
5.4.1	XCAT simulations	86
5.4.2	Experimental data	87
5.5	Discussion	89
5.6	Conclusion	92
	References	92
6	Conclusions	93
A	List of common abbreviations and symbols	97
	Common symbols	97
B	Scientific contribution	99

Samenvatting

De X-ray van de thorax (CXR) is een van de oudste technieken voor medische beeldvorming. De lage stralingsdosis (rond 0.06 mSv voor een frontale en laterale opname samen) en relatief lage kostprijs ten opzichte van CT of andere technieken maken dat de CXR nog steeds veelvuldig wordt gebruikt als eerste stap in de diagnostische beeldvorming van de patiënt. Niettegenstaande deze voordelen wordt de interpretatie van de CXR echter vaak bemoeilijkt door overlappende anatomie. Aangezien de CXR een projectiebeeld is, kunnen kleine structuren zoals bv. een longnodule gemakkelijk worden gemist door de radioloog, als een rib of ander lichaamsdeel op dezelfde locatie in het beeld worden geprojecteerd.

Tomosynthese van de thorax (CTS) lost dit probleem van *anatomische ruis* op. Bij CTS worden eerst met een gemotoriseerde röntgenbron een klein aantal (bv. 53) frontale X-rays van de thorax genomen vanuit verschillende hoeken, aan een zeer lage stralingsdosis (typisch 1/10de van een gewone frontale opname). Vervolgens worden sectiebeelden berekend, evenwijdig met de vlakke detector. De overlappende anatomie wordt op deze wijze terug gesplitst en verdeeld over de verschillende sectiebeelden, waardoor de detectie van bv. longnodules of andere condities in de thorax gevoelig verbetert ten opzichte van een klassieke CXR.

In dit werk wordt een mobiele variant van CTS bestudeerd, op basis van een draagbare detector en een mobiele röntgenbron die op dit moment reeds worden gebruikt voor een CXR opname aan bed. Mobiele CTS is op dit moment nog niet op de markt, maar zou mogelijk de CXR opnames aan bed kunnen verbeteren voor patiënten die niet eenvoudig kunnen worden getransporteerd naar de radiologieafdeling. Om deze mobiele variant van CTS mogelijk te maken worden in dit werk drie uitdagingen behandeld.

Reconstructie met een klein aantal projecties

Aangezien mobiele CTS kan worden uitgevoerd buiten de radiologieafdeling, werd in een eerste fase onderzocht of het aantal projectiebeelden verder kon worden verlaagd van 53 naar bv. 15 of 10. Bij een lager aantal projectiebeelden zakt het stralingsrisico voor de omringende patiënten en medisch personeel, en wordt de mobiele workflow ook eenvoudiger.

Een reductie van het aantal projecties zorgt echter voor artefacten in de gereconstrueerde beelden. Onderzoek naar het reduceren van deze ringing en streak artefacten resulteerde in ARTIC, een nieuwe methode voor driedimensionale reconstructie waarbij een klein aantal projectiebeelden wordt opgenomen met een continu bewegende en stralende röntgenbron. De beweging wordt vervolgens mee gemodelleerd in het reconstructiealgoritme en leidt tot een lokale verbetering van

SAMENVATTING

de beeldkwaliteit. ARTIC kan worden toegepast op CTS maar bleek ook waardevol voor synchrotron en CT beeldvorming.

Aantonen van klinisch potentieel

De opnametechniek van mobiele CTS aan bed verschilt van een gewone CTS in een röntgenkamer, ten gevolge van het kleiner aantal projecties en de gereduceerde beweging van de röntgenbron. In een tweede fase werd daarom een simulatiestudie opgezet om te onderzoeken of mobiele CTS de patiëntzorg in een Intensieve Zorgenafdeling (InZo) kan verbeteren. Mobiele CTS onderzoeken werden gesimuleerd op basis van CT scans van patiënten in de InZo en vergeleken met gewone CXRs aan bed, die kort daarvoor werden genomen. Ondanks de technische beperkingen van de simulaties, toonde mobiele CTS potentieel voor het detecteren van pneumothorax en andere acute problemen in InZo.

Automatische geometrische calibratie

De algoritmes voor de reconstructie van de sectiebeelden vereisen de exacte locatie van de bron en detector van elk projectiebeeld. De geometrie van een mobiel CTS onderzoek kan echter niet op voorhand worden bepaald met een calibratiefantom zoals bij gewone CTS in de röntgenkamer, aangezien voor mobiele CTS aan bed een draagbare detector en mobiele röntgenbron worden gebruikt. Daarom werd in een derde fase een automatische methode ontwikkeld om de relatieve posities van bron en detector te bepalen, gebaseerd op de informatie in de projectiebeelden zelf.

Samengevat kunnen de technieken uit dit werk worden gebruikt om de kwaliteit van een CTS onderzoek te verbeteren en op termijn leiden tot de ontwikkeling van mobiele CTS, een nieuwe beeldvormingstechniek aan bed die de diagnostische waarde van een thorax röntgenopname aan bed verbetert.

Summary

The chest X-ray exam (CXR) is one of the oldest medical imaging techniques. It offers a quick and relatively cheap first insight into the condition of the patient, with a low radiation dose (around 0.06 mSv). However, the interpretation of the CXR is often complicated by overlapping anatomy. Small structures such as lung nodules can easily be missed by the radiologist if a rib or another body part is projected onto the same location in the image.

Chest tomosynthesis (CTS) solves this problem of anatomical noise. CTS is an X-ray imaging technique in which a small number of low dose chest X-ray images are acquired from different angles, using a motorized X-ray tube. Subsequently, section images are computed parallel to the detector by a reconstruction algorithm. The overlapping anatomy is thereby separated into different section images, which improves the detection of lung nodules and simplifies the detection of various other abnormalities in the chest.

In this work, three challenges were dealt with to create a mobile version of CTS, based on a mobile X-ray unit and a portable flat panel detector, which are currently used for bedside CXR. Mobile CTS is not on the market yet, but might hold potential for improving the bedside CXRs of patients that cannot easily be moved to the X-ray room for a regular tomosynthesis exam.

Challenge 1: reconstruction with a small number of projections

A first challenge that needed to be addressed in order to turn CTS into a mobile imaging technique, was the reduction of the number of projection images. A substantially reduced number of projections simplifies the mobile workflow and reduces the radiation risk for medical staff and other patients. However, a limited number of views is known to cause streaks and ringing artifacts in the reconstructed images. Research into the reduction of these ringing artifacts resulted in ARTIC, a novel approach for image reconstruction in which a limited number of projection images are acquired with a continuously moving and continuously radiating X-ray source. ARTIC can be applied to chest tomosynthesis but has also proven useful in synchrotron and CT imaging.

Challenge 2: assess clinical potential

Secondly, a simulation study was performed to assess if a mobile CTS implementation with a substantially reduced tube travel distance could improve patient care in the Intensive Care Unit (ICU). Mobile CTS exams were simulated from CT scans of patients in the ICU, and compared with CXRs that were taken within a short timeframe. Despite the technical limitations of the simulations, mobile CTS

SUMMARY

shows potential for the detection of pneumothorax and other acute problems in the ICU.

Challenge 3: automatic geometric calibration

Contrary to CTS in the X-ray room, the geometry of the mobile CTS system cannot be calibrated up front with a calibration phantom, as the relative positions of X-ray source and detector vary with each bedside exam. Accurate knowledge of the acquisition geometry is required in order to produce high quality reconstructions, and therefore an automatic method was derived to automatically calibrate the geometry of the bedside CTS, using the information in the projection images.

To conclude, the techniques described in this work can be used to improve the quality of CTS and might lead to the development of mobile CTS, a new bedside imaging technique that improves the diagnostic value of the CXR.

CHAPTER 1. INTRODUCTION

X-rays were accidentally discovered by the German physicist Wilhelm Conrad Röntgen[?] in 1895, while experimenting with accelerated electrons. He discovered a form of radiation that was able to penetrate optically opaque objects. This discovery formed the basis of medical imaging. Soon after, the first imaging devices were designed to acquire knowledge of the inside of the human body.

Quickly after, physicist and doctors realized the difficulty of reading projection images. Due to the overlap of anatomy and sometimes medical devices on the X-ray images, subtle features such as lung nodules or tiny fractures could be missed easily by the radiologist.

This problem of overlap can be solved by three dimensional imaging, which allows for the *slice-by-slice* visualization of a patient, using consecutive sectional images. Nowadays, the most popular modality for three dimensional X-ray imaging is Computed Tomography (CT), which was invented in the late 1970's. However, other techniques existed before such as (classical) tomography, which has been abandoned completely until recent advances in digital imaging have lead to its successor: tomosynthesis. Fig. 1.1 shows images of a chest phantom, obtained with these 4 mentioned techniques.

In this chapter, an introduction is given on X-ray imaging, classical tomography and digital tomosynthesis. A thorough overview on Computed Tomography can be found in the book of Buzug [?].

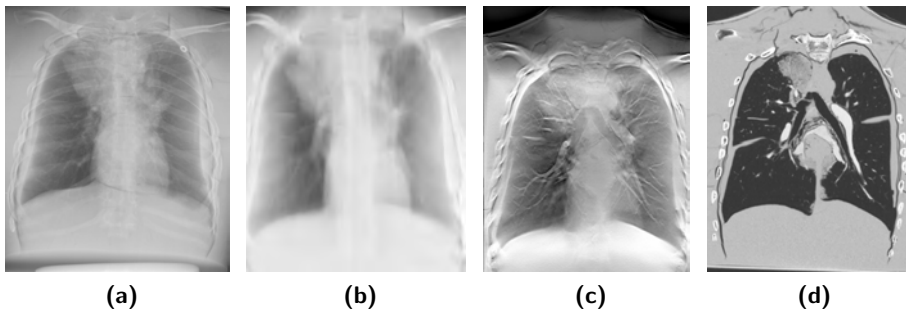


Figure 1.1: Examples of X-ray based imaging of a chest phantom (a) posterior-anterior (PA) X-ray image (b) classical tomography, with fulcrum plane in the lungs (c) tomosynthesis image, at the same depth position in the lungs (d) coronal reformat of a Computed Tomography (CT) exam, also at the same depth position.

1.1 X-ray imaging

1.1.1 X-ray generation

Vacuum tube

In medical imaging, X-rays are often produced with a vacuum tube. A typical X-ray tube is illustrated in Fig. 1.2. A cathode filament is heated to approximately 2400K, which causes electrons to escape due to thermal emission. Subsequently, these electrons are accelerated in the electric field between cathode and anode, which is created by a high voltage generator. The electrons hit the metal anode at a high speed, which is dependent on the applied voltage. For tomosynthesis imaging, which is the main topic of this work, this voltage ranges between 90kV and 120kV. The X-ray tube is made vacuum, allowing electrons to move freely towards the anode without interaction with air along their way.

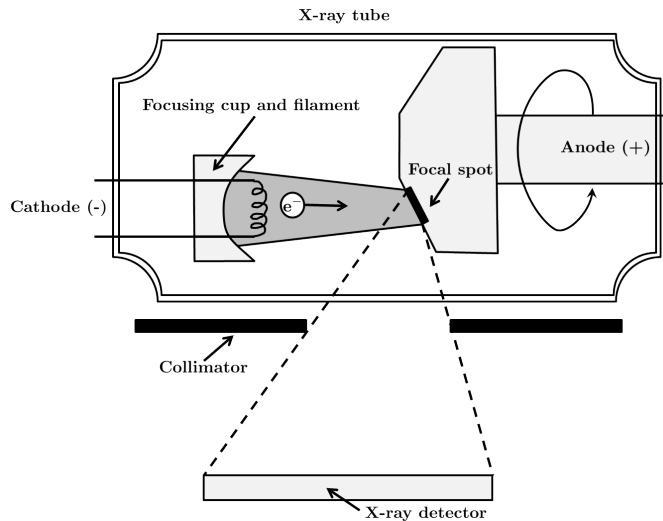


Figure 1.2: A typical X-ray tube. A heated cathode filament emits thermal electrons, which are accelerated by a high voltage electric field and subsequently hit the anode at high speed at the focal spot. X-rays emerge from the deceleration of the fast electrons upon entering the anode material. The anode is rotated, to avoid local overheating where the electrons hit the metal.

The area where the accelerated electrons hit the anode is called the *focal spot*. Upon hitting the focal spot, the kinetic energy of the electrons is converted into heat and X-ray radiation. The spectrum of this X-ray radiation has a specific

CHAPTER 1. INTRODUCTION

form, of which a conceptual example is shown in Fig. 1.3.

The continuous part of the spectrum corresponds to the *brehmsstrahlung* or *braking radiation*: the electrons entering the anode surface are decelerated by the Coulomb fields of the atoms in the anode material. This deceleration creates an electric dipole and electromagnetic waves are irradiated. Usually, several photons are emitted throughout the complete path of the incoming electron interacting with the anode atoms. If the incoming electron loses its complete kinetic energy in a single collision, a photon is emitted with a maximum energy E_{\max} (and thus minimal wavelength λ_{\min}) which is related to the applied voltage U :

$$\lambda_{\min} = \frac{1.24\text{nm}}{U}$$

with U expressed in kiloVolts (kV).

The peaks in the spectrum are caused by the *characteristic radiation*. If the bombarding electrons have sufficient energy, an electron in an inner K shell of the target metal atoms is freed. An electron from a higher (L or M) shell states drops down to fill the vacancy, emitting x-ray photons with precise energies determined by the electron energy levels. In Fig. 1.3, these peaks are labeled as K_{α} and K_{β} . Although the probability of characteristic radiation is quite high around these wavelengths, characteristic radiation contributes far less to the total X-ray radiation than brehmsstrahlung. In clinical practice, X-ray filters are used to block the low energy photons. Low energy photons are easily absorbed by soft tissue and hence do not contribute to the final image. Moreover, filtering out unnecessary radiation decreases the total radiation exposure.

Most of the kinetic energy of the electrons striking the focal spot is converted into heat (99%). To avoid overheating of the focal spot, the anode is typically designed as a rotating component. The heating of the focal spot is directly related to the amount of incoming electrons. Therefore, a larger focal spot allows for a higher amount of photons to be generated. However, with an increased focal spot, X-rays are generated from a larger area, which causes the X-rays passing through the edges of an object to hit the detector in a so called *penumbra* as illustrated in Fig. 1.4. The object edge will therefore appear blurred in the projection image. The sharpness of the projection image is thus inversely related to the focal spot size and in practice an X-ray tube is designed to have a minimal focal spot size, which still allows for sufficient generation of photons for the intended application without overheating the anode. Typical focal spot sizes for X-ray tubes used in medical devices are 0.6 – 2.0mm. Note that for a large detector, the amount of blurring due to the focal spot size varies locally on the detector. For imaging systems with large detectors such as tomosynthesis, a locally varying focal spot size should therefore be taken into account to improve image quality [? ?].

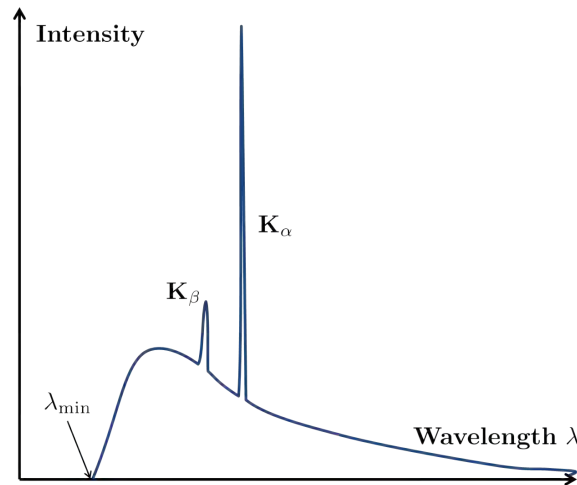


Figure 1.3: Conceptual example of an X-ray spectrum, generated by an X-ray tube. The continuous spectrum represents the different energy levels of the photons in the *Bremsstrahlung*, whereas the peaks around K_α and K_β represent the *characteristic radiation*.

The orientation of the anode surface has another effect on the produced X-ray beam. X-ray beams that leave the anode at a very sharp angle with the anode surface are more likely to be absorbed again by the anode material than beams leaving at larger angles with the surface. This effect is known as the *Heel effect* and causes the X-ray beam to be less intense on the anode side and more intense on the cathode side. The intensity inhomogeneities induced by the heel effect in digital radiographs can be corrected retrospectively [?].

Other methods for X-ray generation

A recent method to reduce anode heating is based on *liquid metals*. In these X-ray devices, the anode material is replaced by a liquid which has much better heat dissipation properties [?]. High-brilliance micro-focus sources based on liquid metal anodes allow imaging with a very high resolution, and are currently being investigated in various X-ray imaging applications [? ?].

Electron beam tomography (EBCT) is a form of computed tomography (CT), in which X-rays are generated from different angles around the patient. However, contrary to CT, in EBCT these X-rays are not generated by a moving X-ray tube. Instead, a beam of electrons, generated from a stationary source, is swept at high speed along a tungsten arc of 210° around the patient, who is lying on a radiologic cradle. The impact of the electron beam against the tungsten ring causes the

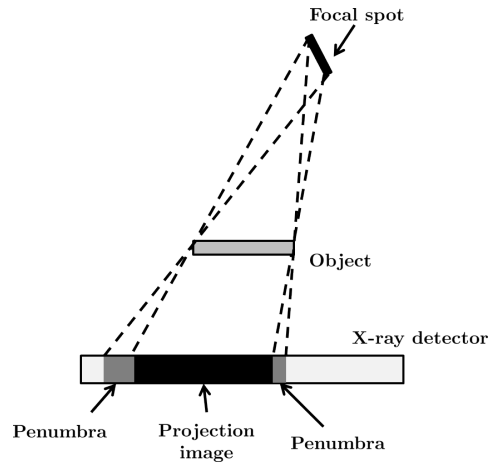


Figure 1.4: Illustration of the effect of the focal spot size. Due to the non-zero size of the focal spot, the X-rays passing through the object boundaries hit the X-ray detector in a zone called *penumbra*, which leads to a blurred edge in the projection image. The size of this penumbra and thus the amount of blurring is related to the size of the focal spot and the location on the detector.

emission of a fan of X-rays. The circular sweeping of the x-ray fan reproduces the function of a mechanical CT that uses moving parts revolving around the human body. Images are obtained with a 50 to 100msec scan time [?]. However, the very high cost and relatively poor flexibility of EBCT scanners (EBCT scanners are essentially single purpose cardiac scanners) has led to poor uptake. Nowadays, modern multislice CT scanners have become the standard for cardiac imaging.

In a *carbon nanotube (CNT) X-ray source*, the classical thermionic cathode is replaced by an array of CNT based electron field emission cathodes. These new X-ray sources require no heating of the cathode which allows for instantaneous turning on and off of the X-ray beam. This allows for fast image acquisition and physiological gating for medical applications. The CNT X-ray sources are also compact in design and can therefore be placed very close together which allows for creation of X-ray source arrays with unique geometries. [? ? ? ? ?].

1.1.2 X-ray interaction with matter

When a photon encounters matter on its path, several interactions can occur which form the underlying principle of X-ray imaging. In general, a mono-energetic beam

of photons is exponentially *attenuated* when passing through matter:

$$I(s) = I_0^- \int_0^s \mu(\eta) d\eta \quad (1.1)$$

with I_0 the intensity emitted by the X-ray source and $I(s)$ the intensity after attenuation by the object along a ray of length s . The material dependent attenuation of the object is represented by $\mu(\eta)$. Most algorithms discussed in this work are based on Eq. 1.1, which is known as the law of *Beer-Lambert*. Often Eq. 1.1 is transformed into a linear sum of attenuations before further processing is applied:

$$-\ln \left(\frac{I(s)}{I_0} \right) = \int_0^s \mu(\eta) d\eta \quad (1.2)$$

Note that in many clinical systems a mono-energetic X-ray beam is hard to generate, and typically the beam consists of photons with multiple energies. The attenuation coefficient of a certain object is also depending on the energy of the photon, and hence X-ray attenuation can be written as

$$I(s) = \int_0^{E_{\max}} I_0(E)^- \int_0^s \mu(E, \eta) d\eta dE \quad (1.3)$$

with μ also depending on the delivered energy E .

X-rays are harmful to the human body. Therefore, radiation dose must be kept as low as reasonably achievable, also called the 'ALARA' principle [? ?]. The effective dose of a postero-anterior (PA) chest X-ray of an average adult male is estimated to be 0.02mSv, and for a lateral view 0.04mSv. The effective dose of a chest tomosynthesis exam is 0.12mSv, which is about twice the dose of a two-view chest exam [? ? ? ? ? ?]. The average effective dose of a chest tomosynthesis exam is about 12% that of a chest CT exam. Also, patient body size has been shown to have a much greater impact on radiation dose of chest CT examinations than chest radiography and tomosynthesis [?].

1.1.3 X-ray detection

The X-ray detector is a key component of (chest) radiography. In the past few decades, changes in detector technology have ultimately led to new image acquisition techniques, including tomosynthesis.

Scintillators

The original means to visualize X-rays, which also led to their discovery by Röntgen, was a barium plate which turned the incoming photons to visible light by excitation of the barium atoms. Devices were soon after designed with a photo luminescent

CHAPTER 1. INTRODUCTION

plate, which lightened up at the arrival of incoming photons. An example of such a device with a fluoroscopic screen is shown in Fig. 1.5. For a more in depth description of the first X-ray devices and modalities, refer to the work of Webb[?].



Figure 1.5: Photo of experimenters taking an X-ray with an early Crookes tube apparatus, from the late 1800s. The upper man is examining the bones of his hand with a fluoroscope screen, while the lower man is taking a radiograph of his hand with a photographic plate. No precautions against radiation exposure are taken; its hazards were not known at the time. Image taken from “The X-ray, Photography of the invisible and its value in surgery” [?]

Film based systems

The first method to store the generated X-ray image more permanently was using photographic film, which was sandwiched between two layers of phosphor screens. The screens served as the primary medium to convert x-ray photons to light photons, which were then captured by the film. Subsequently, the film was developed in dedicated machines using photochemical substances (Fig. 1.6a). The dominant producers of photographic film at the time naturally extended their portfolio to also produce film suitable for X-ray imaging. Fuji, Kodak, and the Belgium based Gevaert company all produced film and the according equipment to generate X-ray images for decades.

X-ray imaging with film imposed some limitations on the practice of chest radiography, due to their limited light range sensitivity. The right X-ray tube current, voltage and exposure time and according film sensitivity depended on patient size and positioning, and required profound experience of the X-ray technician in



Figure 1.6: Examples of Agfa equipment for (a) film based X-ray imaging, (b) computed radiography (CR) and (c) direct radiography (DR).

order not to over or underexpose the film.

Computed radiography

The next technological breakthrough was Computed Radiography (CR), in which the photographic film was replaced by a phosphorescent plate that could be read out by a digitizer to produce a digital image (see Fig. 1.6b). CR emerged in the early 80's and would become the dominant imaging technology in radiology for decades, gradually replacing all analog (film based) X-ray imaging machines [? ? ?]. The advent of digital imaging opened up an entire research domain on image processing. After the X-ray image was read out by the digitizer, a whole new image processing chain was set in place to improve the detected image. In a first step, the detected raw image is cleaned of any artifacts that were caused by the digitizer equipment itself. Subsequently, if an anti-scatter grid has been used, the footprint of this grid is removed by grid removal software [? ? ?]. This removal is necessary, because the grid shadow causes Moirée effects on monitors with a lower display resolution when unremoved (see Fig. 1.7). Finally, image contrast improvement software is applied to improve the contrast of the raw image[? ? ?] (Fig. 1.8).

The high dynamic range of the CR detector system allowed for a wider range of incoming photon counts and thus less sensitivity to the X-ray generator settings. Moreover, due the inherent digital nature of CR, the images naturally fit into the electronic Picture Archive and Communications System (PACS) of the hospital, which provides digital archiving and viewing.

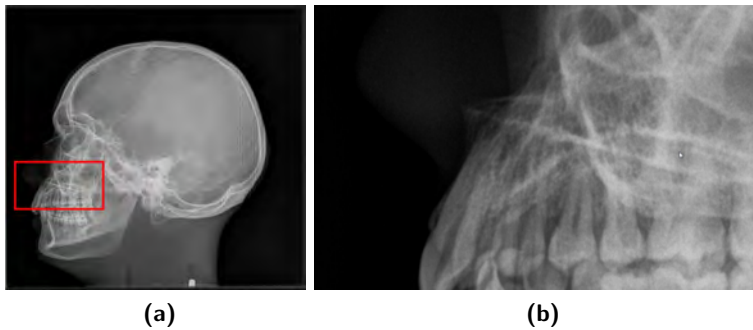


Figure 1.7: (a) shows the Moire effect: vertical stripes appear on a low resolution monitor due to the high frequent grid footprint which is present in the image (b) the zoomed region shows the high frequent grid footprint

Direct radiography

The cassette based workflow in CR demanded that each single X-ray image had to be digitized by a dedicated machine before the next image could be taken. Despite the transition from analog to digital imaging in CR, this workflow did not allow for tomosynthesis imaging in which a sequence of multiple images from different angles needed to be acquired in a short time.

Direct Radiography (DR) was a necessary technological breakthrough for tomosynthesis imaging. Similar to CR, the DR flat panel detector (Fig. 1.6c) contains a phosphor plate which converts the X-rays into visible light. However, the conversion to a digital image now occurs in the detector itself, by the means of CCD or CMOS based cameras that detect the light directly from the phosphor layer. DR based detectors can image multiple frames per second, which allows to acquire an entire tomosynthesis sequence in several seconds without manual cassette handling between exposures by a radiographer. The rise of tomosynthesis techniques in clinical practice is closely coupled to the availability of DR detectors.

1.2 From planigraphy to digital tomosynthesis

The invention of X-ray imaging was quickly accepted as a major discovery in medicine. It enabled physicians to learn about the inside of the human body without actually opening it in surgery. However, images generated with an X-ray modality were and still are often difficult to interpret due to the overlap of anatomy.

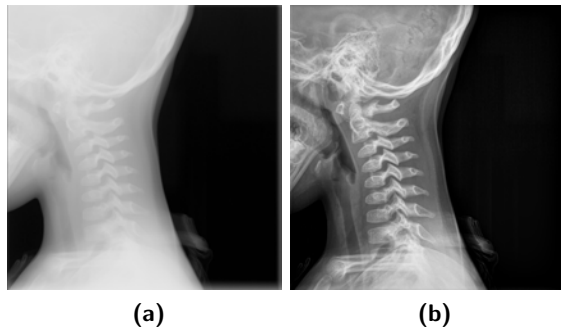


Figure 1.8: (a) a raw image, read out from a DR detector, before contrast improvement (b) the same image, after processing with the Musica3 algorithm.

This section provides an introduction on planigraphy and digital tomosynthesis. Both are techniques to produce sectional images of a patient, which reduces the visual overlap of anatomy. Whereas the former was invented in the 1930s and was clinically used until the 1980s, the latter only emerged in the last decade due to technological advances in detector technology and computing power. The section is concluded with a summary on the clinical applications of chest tomosynthesis.

1.2.1 Planigraphy

The first apparatus for section imaging was developed by Ziedses des Plantes [?] in 1931. During his night shift as an assistant doctor in a psychiatric hospital, des Plantes was faced with the decease of a patient due to a brain tumor that was not detected on a routine X-ray image of the skull. He realized that the brain tumor would have been detected if only a sectional plane of the skull was visualized, comparable to a slice under a microscope. Having an additional background as electrotechnical engineer, an idea he had several years earlier on a device for planigraphic imaging came to his mind again. He designed a *planigraphy* device consisting of a moving X-ray source and a film holder, moving in the opposite direction. Due to the relative motion of source and X-ray detector, an image was obtained of the patient's head which was sharp around the rotation center (the fulcrum), whereas anatomy above and below this fulcrum plane was smeared out over the X-ray film.

The principle of planigraphy is illustrated in Fig. 1.9. Only the objects in the focal plane are imaged sharply, whereas objects in planes above and below this focal plane are smeared out in the projected image due to the relative motion of

CHAPTER 1. INTRODUCTION

X-ray source and film during the acquisition. Example planigraphy (or classical tomography) images of a chest phantom are displayed in Fig. 1.10.

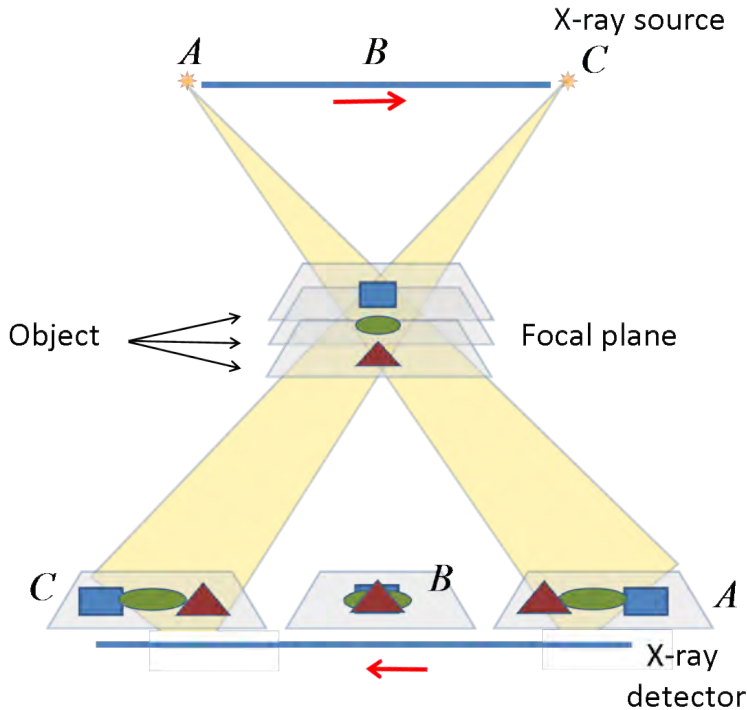


Figure 1.9: Principle of planigraphy. During the acquisition of an image, the X-ray source moves from A to C , while the X-ray detector moves in opposite directions underneath the object. In the resulting image, only a single focal plane in the object (containing the green circle) is projected onto a fixed position, while structures above and beyond the focal plane are smeared out in the projection image.

Similar ideas were formulated even earlier by Bocage [?], Portes and Chaussé, but were never put in practice. Vallebona also described a device in which a rotating patient was imaged with a still X-ray source and detector. A more elaborate history on the early days of tomography is presented by Webb [?].

The technique of planigraphy, later known as *tomography*, was commonly used in clinical practice between 1950 and 1980, for various diagnostic tasks such as the localization of kidney stones and brain tumor imaging [?]. Examples of such systems are displayed in Fig. 1.11, which were also capable of non-linear motion to improve the blurring of out-of-plane structures. From 1970 onwards,

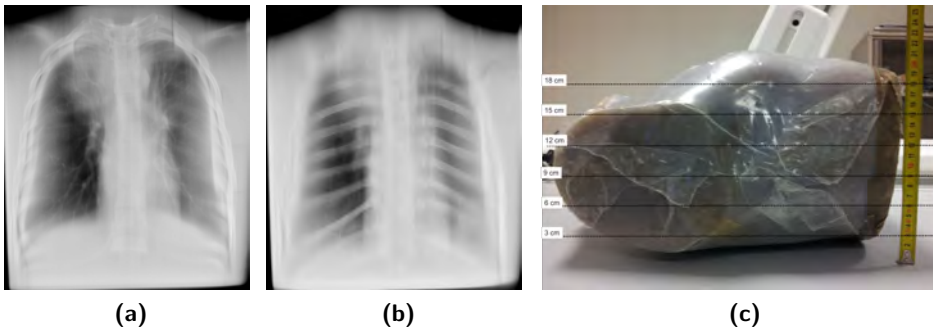


Figure 1.10: Planigraphic images of a chest phantom, acquired at a depth of (a) 12cm and (b) 3cm. Note the vertical blurring of structures outside the focal plane. (c) shows a picture of the chest phantom, with an indication of the depths relative to the detector.

planigraphy (also called classical tomography) became gradually replaced by computed tomography.

1.2.2 Tomosynthesis

The technique of planigraphy as designed by des Plantes had two obvious drawbacks. First, to image a different focal plane a new planigraphic image had to be acquired, which resulted in high X-ray exposure doses for the patient. Second, although anatomy that was located above and below the focal plane was smeared out in the planigraph, it still was overlaying the image. Completely suppressing out-of-plane details was not possible, despite the design of more complex motion paths to optimize the smearing out of structures not in focus [?].

To overcome the first drawback concerning the multitude of planigraphs that had to be acquired for each single focal plane, des Plantes already described a technique in his doctoral thesis [?] in 1934. If separate radiographs were acquired from each projection angle, the original tomography could be imitated by summing (overlying) these radiographs. By properly shifting the images before summation, planigraphs at specific focal planes could be *synthesized* using the same stack of radiographs. An illustration of this *shift-and-add technique* is presented in Fig. 1.12. Depending on the amount of shift, one specific plane in the object will be in focus while the other planes will be blurred. This principle was described further in detail by Garrison [? ?] and embodied the first implementation of *tomosynthesis*. The shifted summation of the projection images can also be seen as *unfiltered backprojection*.

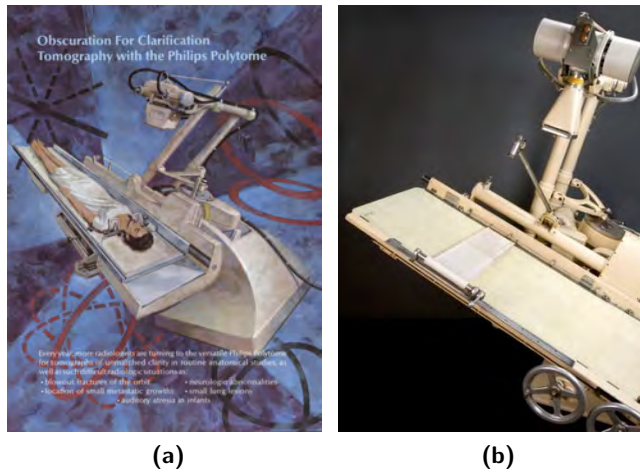


Figure 1.11: (a) The Philips polytome (1952), capable of linear, circular and spiral relative movement of X-ray source and film holder. (b) Massiot device, also designed for planigraphy.

Alternative source/detector setups for tomosynthesis

Besides the setup with a moving X-ray source and a flat panel detector as described above, alternative setups exist for tomosynthesis that were developed recently. *Stationary* tomosynthesis is realized with a fixed source and detector, thus eliminating the mechanical motion of the tube or detector. The classical X-ray tube is replaced by an array of carbon nanotube sources, which can be triggered individually by electronics at high speed [?]. Initial clinical experiments show that with a suitable flat panel detector that provides a high enough scanning rate, the total acquisition time for a stationary tomosynthesis exam could be reduced to 1/3d of a conventional tomosynthesis exam, which reduces the effects of patient motion during the scan [?]. Moreover, the CNT technology allows for gated exposures, in which the X-ray pulses could be synchronized with a breathing monitor for patients unable to hold their breath.

In a *scanning-beam digital x-ray (SBDX)* system, a large-area x-ray target is scanned with electron beams, and X-rays are emitted from an array of source positions aligned with collimators and directed at the small area digital detector array in a so-called *inverse geometry* [?]. Designed originally for cardiac imaging, the SBDX setup was recently adapted for chest imaging. SBDX offers several advantages. The scanning source obviates the need for mechanical motion, allowing acquisition of tomosynthesis data sets at speeds limited only by the detector

1.2. FROM PLANIGRAPHY TO DIGITAL TOMOSYNTHESIS

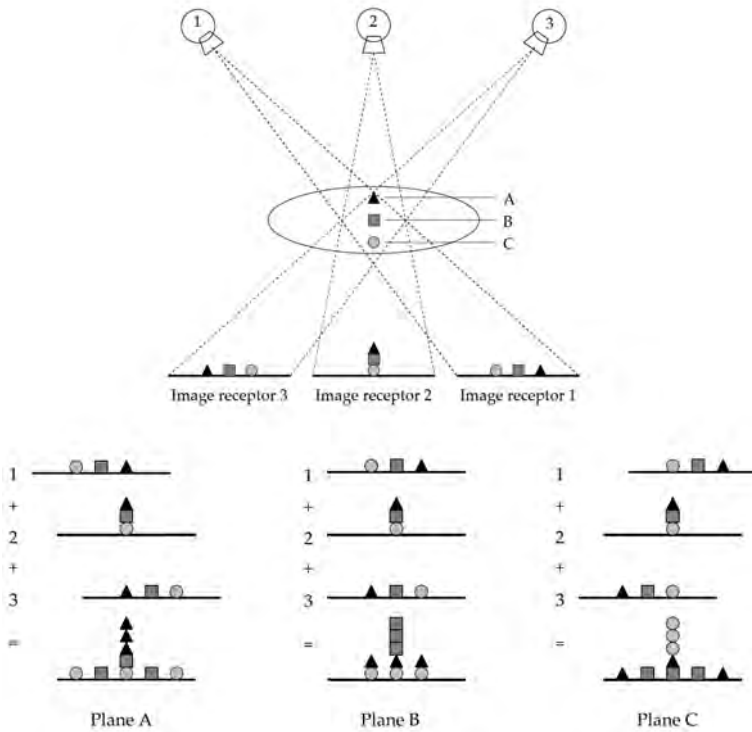


Figure 1.12: Illustration of the shift-and-add technique. Image taken from [?]. By shifting the acquired projection images relative to each other before summation, objects from different planes in the patient will be in focus while objects in other planes will be smeared out.

1.3. TOMOSYNTHESIS RECONSTRUCTION

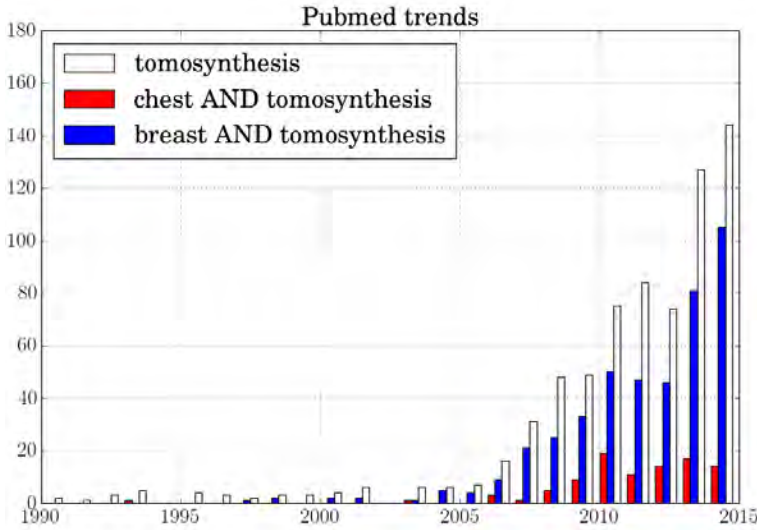


Figure 1.13: Pubmed trends for tomosynthesis

pression of blurred out-of-plane image information. These initial approaches were all variants of deblurring algorithms, that were designed to remove the blur in the computed tomographic images as a post processing step. A thorough review of the early methods for tomosynthesis reconstruction can be found in Dobbins [?].

The first deblurring algorithm from Edholm [?] was a method to subtract a blurred transparent negative photographic copy from the original image, which was basically an analog implementation of a high pass filter. This approach was later also applied to digital tomosynthesis with high pass filtering [?] and band pass filters [?].

Ruttiman [?] proposed a novel concept to use planes adjacent to the plane of interest in a spatial iterative deconvolution. He subtracted a set of properly blurred adjacent planes from the plane of interest to remove the blur, caused by features in out-of-focus planes. A similar approach of *selective plane removal* was mentioned by Roy [?], in which distortions from closely adjacent planes were eliminated with the use of a blurring function. In another technique, adjacent planes were reprojected onto a target plane after initial reconstruction to estimate their contribution to the blurring in that target plane [?].

In matrix inversion tomosynthesis (MITS) [?], linear systems theory is used, along with a priori knowledge of the imaging geometry, to deterministically dis-

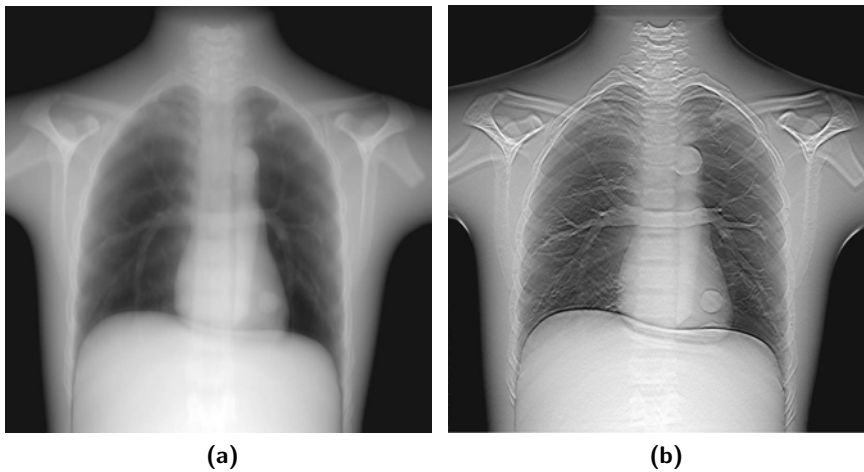


Figure 1.14: (a) Unfiltered backprojection plane of an anthropomorphic chest phantom. Note the excessive tomographic blur. 21 images were acquired over an angle of 7° . (b) The same plane, after deblurring with matrix inversion tomosynthesis (MITS). Both images taken from Godfrey et al[?].

tinguish between true structure and overlying tomographic blur in a set of conventional tomosynthesis planes. Fig. 1.14 compares an unfiltered backprojection image with a plane reconstructed with MITS. The essence of the MITS algorithm is an attempt to distinguish between in-plane detail and residual tomographic blur in a conventional backprojection tomosynthesis dataset. Knowledge of the imaging geometry is combined with linear systems theory to generate a set of coupled linear equations that describe how objects located in distant planes within the reconstruction set are blurred onto each local plane of interest. Deblurring is then performed in the frequency domain, by multiplying the spectra of each conventional tomosynthesis plane by the inverse of the deterministic blur matrix for each frequency.

Recently, Wu [?] analyzed the impulse responses of common tomosynthesis systems on a plane-to-plane basis and proposed a fast and accurate convolution-based blur-and-add (BAA) model to simulate the backprojected images.

A *wavelet* based approach for removing blurred out-of-plane structures [?] turned out to be effective for a specific class of objects, namely these presenting features of high contrast and high frequency such as high-speed rotational angiography. Finally, three dimensional anisotropic diffusion filtering [?] can also be applied to filter out unwanted blurring.

1.3. TOMOSYNTHESIS RECONSTRUCTION

In some methods for tomosynthesis, the backprojection itself is modified to only backproject the smallest or largest value for a particular voxel. In these nonlinear *extreme-value-reconstruction* methods [? ? ? ?], it was required that the plane of interest contained the most extreme value and at least one relatively unobstructed view of the voxel in question was available. For clinical tasks where the object of interest was high contrast compared to its surroundings, such as with angiography, these extreme-value reconstructions proved effective.

A *voting strategy* was applied, which rejects the projections that include too high values, for the reconstruction of artifacts caused by a needle in breast tomosynthesis [?]. In an empirical adaptive weighting scheme, backprojection blur is reduced in musculoskeletal tomosynthesis [?].

1.3.2 Analytical reconstruction algorithms

A different class of methods for tomosynthesis is based on the Fourier slice theorem, which expresses the relationship between a projection image and the Fourier transform of the object. In a simple two step approach, the projection data are first filtered and subsequently backprojected. This leads to the *Filtered Backprojection* (FBP) algorithm, which is intensively used in computed tomography (CT) [?].

In tomosynthesis however, projections are only acquired over a limited angle, which leaves entire regions of the object's frequency space unsampled. The direct inversion of the sampled Fourier space therefore becomes more problematic. In 1980, Edholm and colleagues described *ectomography*, in which inverse filters were chosen to create a constant sampling density within the sampled region of the 3D frequency domain of the object, as well as the 2D frequency domain of the reconstructed planes [? ? ?]. Other filtered backprojection approaches have led to the selection of slightly different filters [? ? ? ?].

1.3.3 Iterative reconstruction techniques

In *iterative* reconstruction algorithms, the slices at different depths are iteratively updated until a certain stopping criteria is met. In general, iterative reconstruction algorithms offer increased flexibility compared to their analytical counterparts, as prior knowledge about the imaged object can be added to the reconstruction algorithm through the means of a regularization term. Moreover, the physics of the acquisition can be modeled in the projection model of the reconstruction such as finite focal spot size, source motion, detector characteristics etc. For a full overview on the different physical effects and their effect on the reconstruction, refer to Nuyts et al [?].

In iterative reconstruction techniques, two main classes of algorithms can be

distinguished: *algebraic reconstruction* (used in this work) and *statistical reconstruction*.

1.3.4 Challenges in chest tomosynthesis reconstruction

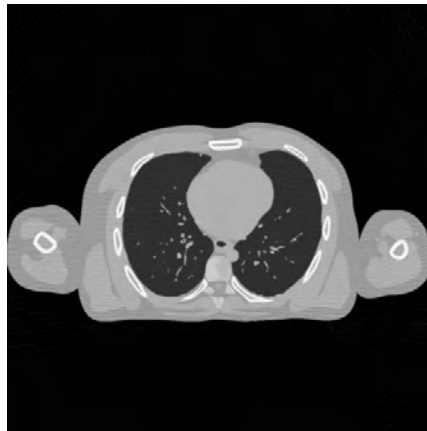
Compared to a classical computed tomography (CT) reconstruction (Fig. 1.15), tomosynthesis poses some additional challenges towards reconstruction algorithms:

- *Limited angle acquisitions*: the X-ray source moves over only a limited acquisition angle relative to the patient. As a consequence, the frequency space of the object is not sampled entirely and a 'missing wedge' appears in the frequency domain of the image. This leads to reconstruction artifacts, as illustrated in Fig. 1.16a. In general, the limited angle causes a loss of depth resolution in tomosynthesis. Some setups provide a dual view, to partially overcome angular undersampling [?].
- *Truncation*: the chest of the patient is larger than the detector. Moreover, the detector either remains stationary or moves only in a single plane, which causes different parts of the anatomy to be imaged in the acquired images depending on the positions of source and detector. Generally, this leads to truncation artifacts (Fig. 1.16b) although recent advances in reconstruction theory have made possible to exactly reconstruct parts of the image under certain conditions [?].
- *Limited view*: Unlike CT, in tomosynthesis the projection density is too low to allow for exact reconstruction even if projections would have been acquired over a full rotation around the patient. The coarse angular sampling causes ringing and streak artifacts (Fig. 1.16c), which are a known drawback of tomosynthesis. In practice, acquisition protocols are tuned to reduce the effect of the ringing to an extent that it does not hinder clinical evaluation of the reconstructions [? ? ?]. If available, a prior CT scan could also be used to overcome these ringing artifacts [?].
- *Geometric instability* Unlike a CT scanner, a tomosynthesis system is more prone to mechanical instability. Errors in the assumed geometry also cause artifacts in the reconstruction (Fig. 1.16d), and therefore TS systems need to be calibrated carefully. This problem becomes worse if no mechanical coupling exists between source and detector, which is the case in mobile tomosynthesis imaging. A method to derive the exact geometry on the fly is presented in Chapter 5.
- *Patient motion*: Patient motion during the acquisition of the images causes inconsistencies and results in motion artifacts in the reconstruction. A thor-

1.3. TOMOSYNTHESIS RECONSTRUCTION

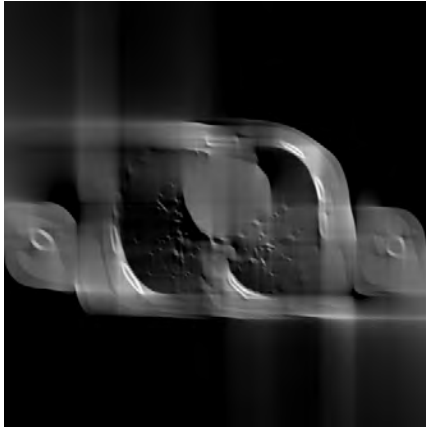
ough review on motion artifact correction for CT imaging can be found in the work of Van Eyndhoven [?]. However, tomosynthesis imaging remains sensitive to patient motion and acquisitions are performed with a breath-hold protocol to prevent patient motion.

- *System motion*: Besides the patient, the X-ray source and/or detector are also in motion during the acquisition of the image series for tomosynthesis. Chapter 3 describes a reconstruction technique for imaging an object or patient with a moving X-ray source, that continuously emits X-ray radiation during a continuous motion. The technique is applied to CT imaging as well as tomosynthesis reconstructions.

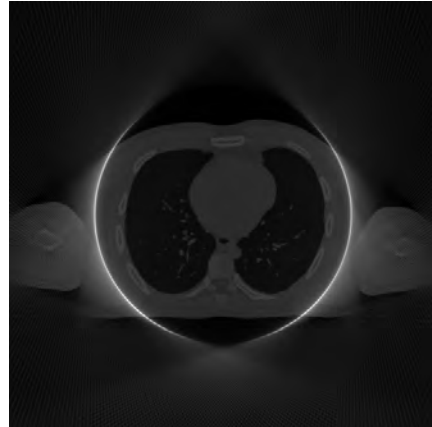


(a)

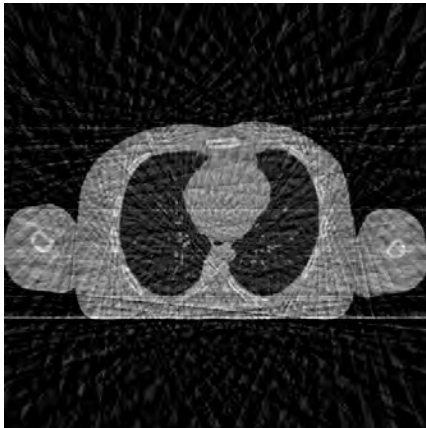
Figure 1.15: FBP reconstruction of a single slice of the XCAT phantom, using $n = 180$ projections with angular coverage of π .



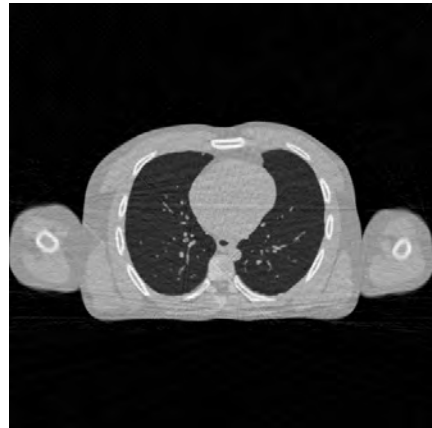
(a) limited angle



(b) truncation



(c) limited view



(d) geometric inaccuracy

Figure 1.16: Examples of FBP reconstructions from sinograms with challenges. (a) limited angle of $\pi/2$ (b) truncated projections (c) limited view ($n = 30$) (d) $n = 180$, angle= π , angle errors randomly distributed between $[-0.5^\circ \dots 0.5^\circ]$.

2

Limited view reconstruction

Contents

2.1	Introduction	24
2.2	Total Variation Regularization	26
2.3	Experiment	27
2.4	Conclusion	28
	References	31

2.1 Introduction

In a typical chest tomosynthesis exam, 53 low dose Tomosynthesis X-Rays (TSXRs) are acquired over an angle of 35° , which corresponds to an angular density of $52/35 \approx 1.5$. However, for a mobile tomosynthesis device, a reduction of the number of TSXRs (also called views) would be preferred (Fig. 2.1), as the exam will often be performed outside the radiology department in environments with less radiation protection. Also, a reduction of the number of views could simplify the mechanical and electronical design of the mobile modality and reduce the total acquisition time.

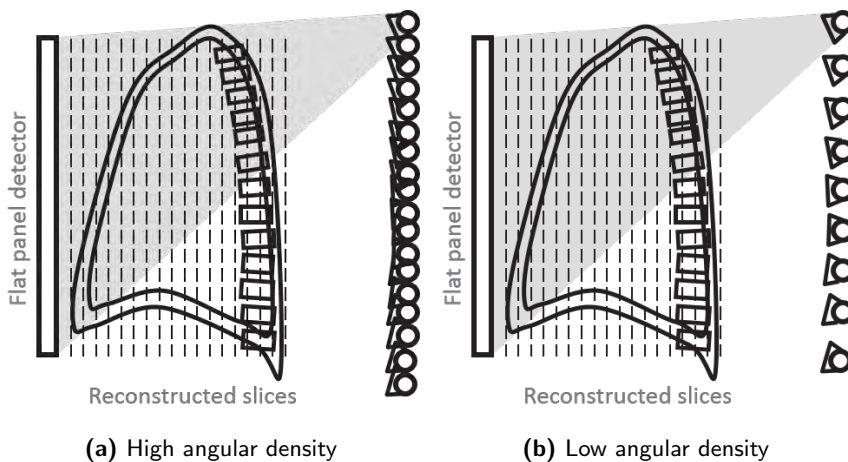


Figure 2.1: In chest tomosynthesis, several low dose postero-anterior tomosynthesis X-ray images (TSXRs) are acquired with a wall mounted flat panel. (a) Scheme for regular tomosynthesis (b) scheme with reduced angular density

The reduction of the number of views or projection images is known as the *limited views* problem in CT reconstruction and is the cause of streak and ringing artifacts. This is illustrated in Fig. 2.2. A Shepp-Logan phantom (Fig. 2.2a) was reconstructed using 80 parallel beam projections over an angle of 40° . The resulting reconstructed image (Fig. 2.2b) shows geometric distortions, due to the limited angle of only 40° .

The reconstruction of the same phantom with only 10 views over the same angle of 40° is shown in Fig. 2.2c. The image now clearly shows streak artifacts, on top of the geometric distortion. The ringing artifacts can also be seen in Fourier space in Fig. 2.3. Whereas the FFT of the reconstruction using 80 projections

(Fig. 2.3a) only shows a missing wedge in the Fourier space due to the limited angle of only 40° of the acquisitions, the FFT of the reconstruction using only 10 projections (Fig. 2.3b) also shows that the information inside the non-missed wedge is insufficiently sampled.

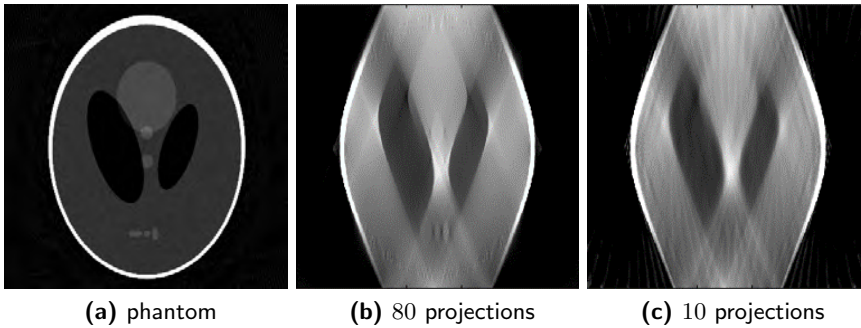


Figure 2.2: (a) Shepp-Logan phantom (b) reconstruction using 80 projections over 40° (c) reconstruction using 10 projections over 40° , showing streak artifacts.

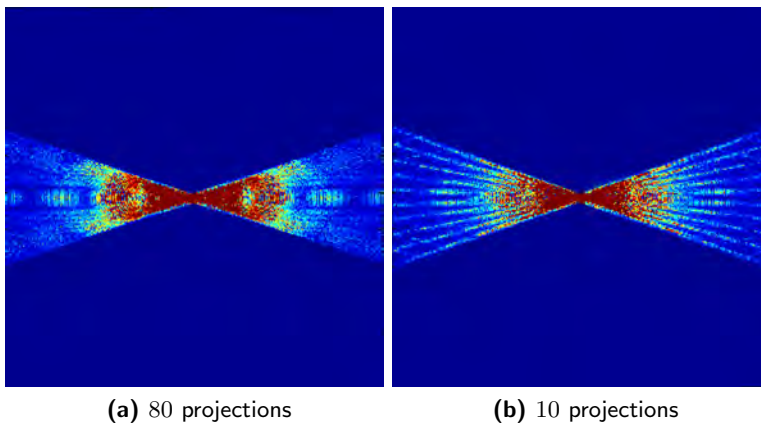


Figure 2.3: FFT of the reconstructed Shepp-Logan phantom using (a) 80 projections (b) 10 projections

The effect of reducing the angular density in chest tomosynthesis is illustrated on an antropomorphic phantom in Fig. 2.7. A reduction from 53 to 11 views results in ringing artifacts, which are presented as shadows of sharp edges (in this case

CHAPTER 2. LIMITED VIEW RECONSTRUCTION

the border between the rib and air) on planes above and below these structures. In a reconstruction with sufficiently high angular density, this ringing artifact has a high spatial frequency and is thus not noticed by a human observer. However, with the reduction of the angular density, the artifact becomes low frequent and can easily be noticed.

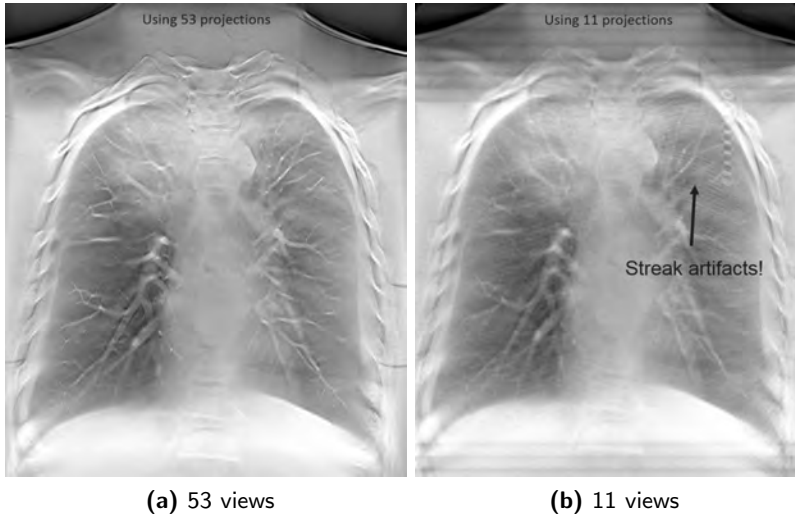


Figure 2.4: Chest tomosynthesis reconstruction of an anthropomorphic phantom using (a) 53 views and (b) only 11 views, which results in streak artifacts.

2.2 Total Variation Regularization

An often used technique to reduce ringing artifacts in CT reconstruction is to add a regularization term to the reconstruction problem, which uses prior knowledge about the object to be reconstructed. A popular form of regularization in medical imaging is the reduction or minimization of the Total Variation (TV) in the image, which is based on the prior knowledge that the density (attenuation value) of a patient only changes at the borders of organs and internal structures, and remains relatively constant within these structures. The reconstruction algorithm can thus be rewritten as

$$\arg \min_{\mathbf{x}} \|\nabla \mathbf{x}\|_{TV} \text{ subject to } \|\mathbf{A}\mathbf{x} - \mathbf{b}\| < \epsilon \quad (2.1)$$

with \mathbf{x} the reconstructed image, \mathbf{A} the system matrix which models the projection and \mathbf{b} the acquired images. The error ϵ is chosen in function of the noise \mathbf{b} . Of all possible solutions of \mathbf{x} with sufficiently low projection difference $< \epsilon$, the solution is chosen with the lowest Total Variation $\|\nabla\mathbf{x}\|_{TV}$.

One of the first concrete implementations to add the Total Variation penalty into a reconstruction algorithm was proposed by Sidky[?] in 2006. His Adaptive Steepest Descent - Projection Onto Convex Sets (ASD-POCS) algorithm is based on the Simultaneous Iterative Reconstruction Technique (SIRT). A block of N_{data} SIRT iterations are followed by a block of N_{grad} weighted TV reduction steps, to force a lower TV of the solution of the reconstruction algorithm. This procedure is repeated N times. As the updates of the SIRT iterations become smaller, the weight for the TV steps also decreases to guarantee convergence of the method (for a more detailed description of ASD-POCS refer to [?]).

```

x = 0;
while  $n < N$  do
  do  $N_{\text{data}}$  SIRT iterations;
  apply positivity constraint;
  do  $N_{\text{grad}}$  steepest descent iterations on TV;
end

```

Algorithm 1: The ASD-POCS algorithm pseudocode

2.3 Experiment

To study if ASD-POCS could be used to suppress the streak artifacts in tomography with a reduced number of views, simulations were performed with the XCAT [?] phantom (Fig. 2.5). First, 40 noiseless projections were simulated over an angle of 40° . A SIRT reconstruction was performed which stopped at $N = 80 \times 20$ iterations (Fig. 2.6a). Note the high frequent streak artifacts, originating from structures with high contrast. The ASD-POCS reconstruction (Fig. 2.6b) was stopped after $N = 80$ iterations, using $N_{\text{data}} = 20$ and $N_{\text{grad}} = 20$. Although the number of SIRT iterations remained equal in the ASD-POCS reconstruction, the streak artifacts were removed thanks to the Total Variation reduction steps.

Next, only 11 projections were simulated of the same XCAT phantom, over the same angle of 40° . The SIRT reconstruction now shows streak artifacts with a lower spatial frequency (Fig. 2.6c), which could not be removed as effectively with ASD-POCS (Fig. 2.6d) as in the experiment with 40 projections. To get rid of the more prominent streak artifacts that appear in reconstructions using a low angular sampling of only 11 projections over 40° , the weight of the TV regularization has to be increased much more. However, this also leads to the removal of small structures

CHAPTER 2. LIMITED VIEW RECONSTRUCTION

that are not unwanted, such as subtle lung tissue changes or small vessels, and the appearance of the so called cartooning effect which can already be seen in Fig. 2.6d.

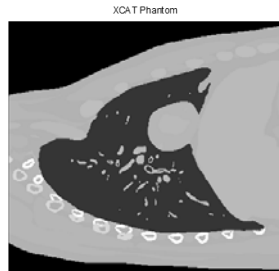


Figure 2.5: The XCAT phantom

In a second experiment, 11 projections were experimentally acquired over an angle of 40° of an antropomorphic phantom in a tomosynthesis setup. The source image distance (SID) was 120cm, and a Canon flat panel detector was used with 3408×2800 pixels of $0.125\mu\text{m}$ size. Tube was set to 1 mAs and 90 kV.

The projections were reconstructed with SIRT and ASD-POCS, respectively. The results are displayed in Fig. 2.7. The SIRT reconstruction (Fig. 2.7a) shows streak artifacts, as could be expected. In the ASD-POCS reconstruction (Fig. 2.7b), the TV descent steps reduced the noise but did not fully remove the streak artifacts. Moreover, subtle cartooning already starts to appear which indicates the weight of the TV regularization could not be increased without deteriorating overall image quality. Note also in the insets of the image how the streak artifacts have similar structure and intensity compared to the smaller lung vessels, which should not be removed by the regularization.

2.4 Conclusion

To conclude, adding TV regularization for tomosynthesis images might bring benefits for noise suppression, and the removal of subtle streak artifacts which can be seen in reconstructions with a high angular sampling. However, when the angular sampling becomes much more sparse such as in the example with only 11 projections over an angle of 40° , the streak artifacts become too strong and other methods should be used to suppress the streak artifacts. In the next Chapter, an entirely different approach is presented to reduce streak artifacts caused by angular undersampling.

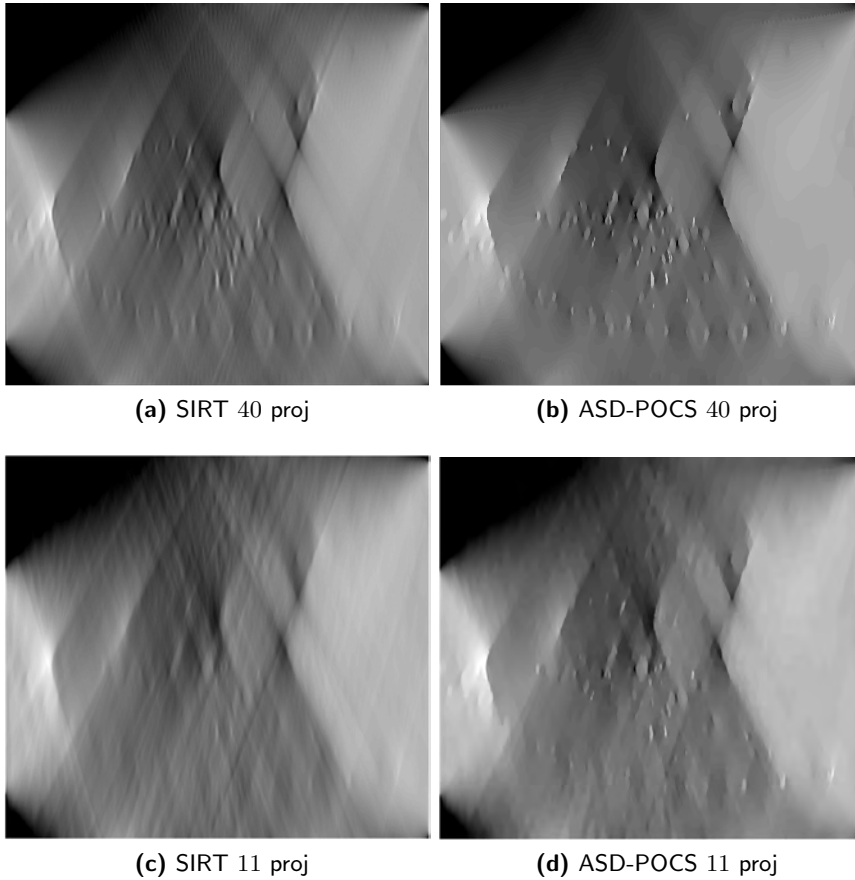


Figure 2.6: Chest tomosynthesis reconstructions of the XCAT phantom, using projections acquired over 40° . (a) SIRT, $N = 80 \times 20$, 40 projections (b) ASD-POCS, $N = 80$, $N_{\text{data}} = 20$, $N_{\text{grad}} = 20$, 40 projections. (c) SIRT, $N = 80 \times 20$, 11 projections (d) ASD-POCS, $N = 80$, $N_{\text{data}} = 20$, $N_{\text{grad}} = 20$, 11 projections.

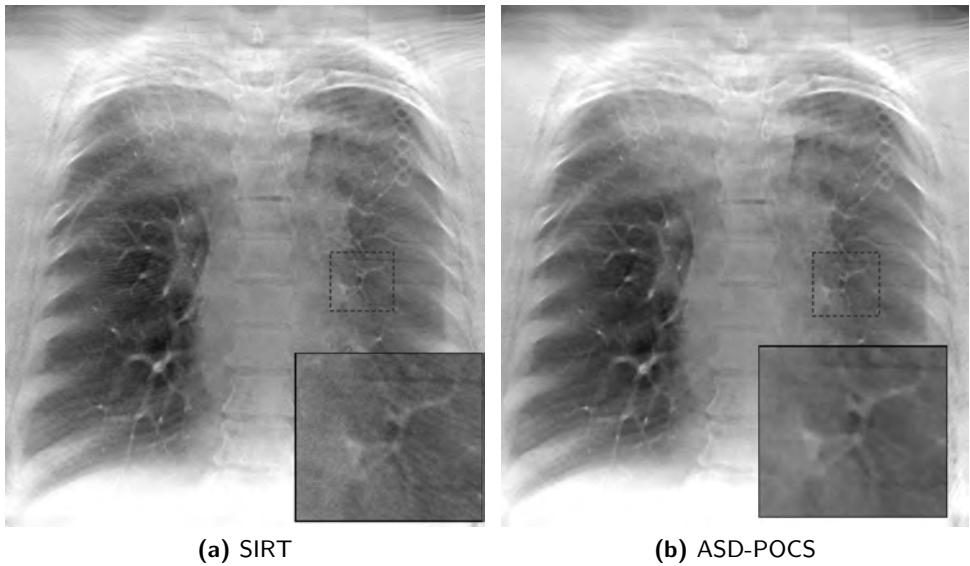


Figure 2.7: Reconstruction of 11 projections of an antropomorphic phantom. (a) SIRT, (b) ASD-POCS, both with insets (bottom right) of enlarged region within the image, indicated with dashed line. Note the reduced noise in the ASD-POCS inset compared to the SIRT inset.

3

Continuous tomosynthesis

Contents

3.1	Introduction	32
3.2	Methods	33
3.3	Experiments	37
3.3.1	Resolution phantoms	37
3.3.2	Forbild phantom	39
3.3.3	Synchrotron measurements	40
3.3.4	Continuous tomosynthesis	40
3.4	Results	41
3.4.1	Resolution phantoms	41
3.4.2	Forbild phantom	43
3.4.3	Synchrotron measurements	49
3.4.4	Continuous tomosynthesis	51
3.5	Discussion	52
3.6	Conclusion	54
3.7	Linearization of forward projector	54
	References	55

Insufficient angular sampling leads to streak and ringing artifacts in the reconstruction. In this chapter, an alternative method is proposed to improve the angular sampling (and hence reduce the ringing artifacts), in a central region of the image. The proposed method is based on a continuously moving and radiating X-ray source. The continuous motion of the tube causes blurring in the projections, which is subsequently modeled in the reconstruction. The method is first described for CT imaging, and then transferred to tomosynthesis imaging.

3.1 Introduction

Computed tomography (CT) is increasingly used to study dynamic processes, often referred to as 4D CT. The time resolution with which such processes can be studied strongly depends on the rotation speed of the gantry. Pushing the rotation speed to its limits, however, may result in blurred X-ray projections depending on the type of acquisition, which in turn leads to blurring in the reconstructed images [? ?].

In a *step-and-shoot* acquisition setup, the X-ray source and detector are stepwise moved on a predefined path and kept still during the exposure [?]. While this approach yields sharp projection images, precisely controlling, moving and stopping the X-ray source is challenging. As a result, the focal spot often still moves during exposure, which causes blurring in the reconstructed images [?]. In addition, step-and-shoot protocols typically lead to longer acquisition times [?].

An alternative acquisition strategy is to keep the gantry in a constant motion, a so called *continuous* acquisition mode. This mode allows shorter acquisition times, but also suffers from blurred projection data, even if a pulsed X-ray source is employed, as the gantry is still moving during the pulse. A related blurring effect is caused by detector lag, where the detector still partly contains the signal of the previous exposure and hence also appears to store photon beams from multiple angles [?].

Most acquisition protocols are designed to limit the angular integration as much as possible, either by increasing the detector frame rate [? ?], by reducing the rotation speed of the gantry, or by decreasing the exposure time of the X-ray pulse [? ?]. Recently, efforts have been made to model the focal spot motion during these X-ray flashes in the reconstruction algorithm to improve the reconstruction quality [?]. Another previous approach to reduce the angular integration consisted of a pixel shifting technique [?]. Closely related to angular integration, overlapping beams were modeled originating from multiple sources in [?].

While reducing blurring effects has obvious advantages, the main consequence seems to be prolongation of the acquisition time. An alternative approach, which

we will follow in this paper, consists of accurately modeling the blurring effect and integrating it in an image reconstruction framework. Iterative reconstruction methods are known to be suitable to model various physical effects, such as the focal spot size, the beam energy spectrum, the finite detector elements, etc[?]. In this work, the blurring due to gantry rotation during the acquisition of a single projection is modeled and integrated into a novel acquisition/reconstruction method: the Algebraic Reconstruction Technique with angular Integration Concept (ARTIC). ARTIC is based on the continuous acquisition mode as described above, but using a continuously emitting X-ray source instead of a pulsed source. The continuously emitting source causes deliberate angular integration of the X-rays along its full motion path from the start of the exposure until the start of the next exposure. Thus for a given total scan angle, the angle of integration increases with decreasing number of projections. Opposed to conventional reconstruction methods, in ARTIC, the angular integration is modeled and integrated into an iterative reconstruction scheme. The performance of ARTIC in terms of image reconstruction quality is evaluated on simulation phantoms and real datasets.

3.2 Methods

In this section, we explain the concept of continuous projections for parallel beam geometry. Generalization to other geometries is straightforward. In what follows, a point source and point detector are assumed.

The attenuation of an X-ray beam in the case of a pulsed X-ray source, further referred to as a 'static' projection, can be expressed as follows:

$$I_n^s(r) = I_0 \exp \left(- \int_{L_{r,\theta_n}} \mu(x,y) ds \right) \quad (3.1)$$

with $(x, y) = (r \cos \theta_n - s \sin \theta_n, r \sin \theta_n + s \cos \theta_n)$. Furthermore, I_0 is the intensity measured by the detector without object and I the intensity after attenuation by the object. The attenuation coefficients of the imaged object are represented by $\mu(x, y)$, and the line integral is taken over the X-ray beam L_{r,θ_n} from source to detector as illustrated in Fig. 3.1a.

After transformation of the projection data by $-\ln(I_n^s(r)/I_0)$ and discretization, Eq. (3.1) can be expressed as a linear combination of the attenuation coefficients:

$$b_i = \sum_j a_{i,j}^s x_j \quad (3.2)$$

where b_i represents the measured projection data at detector position i and x_j is a pixel in the discrete representation of μ . The contribution of image pixel j to

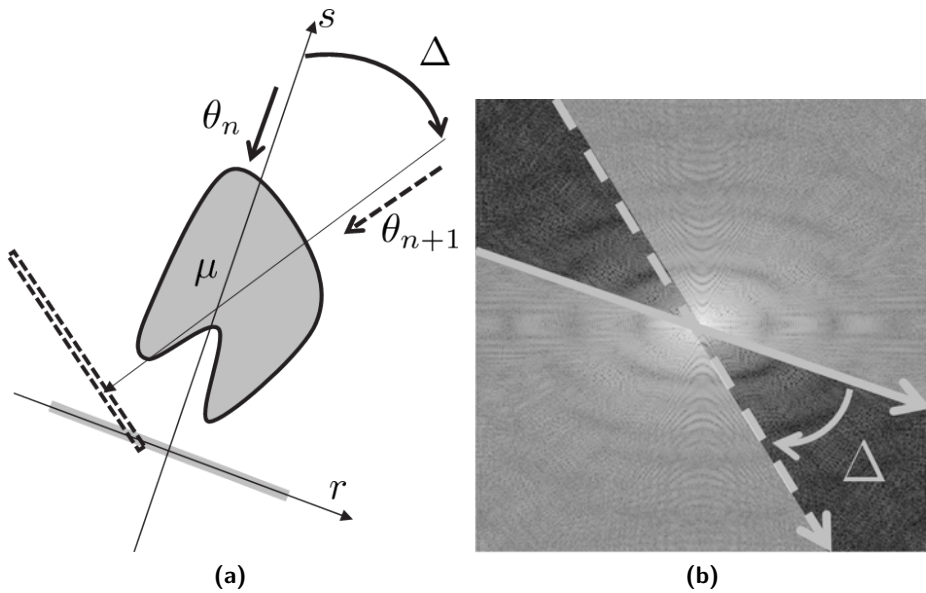


Figure 3.1: (a) shows an example image acquisition geometry. Parallel beam projections are acquired at angles $\theta_n = n\Delta$ with $n = 1, \dots, N$. (b) shows the corresponding lines of these projections in the Fourier space. In a *continuous* acquisition, the detector integrates photons between θ_n and θ_{n+1} and hence gathers information about a wedge of angular width Δ in the Fourier space.

detector value b_i is $a_{i,j}^s$, which is related to the intersection length of the ray with this pixel.

The combination of Eq. (3.2) for all projection pixels leads to a system of linear equations

$$\mathbf{b} = \mathbf{A}^s \mathbf{x} \quad (3.3)$$

where $\mathbf{A}^s = \{a_{i,j}^s\}$ represents the system matrix, $\mathbf{x} = \{x_j\}$ the vector of unknown attenuation coefficients in the discrete representation of μ and $\mathbf{b} = \{b_i\}$ the vector of the projection data.

In case of continuous projections, each projection value $I_n^c(r)$ is the result of the integration of photons during rotation of the source-detector system from θ_n to $\theta_{n+1} = \theta_n + \Delta$. An equivalent approach can be described with a fixed source-detector system and a continuously rotating object, e.g. in synchrotron imaging. In this case, θ refers to the rotation of the object instead of the source-detector system. If the same total radiation dose is administered and the X-ray source and detector move with constant angular velocity, the measured intensity is given by:

$$I_n^c(r) = \frac{I_0}{\Delta} \int_{\alpha=\theta_n}^{\theta_{n+1}} \exp\left(-\int_{L_{r,\alpha}} \mu(x,y) ds\right) d\alpha \quad (3.4)$$

with $(x,y) = (r \cos \alpha - s \sin \alpha, r \sin \alpha + s \cos \alpha)$. For simplicity, we assume the source emits a constant intensity. Also, the delay for reading out the detector is assumed to be negligible compared to the integration time.

To obtain a discrete formulation of Eq. (3.4), S number of rays are projected between θ_n and θ_{n+1} . Eq. (3.2) is modified to:

$$b_i = -\ln\left(\frac{1}{S} \sum_{s=1}^S \exp\left[-\sum_j a_{i,j,s} x_j\right]\right) \quad (3.5)$$

where $a_{i,j,s}$ now represents the weight of the attenuation coefficient at image pixel j for the beam arriving at detector pixel i with angle $\theta_n + \frac{s}{S} \Delta$. The sampling factor S should be chosen high enough to sample the full area between the corresponding lines in the Fourier space as illustrated in Fig. 3.1b.

Furthermore, under the assumption (see Appendix 3.7) that each ray sum $b_{i,s} \equiv \sum_j a_{i,j,s} x_j$ only differs slightly from the average ray sum $b_{i,avg} \equiv \frac{1}{S} \sum_{s=1}^S b_{i,s}$, Eq. (3.5) can be approximated using the fact that $\exp(x) \approx 1 + x$ for small x :

$$\begin{aligned}
 b_i &= -\ln \left(\frac{1}{S} \sum_{s=1}^S \exp(-b_{i,s}) \right) \\
 &= -\ln \left(\frac{1}{S} \sum_{s=1}^S \exp(b_{i,avg} - b_{i,s} - b_{i,avg}) \right) \\
 &= -\ln \left(\frac{1}{S} \sum_{s=1}^S \exp(b_{i,avg} - b_{i,s}) \exp(-b_{i,avg}) \right) \\
 &= b_{i,avg} - \ln \left(\frac{1}{S} \sum_{s=1}^S \exp(b_{i,avg} - b_{i,s}) \right) \tag{3.6}
 \end{aligned}$$

$$\begin{aligned}
 &\approx b_{i,avg} - \ln \left(\frac{1}{S} \sum_{s=1}^S [1 + (b_{i,avg} - b_{i,s})] \right) \\
 &= b_{i,avg} \\
 &= \sum_j a_{i,j}^c x_j \tag{3.7}
 \end{aligned}$$

with $a_{i,j}^c \equiv \frac{1}{S} \sum_{s=1}^S a_{i,j,s}$.

In this work, we use the linear approximation of Eq. (3.7) to model the forward continuous projection, which leads to the following linear system:

$$\mathbf{b} = \mathbf{A}^c \mathbf{x} \tag{3.8}$$

where $\mathbf{A}^c = \{a_{i,j}^c\}$ represents the system matrix for the continuous projections.

The linear system in Eq. (3.8) can then be solved by different techniques. In the remainder of this work, the Simultaneous Iterative Reconstruction Algorithm (SIRT) is chosen as an example implementation. In SIRT, the update step can be written as [?]:

$$\mathbf{x}^{(k+1)} = \mathbf{x}^{(k)} + \mathbf{C} \mathbf{A}^T \mathbf{R} (\mathbf{b} - \mathbf{A} \mathbf{x}^{(k)}) \tag{3.9}$$

with \mathbf{A} the system matrix, and \mathbf{R} and \mathbf{C} diagonal matrices, consisting of the inverse row and column sums of \mathbf{A} , respectively. The reconstructed image in iteration k is represented by $\mathbf{x}^{(k)}$. In this work, we will further refer to ‘ARTIC’ for solving the continuous projections system in Eq. (3.8) with SIRT, as opposed to ‘SIRT’ for solving the static projections system in Eq.(3.3) with SIRT.

3.3 Experiments

Section 3.3.1 describes experiments with resolution phantoms. In Section 3.3.2 we describe a simulation experiment using the Forbild [?] phantom. In Section 3.3.3 we perform an experiment on real data, acquired with a synchrotron.

3.3.1 Resolution phantoms

To compare the reconstruction quality in a region of interest (ROI) between Filtered Back Projection (FBP) [?], SIRT and ARTIC, a phantom was created consisting of non-overlapping randomly placed Gaussian blobs with radius 10px and a maximal intensity of 1, which decreases to 0 towards the border of the dot. (Fig. 3.2a). The phantom dimensions were 700px \times 700px. All projections were simulated using parallel beams, with projection angles equally distributed over 180°. The detector contained 525 elements with a relative pixel width of 2 compared to the phantom pixels. Reconstructions were computed on a grid of size 350px \times 350px. To measure the reconstruction quality in a ROI, the following local Root Mean Square Error (RMSE) was defined:

$$RMSE(r) \equiv \sqrt{\frac{1}{|D(r)|} \sum_{j \in D(r)} (x_j - \hat{x}_j)^2} \quad (3.10)$$

where x_j represents the j th pixel of the phantom, \hat{x}_j is the j th pixel of the reconstructed image, and $D(r)$ is the set of pixels within a circular ROI of relative radius r around the source-detector rotation center, and $|D(r)|$ is its cardinality. A relative radius $r = 1$ corresponds to a circular field of view with a radius of half the image width. To exclude differences in convergence speed between both methods, reconstruction iterations were stopped at the iteration at which the reconstructed image showed a minimal RMSE in a ROI of $r = 0.5$.

In a first experiment, the relationship between the number of projections and ROI size was investigated. Reconstructions were made using 20, 40 and 60 simulated projections with moderate noise ($I_0 = 10^5$). The RMSE was measured in function of the size of the ROI around the rotation center.

Secondly, to compare the noise propagation of SIRT and ARTIC through subsequent iterations, 3 sets of 30 noisy projections with $I_0 = 5 \times 10^3, 10^4, 10^5$ were simulated. The RMSE of the reconstruction was evaluated in function of the number of iterations in a ROI with radius $r = 0.5$.

Third, to illustrate the possible gain in total acquisition time, the RMSE was computed as a function of the number of projections. Moderate noise was added ($I_0 = 10^5$) and both SIRT and ARTIC reconstructions were again stopped at the

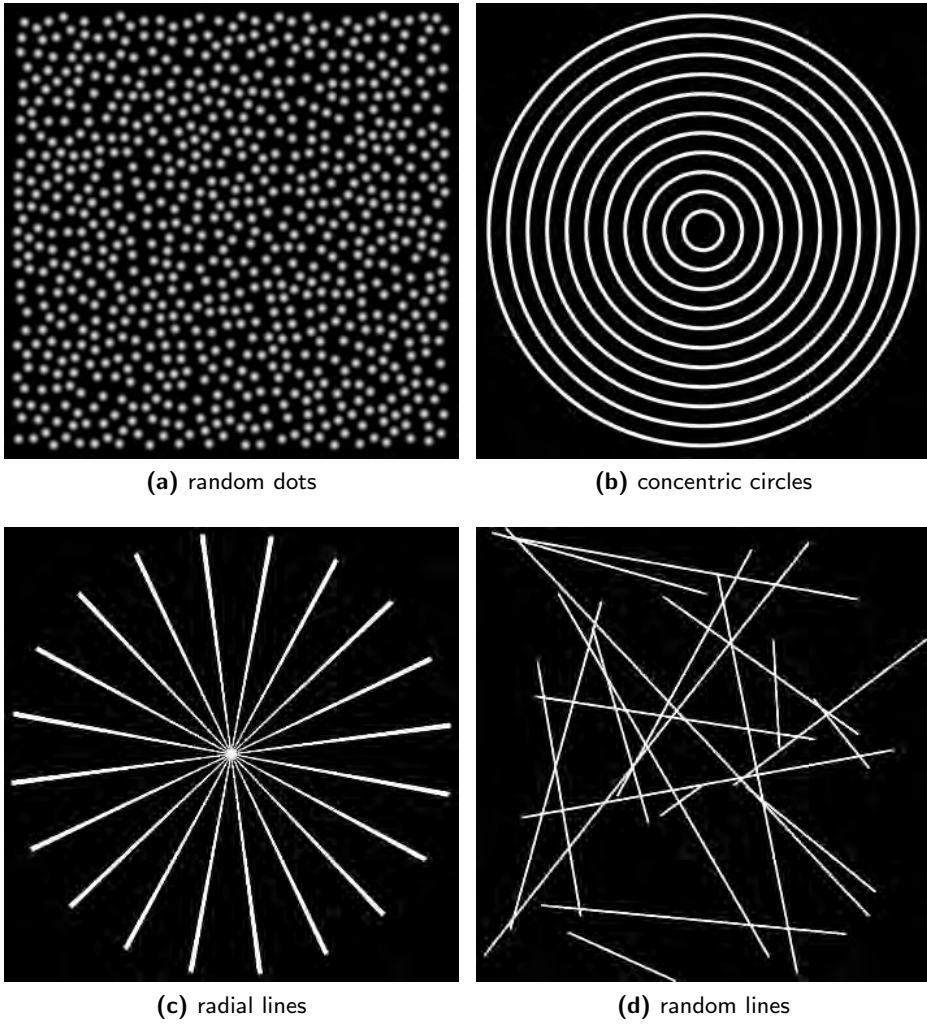


Figure 3.2: Phantoms for evaluation of the spatial resolution.

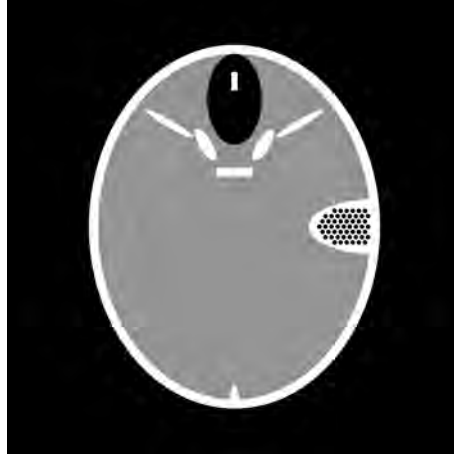


Figure 3.3: Forbild phantom.

iteration with minimal RMSE.

The phantom images in Figs. 3.2b, 3.2c and 3.2d were designed to illustrate the local radial and angular resolution of ARTIC. Pixel intensities are within $[0,1]$. Phantom dimension, reconstruction grid, detector size and geometry were identical to the random dots phantom experiments. FBP, SIRT and ARTIC reconstructions were computed from 20 noiseless projections.

3.3.2 Forbild phantom

Simulation experiments were run using the Forbild phantom (Fig. 3.3). For the simulation of the continuous projections of the anthropomorphic phantoms, Eq. (3.5) was used to allow validation of the linearization in the reconstruction algorithm in Eq. (3.7).

The Forbild phantom was generated on a 351×351 pixels grid with pixels of size $75\mu\text{m}$. Projections were simulated with 45 parallel beams, equally distributed over 180° , on a detector of 527px width to avoid truncation. Moderate noise ($I_0 = 10^5$) was added to the projections. Reconstructions were computed with FBP, SIRT and ARTIC for different source-detector rotation centers and the RMSE was evaluated around the rotation center for different ROI sizes r . All reconstruction iterations were stopped at the iteration for which the RMSE in a ROI with $r = 0.3$ was minimal.

3.3.3 Synchrotron measurements

We evaluated our method on two sets of parallel beam projections of an Al8Cu metal rod, made with a synchrotron. The angles of both sets were equally distributed over 180° . The first set consisted of 1000 continuous projections and was considered the reference set. The second set contained only 125 continuous projections.

We reconstructed the set of 1000 projections with SIRT, ignoring the small angular integration, and used it as a reference image. Then we reconstructed the set of 125 continuous projections with FBP, SIRT and ARTIC, and compared the RMSE with the reference image after rigid registration. We set r to cover the full metal rod excluding the background. We also computed the Structural Similarity Index (SSI) [?] with the reference image for the same region.

3.3.4 Continuous tomosynthesis

As a final experiment, continuous tomosynthesis is investigated using the XCAT [?] phantom. Step-and-shoot and continuous projections were simulated, both covering 10 projections in an angular range of 40° . Detector and X-ray source moved in parallel planes on opposite sides of the phantom, as illustrated in Fig. 3.4. The source image distance was set to 1200mm and the rotation center of the source and detector motion was placed in the middle of the phantom. Poisson noise was simulated in both sets of projections, assuming an incident photon count of $I_0 = 100000$. The step-and-shoot and continuous projections were reconstructed with SIRT and ARTIC respectively, using the open source ASTRA toolbox [? ?].

Conventional reconstructions from a limited angle suffer from limited depth resolution, even when a high amount of noiseless projections are provided. Especially structures with edges which are, due to the limited angle, not oriented parallel to the direction of incoming rays [?] in any projection, are almost invisible in the reconstructed image. The red arrow in Fig. 3.5a illustrates such a structure. The goal of this experiment however, is not to improve depth resolution. In this experiment, the primary goal is to reduce the number of projections and thus increase the acquisition speed by continuous motion and emission of the X-ray tube and detector. Therefore, a SIRT reconstruction from 300 noiseless projections from the same angular range of 40 was computed and is further considered as the reference. This reference reconstruction still contains reconstruction artifacts, due to the limited angle acquisition, as can be observed in Fig. 3.5b. A reduction of the number of projections and the addition of noise will further reduce the reconstruction quality. In this experiment, conventional SIRT and ARTIC reconstructions using only 10 noisy step-and-shoot resp. continuous projections are compared to

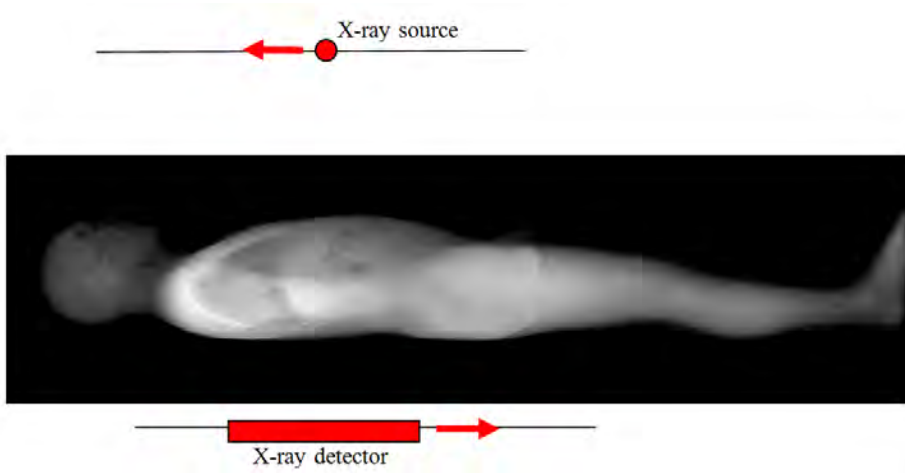


Figure 3.4: Geometry for the experiment with the XCAT phantom. A flat panel detector moves continuously in a plane underneath the phantom, while the X-ray source moves in opposite direction in a plane above the phantom.

this reference reconstruction.

3.4 Results

3.4.1 Resolution phantoms

Fig. 3.6 shows reconstructions from FBP, SIRT and ARTIC for an increasing number of projections. Whereas the resolution is not spatially dependent for FBP and SIRT, the results from ARTIC clearly show an improved resolution in a local region around the rotation center, with a decreasing tangential resolution further away from the rotation center. The radius of this local region increases with the number of projections.

Fig. 3.7 shows the RMSE in function of the radius r of the ROI. A substantial improvement is observed with ARTIC for regions with radius $r < 1$. For increasing ROI radius r , the RMSE of SIRT and ARTIC gradually converges towards approximately the same global RMSE. The difference in RMSE between SIRT and ARTIC reconstructions also lowers with increasing number of projections, which can be understood intuitively as this reduces the angular integration. To illustrate the spatial dependency of the RMSE in ARTIC reconstructions, Fig. 3.8 displays the RMSE in a ring of width 0.2 and outer radius r . Around $r = 0.75$ and above, the

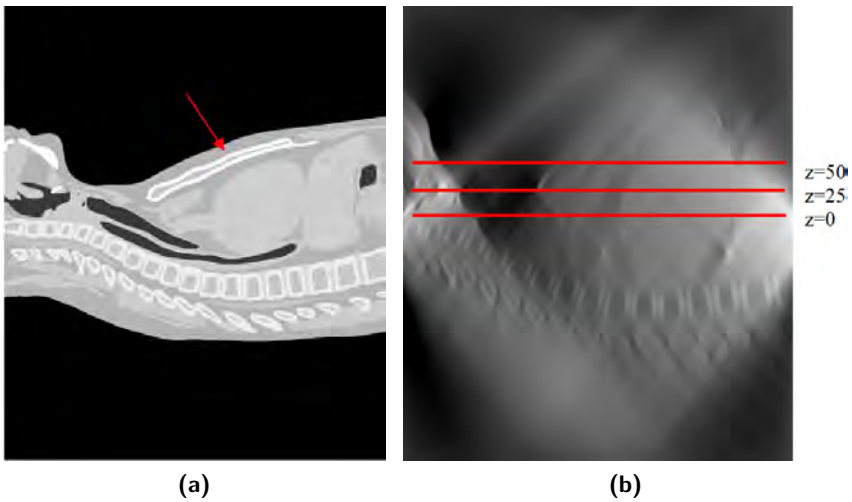


Figure 3.5: (a) sagittal (side) view through the middle of the XCAT phantom. The arrow indicates a structure with edges perpendicular to the incoming rays. (b) sagittal view through the reference SIRT reconstruction with 300 noiseless projections, showing limited depth resolution. The red lines indicate the location of the 3 reference slices at different depths. The slice at $z=0$ represents the slice in the rotation center of the continuous tube-detector motion.

RMSE of ARTIC is higher than the RMSE of SIRT.

The RMSE of a fixed ROI ($r = 0.5$) in function of the iterations is plotted in Fig. 3.9 for a fixed number (30) of projections. As can be observed, the RMSE of ARTIC reconstructions increases faster after the optimal stopping iteration compared to SIRT. This illustrates the stronger noise propagation of ARTIC compared to SIRT.

The RMSE in a fixed ROI with radius $r = 0.5$ is displayed in Fig. 3.10. Note that the RMSE of ARTIC at 30 projections is similar to the RMSE of SIRT at 60 projections, showing its potential for reduction of the scan time.

The reconstructions from projections of the circles phantom (Fig. 3.11a) are displayed in the first row of Fig. 3.11. Whereas the FBP (Fig. 3.11b) and SIRT reconstruction (Fig. 3.11c) show many artifacts, the ARTIC reconstruction is nearly perfect (Fig. 3.11d). This demonstrates the improved radial resolution of ARTIC.

The radial lines phantom (Fig. 3.11e) contains lines through the center of rotation and was specifically designed to illustrate the decreased tangential resolution of ARTIC. Compared to the FBP (Fig. 3.11f) and SIRT reconstruction (Fig. 3.11g), the ARTIC reconstruction (Fig. 3.11h) shows substantial angular blurring with increasing distance from the rotation center. The angle of this blurring corresponds to the covered angle of the continuous projections. Note that the radial lines phantom illustrates the worst effect of the angular blurring. Fig. 3.11i shows the ARTIC reconstruction of a phantom consisting of lines with random orientations (Fig. 3.11i).

3.4.2 Forbild phantom

The reconstructions with FBP, SIRT and ARTIC using two different rotation centers of the Forbild phantom are displayed in Fig. 3.12. Both SIRT reconstructions had minimal RMSE at 148 iterations, whereas the ARTIC reconstruction iterations stopped at 404 (left), and 1090 (right) iterations. Compared to the FBP (Fig. 3.12a) and SIRT (Fig. 3.12c) reconstructions, the ARTIC reconstruction (Fig. 3.12e) with rotation center in the left of the image shows greater detail and less artifacts in the region around the rotation center. This is reflected in the RMSE, which is displayed in Table 3.1. At the other side of the phantom the matrix of black holes suffers from angular blurring. Moving the rotation center to this black holes region on the right improved the result in this region for ARTIC (Figs. 3.12f and 3.13), but resulted in a smaller improvement compared to FBP (Fig. 3.12b) and SIRT (Fig. 3.12d).

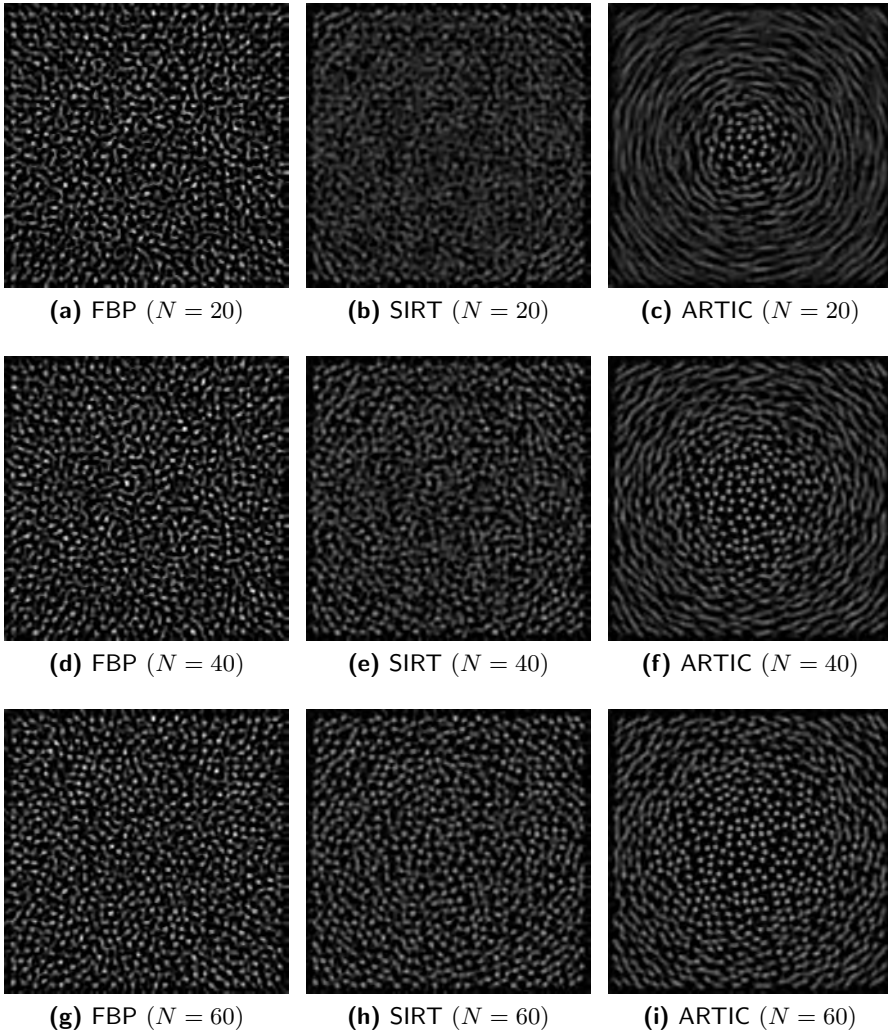


Figure 3.6: Reconstructions with FBP (left column), SIRT (middle column) and ARTIC (right column) of the random dots phantom for 20, 40 and 60 projections. Displayed grayscale set to $[0,1]$.

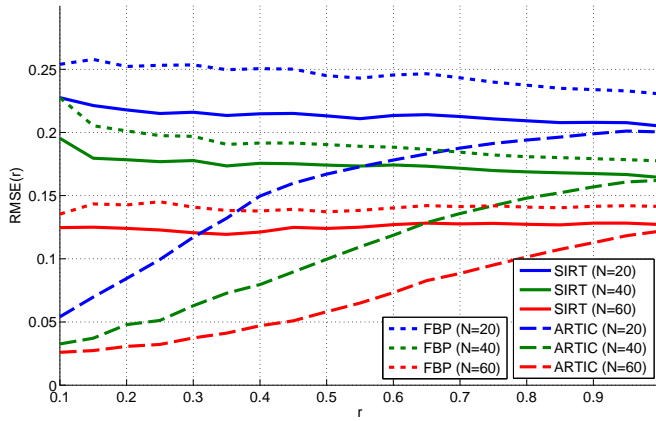


Figure 3.7: RMSE in circular ROI with increasing radius r , for various FBP, SIRT and ARTIC reconstructions of the random dots phantom.

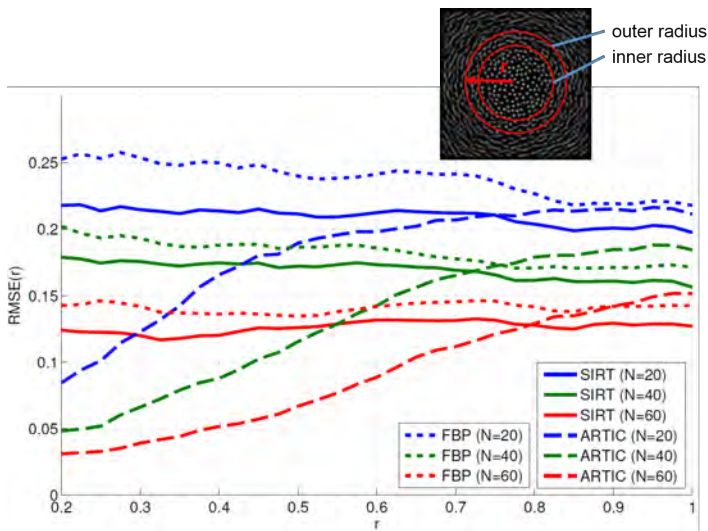


Figure 3.8: RMSE in a circular ring of width 0.2 and outer radius r for various FBP, SIRT and ARTIC reconstructions of the random dots phantom.

CHAPTER 3. CONTINUOUS TOMOSYNTHESIS

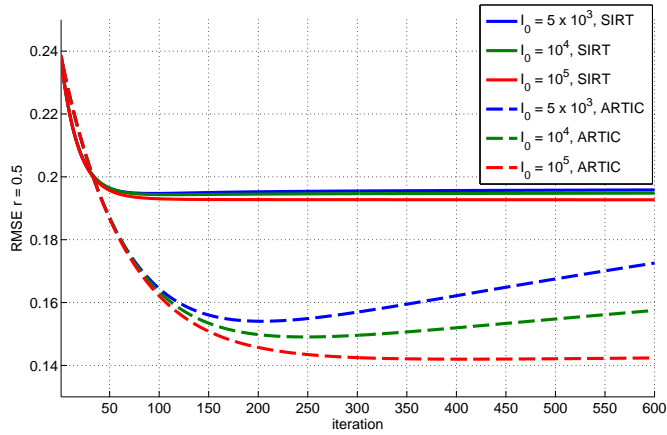


Figure 3.9: RMSE ($r = 0.5$) in function of the number of iterations, for various noise levels and $N = 30$.

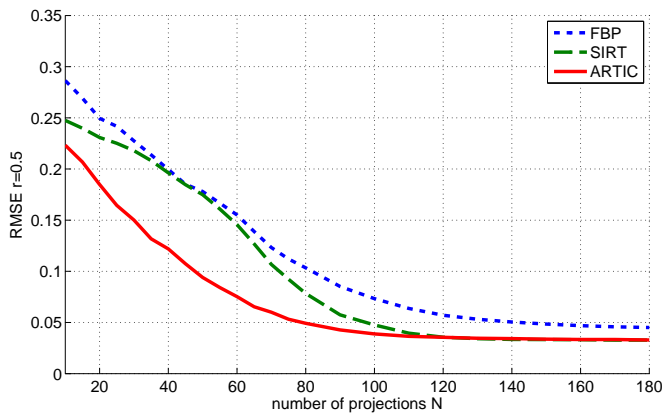


Figure 3.10: RMSE ($r = 0.5$) of FBP, SIRT and ARTIC reconstructions in function of the number of projections.

Rotation center	$r = 0.15$			$r = 0.30$		
	FBP	SIRT	ARTIC	FBP	SIRT	ARTIC
left	0.299	0.087	0.039	0.279	0.107	0.061
right	0.434	0.518	0.336	0.338	0.302	0.215

Table 3.1: Local RMSE for reconstructions of the Forbild phantom with various ROI radius r .

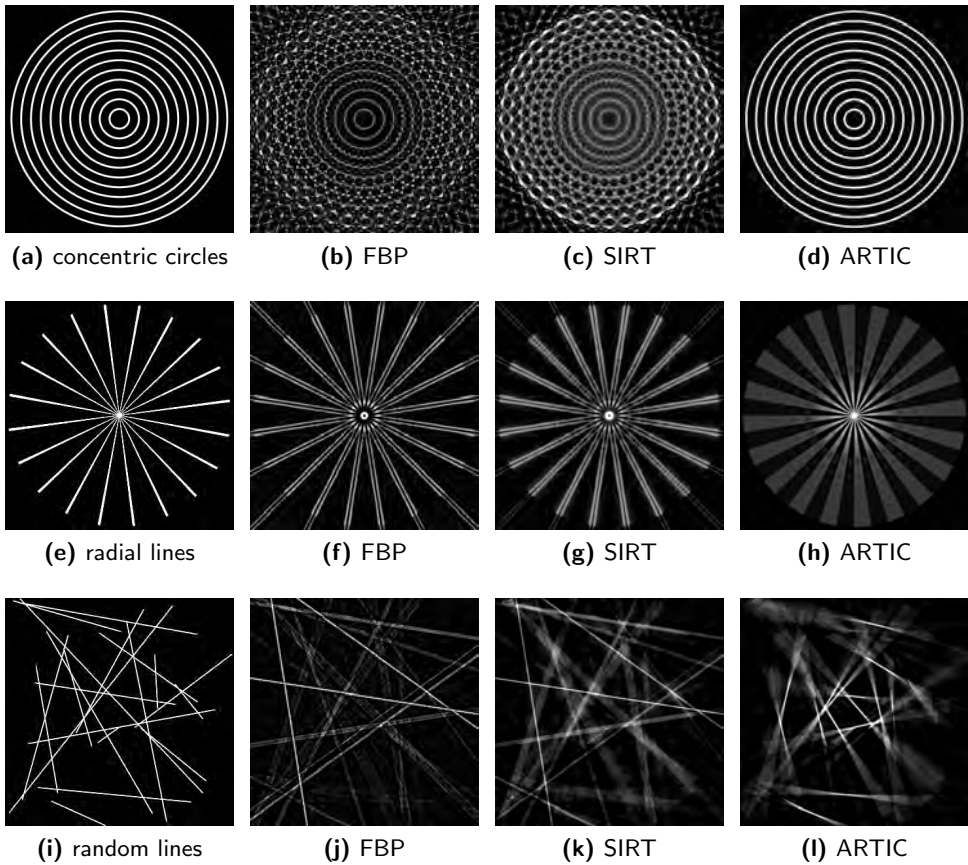


Figure 3.11: Reconstructions of the circles phantom (a), radial lines phantom (e) and random lines phantom (i) with FBP, SIRT and ARTIC. Grayscale displayed at $[0,0.5]$ for increased contrast. $N = 20$ for all reconstructions.

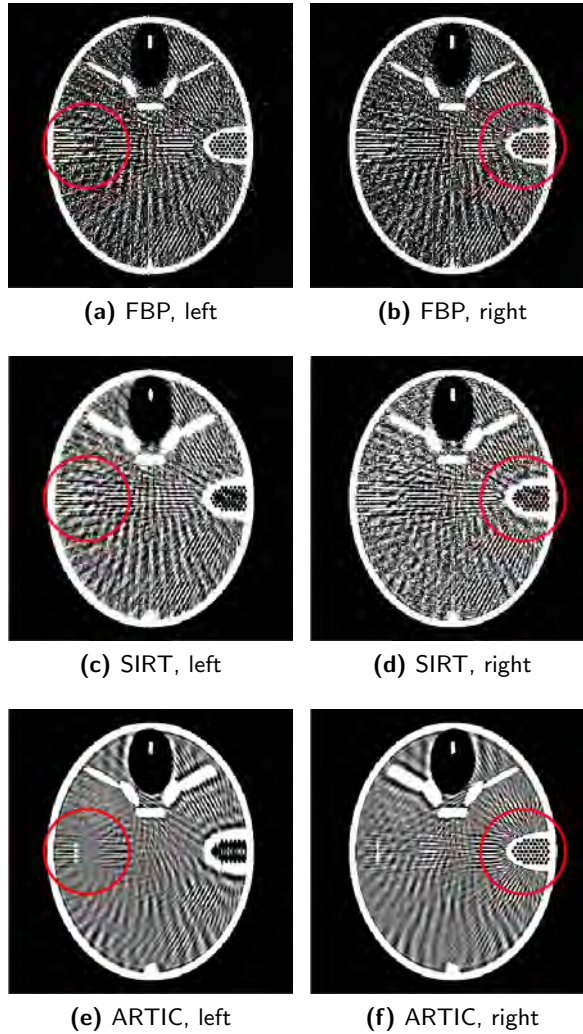


Figure 3.12: Reconstructions from 45 projections of the Forbild phantom with rotation center at the left (left column) and right (right column) of the phantom. All images displayed with grayscale $[-50,150]$ HU. The red circle indicates the border of the ROI around the rotation center with radius $r = 0.3$.

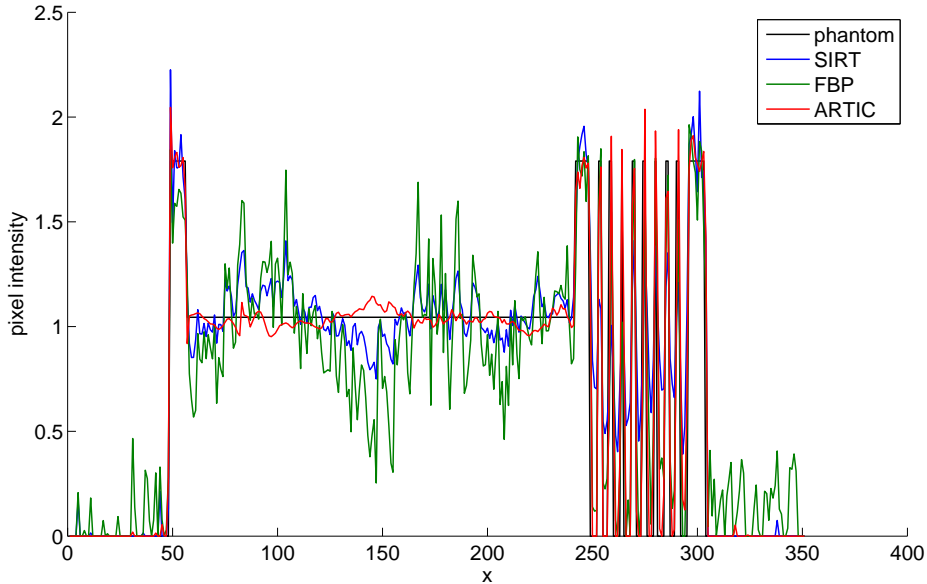


Figure 3.13: Profiles through the middle line of FBP, SIRT and ARTIC reconstructions of the Forbild phantom. Rotation center was in the black holes region on the right of the phantom.

3.4.3 Synchrotron measurements

The reconstructions with FBP, SIRT and ARTIC from the synchrotron images are displayed in Fig. 3.14. The lowest RMSE for SIRT was at 200 iterations, and for ARTIC at 400 iterations. Compared to the FBP reconstruction in Fig. 3.14a, the ARTIC reconstruction (Fig. 3.14c) shows less noise and a higher contrast in the outer region of the object. In the region close to the rotation center, less differences can be observed. This is due to the relatively high number of 125 projections. The SIRT reconstruction (Fig. 3.14b) shows an overall lower contrast than the ARTIC reconstruction.

Table 3.2 shows the quantitative analysis of the reconstructions with the reference image. An improvement is observed for ARTIC, which modeled the relative movement of object and source-detector system during the acquisition of the projections into the reconstruction, compared to FBP and SIRT which ignored the movement.

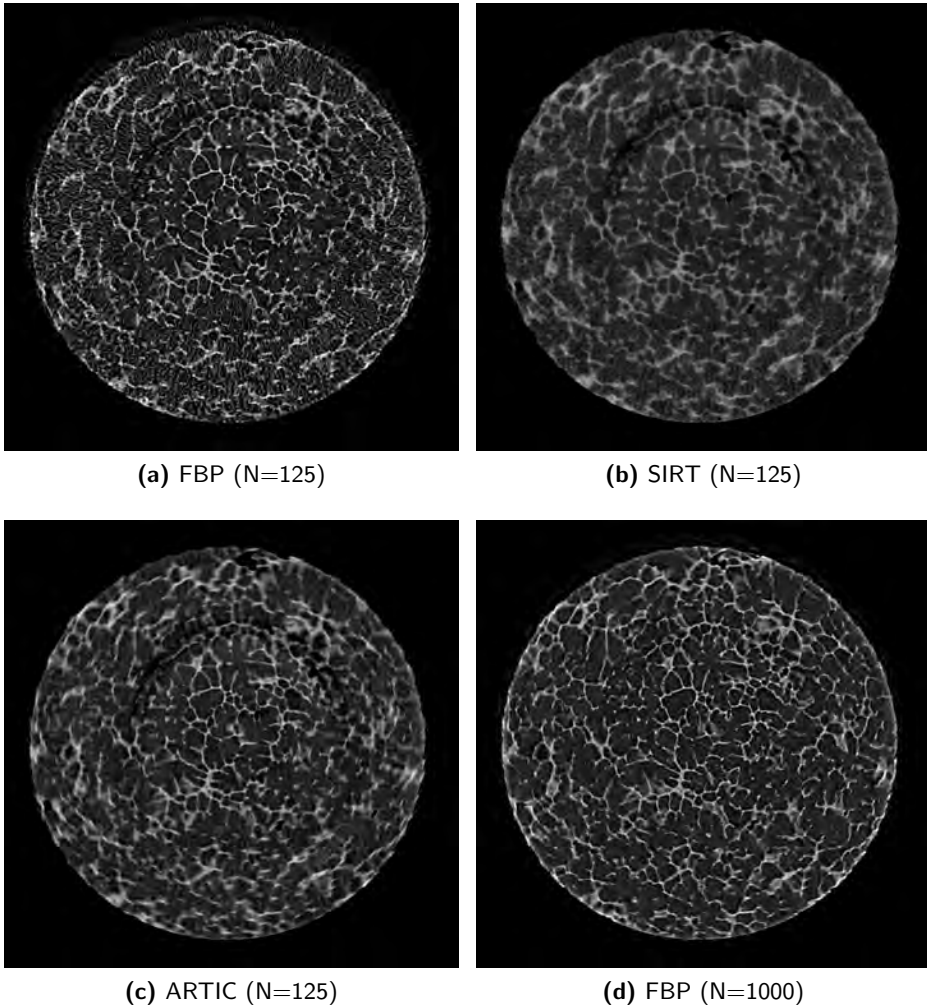


Figure 3.14: Reconstruction of 125 continuous projections of Al₈Cu sample using FBP (a), SIRT (b) and ARTIC (c). (d) shows the reference image, reconstructed with FBP for (N=1000). All images are displayed at the same grayscale.

Reconstruction method	RMSE	SSIM
FBP	0.1553	0.7947
SIRT	0.1417	0.7644
ARTIC	0.1088	0.8273

Table 3.2: RMSE and structural similarity index (SSIM) for FBP, SIRT and ARTIC reconstructions of 125 continuous projections of the Al8Cu sample.

3.4.4 Continuous tomosynthesis

Both SIRT and ARTIC reconstructions were stopped at the iteration during which the middle slice reached the lowest root mean squared error (RMSE) compared to the reference reconstruction with 300 noiseless projections. The RMSE per slice of both SIRT and ARTIC reconstructions is displayed in Fig. 3.15. The largest improvement in RMSE is observed near the rotation center.

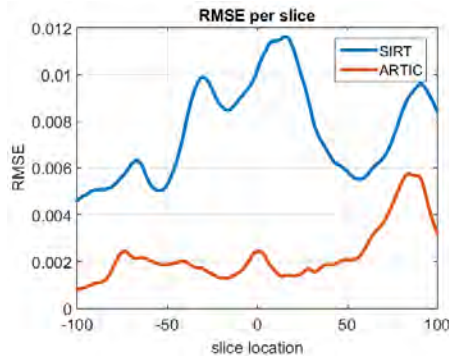


Figure 3.15: RMSE per slice

The reference reconstruction and the resulting SIRT and ARTIC reconstructions are displayed in Fig. 3.16. Note how, despite the limited depth resolution, the reference reconstruction is still capable of providing high resolution section images (Figs. Fig. 3.16 (a),(d),(g)). The reduction of the number of projections causes blurring and ringing artifacts in the SIRT reconstruction, which are caused by streak artifacts in the Z dimension. Furthermore, truncation artifacts can be observed near the top and bottom of the SIRT reconstruction at a depth of $z=50$. The ARTIC reconstruction near the rotation center are displayed in Figs. Fig. 3.16 (c),(f),(i)).

The experiment illustrates that the SIRT reconstruction quality in the slices near the rotation center (Fig. 3.16e) is substantially improved by ARTIC (Fig. 3.16f),

whereas in slices further away from the rotation center ARTIC shows increased blurring in the direction of the tube motion (Fig. 3.16i) compared to SIRT (Fig. 3.16h). The RMSE shows a large improvement on slices near the rotation center, but also moderate improvements away from the center with ARTIC. As the phantom content varies strongly between slices, the slice location dependent resolution of this technique should be more thoroughly evaluated with a resolution phantom or MTF measurements in future work.

3.5 Discussion

A relatively slow detector that limits the number of projections to maintain temporal resolution, can for example be found in systems where a flat panel detector is used to capture X-rays [?] from a patient holding his breath. Other examples include synchrotron imagers, where the rotation speed of a sample is limited by the detector read out time.

To avoid reconstruction artifacts, a set of projection images for reconstructing an image should consist of a large number of projections from all angles [?]. For a parallel beam geometry, the central slice theorem states that the Fourier transform of a 1D projection of an image corresponds to a line in the Fourier transform of the image [?]. A reconstruction from only a few projections therefore suffers from the well known streak artifacts, due to insufficient information about the Fourier space.

Often applied techniques to deal with few view artifacts are based on compressed sensing, where prior knowledge about the object is incorporated into the reconstruction by a regularization term, which steers the reconstruction towards a more desired result. A typical example of prior knowledge is the assumption that the object can be described by a piecewise constant function, expressed by a low total variation of the image[?], or a minimal distance to a high resolution prior reconstruction[?]. In our work, we applied no prior knowledge about the object in the reconstruction other than modeling the continuous acquisition.

In Fig. 3.1, the n th continuous projection integrates all rays between the angles θ_n and $\theta_n + \Delta$ and thus gathers information from the entire area in the Fourier space between the two angles of the static projections. This reduces the typical streak artifacts caused by reconstructing with too few projections, however at the cost of a decreasing tangential resolution outside the rotation center as discussed in the previous sections. Any form of regularization with prior knowledge could easily be integrated with ARTIC, depending on the type of object being reconstructed.

If detectors are fast enough, distributing the total radiation dose over a high number of $S \times N$ static projections with unattenuated beam intensity I_0/S results in a better overall reconstructed image quality than reconstructing from a

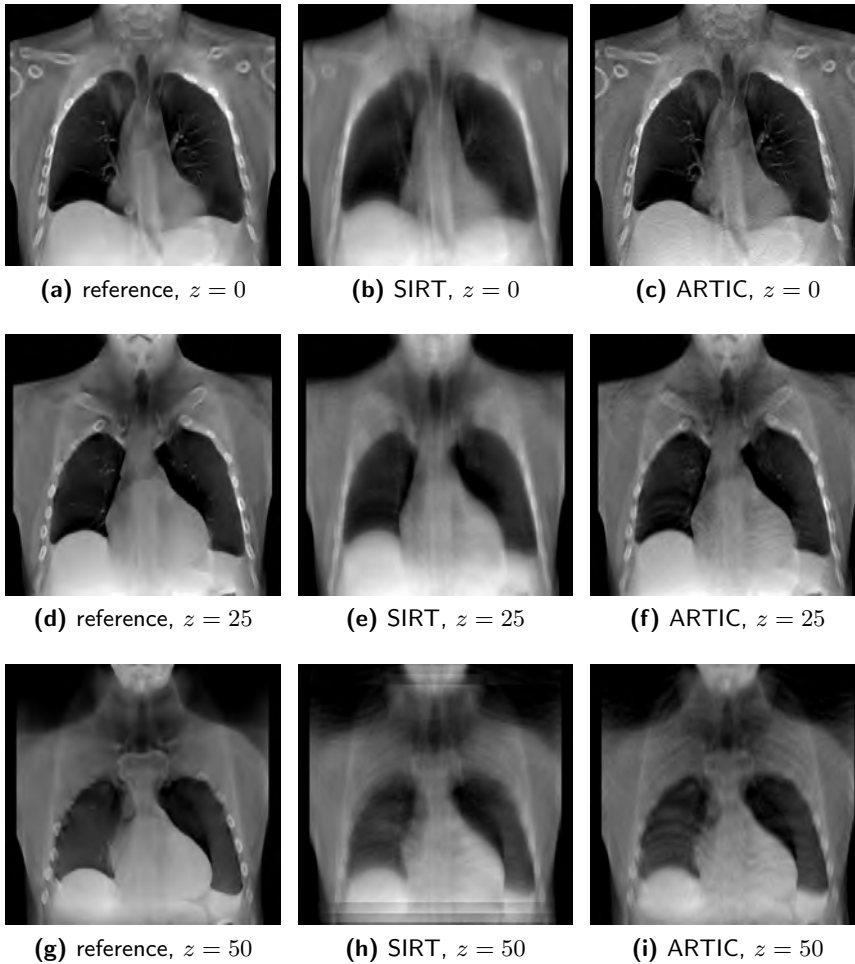


Figure 3.16: Reconstructions of the XCAT phantom, all taken with angular range of 40. First column: SIRT reconstruction from 300 noiseless projections (considered the reference image). Middle column: SIRT reconstructions from 10 noisy step-and-shoot projections. Right column: ARTIC reconstructions from 10 noisy continuous projections.

few number N continuous projections with beam intensity I_0 . In this case, the advantage of ARTIC reduces to a smaller memory footprint of the algorithm on a computing device, as it requires the storage of only a few projection images.

3.6 Conclusion

We propose ARTIC (Algebraic Reconstruction Technique with angular Integration Concept), a reconstruction method for projections that were acquired with a continuously rotating and continuously emitting X-ray source, which causes blurring in the projection images due to the angular integration of the X-ray beams. Compared to conventional reconstruction from a limited number of projections acquired with a pulsed X-ray source, ARTIC improves the resolution in the local neighborhood around the source detector rotation center, at the cost of decreasing tangential resolution further away from this rotation center. Possible applications include region of interest tomography, especially systems where a short total scanning time and a relatively slow detector limit the number of projections that can be acquired.

Continuous tomosynthesis can be of particular interest in systems where the read out speed of the flat panel detector is the limiting factor on the acquisition speed. In this case, the total acquisition time can only be reduced by reducing the number of projections. If a high resolution is primarily needed in a specific region of interest of the image, ARTIC provides a trade off between acquisition speed and region of interest size.

Acknowledgments

The authors would like to thank Pierre Lhuissier for providing the continuous projections dataset from the ESRF Long Term Project LTP ma1876: 'Use of coherency and large field of view for fast in situ multi-resolution imaging'. The authors also thank Frédéric Noo for his valuable comments. This work was supported by Agfa Healthcare and the Agency for Innovation by Science and Technology in Flanders (IWT). Networking support was provided by the EXTREMA COST Action MP1207. Reconstructions were computed with the ASTRA toolbox [? ?].

3.7 Linearization of forward projector

The linearization of the forward projector in Eq.(3.7) is based on the assumption that each ray sum $b_{i,s} \equiv \sum_j a_{i,j,s} x_j$ only differs slightly from the average ray sum $b_{i,avg} \equiv \frac{1}{S} \sum_{s=1}^S b_{i,s}$.

3.7. LINEARIZATION OF FORWARD PROJECTOR

The following example of a cross section of a human thorax illustrates this assumption. We assume a body width of approximately 40cm and use the attenuation coefficients of Table 3.3. We further assume the X-ray beam is produced by a 100kV source, which corresponds to an approximate beam energy of 50keV[?].

A beam s passing mostly through soft tissue or lung tissue would result in $b_{i,s} \approx \sum_j a_{i,j}^c x_j = 40\text{cm} \times 0.2270/\text{cm} = 9.08$. A beam s encountering a lung nodule of 1cm with an approximate attenuation value of cortical bone results in $b_{i,s} = 9.2772$. If half of the beams contributing to b_i encountered the nodule, this leads to $b_{i,avg} = 9.1786$. The error made by the linearization is $9.1786 - (-\log((\exp(-9.08) + \exp(-9.2772))/2)) = 0.0049$, or a relative error of 0.0534% on $b_{i,avg}$.

As a counterexample, assume some of the beams s hit a long structure which is aligned with the beam direction, e.g. a metallic implant of 20cm length. In this case, $b_{i,s} = 20\text{cm} \times 1.213/\text{cm} + 20\text{cm} \times 0.2270/\text{cm} = 28.8$, which differs substantially from beams passing only through soft tissue. In this case, the linearization of Eq. (3.7) would be invalid.

material	$\mu(1/\text{cm})$
lung tissue	0.2270
cortical bone	0.4242
soft tissue	0.2264
titanium	1.213

Table 3.3: Average attenuation factors of common tissues in the human body and titanium, as reported by Hubbell et al[?].

4

Mobile chest tomosynthesis in the ICU

Contents

4.1	Introduction	58
4.2	Material and methods	60
4.3	Results	64
4.4	Discussion	65
	References	73

CHAPTER 4. MOBILE CHEST TOMOSYNTHESIS IN THE ICU

Portable Chest X-Rays (CXRs) are an important and frequently used tool in the Intensive Care Unit (ICU). Unfortunately, the diagnostic value of the bedside chest exam is often low, due to technical limitations and suboptimal patient positioning. Additionally, abnormalities in the chest may be hidden on the projection image by overlapping anatomy and devices such as endotracheal tubes, lines and catheters (Fig. 4.1).

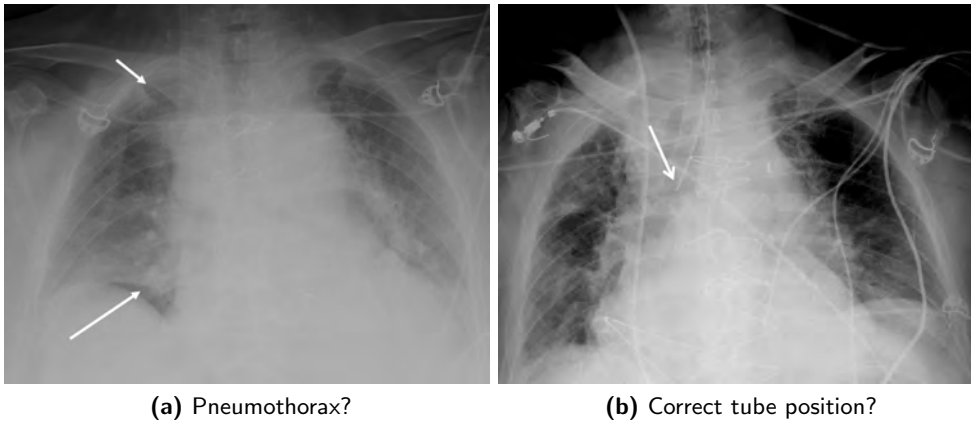


Figure 4.1: Examples of bedside chest X-rays (CXR) that are challenging to interpret due to overlap of anatomy and devices. (a) Pneumothorax is difficult to assess due to the overlap of non-collapsed lung lobes in the supine patient. (b) End of the ventilation tube should be placed right before the bifurcation of the two main bronchi, which are hard to inspect due to overlap of stitches, lines and anatomy.

The purpose of this chapter is to investigate whether the development of portable chest tomosynthesis (TS) can improve the diagnostic value of bedside CXRs. Modifications on chest TS are presented for a portable modality, and potential applications in the ICU are illustrated with a simulation study.

Preliminary results indicate that portable chest TS is technically feasible and can potentially lead to better patient care, due to the improved depth resolution.

4.1 Introduction

Chest X-Rays (CXR) play an important role in patient management in the Intensive Care Unit (ICU) [?]. CXRs assist physicians in the diagnosis and follow up of a variety of cardiopulmonary disorders. They provide value in identification of findings necessitating emergency medical care, such as pneumothorax, (ventilator

4.1. INTRODUCTION

associated) pneumonia or atelectasis, and assessment of volume status [?]. Additionally, CXRs are used to evaluate a broad range of intrathoracic medical devices, ensuring proper positioning and surveying for complications [? ? ?].

Although the justification for daily follow up of patients with CXRs in the ICU is under constant scrutiny [? ?], the American College of Radiologists considers the use of CXRs in the ICU highly appropriate - especially upon admission and after placing invasive devices such as endotracheal tubes, endovascular catheters and drains, or when the condition of the patient worsens [?].

Bedside CXR is the imaging modality of choice for evaluation of the chest in ICU-patients, since these patients need to be monitored closely and are often less mobile due to mechanical ventilation or other medical devices such as drains and tubes. A schematic representation of mobile chest X-ray imaging is shown in Fig. 4.2a. Note how the presence of medical equipment and a ceiling suspension limit the maneuvering space of the mobile X-ray unit.

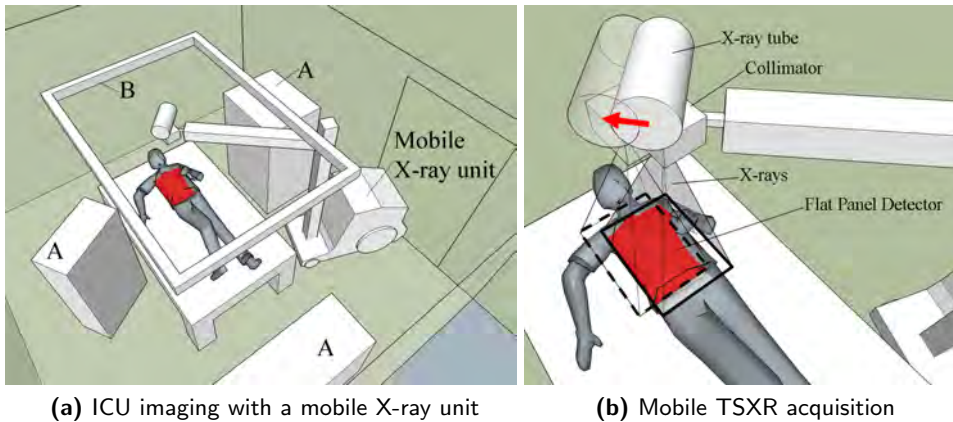


Figure 4.2: (a) example ICU isolation room, showing medical devices such as monitors (A) and a ceiling suspension (B), limiting the maneuvering space of the mobile X-ray unit. (b) shows an example motion of the mobile X-ray tube, to obtain TSXR images from different angles for tomosynthesis.

Despite the advantage of high accessibility, the diagnostic value of portable CXRs in the ICU is significantly lower when compared to a CXR obtained with a dedicated wall mounted flat panel device. First of all, compared to a standard posterior-anterior (PA) and lateral (LAT) exam, the portable anterior-posterior (AP) exam of a bedridden patient in supine position shows an apparently enlarged width of the heart, which may obscure retrocardiac structures, especially

in poor inspiration. Also, the detection and assessment of certain abnormalities (e.g. pneumothorax) is known to be more difficult on portable CXRs obtained in a reclining patient, when compared to CXRs acquired from an upright patient [?]. Additionally, the clinical condition of the patient often hinders optimal patient positioning, causing asymmetric images and superposition of anatomical structures (e.g. of the clavicles over the lung apices). Frequently, superposition of devices, tubes and catheters as well as patient related factors (obesity, hypoventilation, motion) further reduces the quality of the portable CXR in the ICU. Finally, the portable CXR is subject to technical limitations: images are acquired at 90kV instead of 120kV, which results in a less translucent appearance of the ribs. Image contrast in portable CXRs is also reduced due to the absence of an anti-scatter grid in the acquisition and the reduced source image distance of 1.2m causes higher geometrical distortions [?].

Chest tomosynthesis (TS) has potential to improve the diagnostic value and in particular depth resolution of bedside CXR. Chest TS is a technique which is already on the market on a wall mounted flat panel or X-ray table [?]. First, a small number of low dose tomosynthesis X-ray images (TSXRs) (usually between 35 and 60) are acquired with a motorized X-ray source, which moves relative to a stationary detector, as illustrated in Fig. 4.3a. Next, advanced reconstruction algorithms are used to compute coronal section images of the patient. These section images have a higher in-plane resolution than CT, but a lower depth resolution of the slices, due to the limited sweep angle of the X-ray tube (typically 30°) [?]. Chest TS has been reported to improve the detection of lung nodules compared to CXR, thanks to its ability to separate overlapping anatomical structures into subsequent slices [? ?]. Therefore, we are convinced that portable chest TS could also substantially increase the diagnostic value of the portable CXR in the ICU, even though currently, no portable version of a chest TS modality is on the market.

The purpose of this chapter is to investigate if portable chest TS can improve the diagnostic value of portable CXR in the ICU.

4.2 Material and methods

Because there is, to date, no portable TS device on the market, portable chest TS exams were simulated retrospectively. To this end, computed tomography (CT) scans of selected ICU patients were used to simulate TSXRs. Note that the total tube travel distance for the mobile TSXR simulations was substantially reduced compared to a standard tomosynthesis exam, to avoid collisions with equipment in the ICU room. The simulated TSXRs were then used to compute a simulated TS exam. The simulated TS exams were interpreted and compared with the CXRs.

Two ICU patients were retrospectively selected from the hospital Picture Archiv-

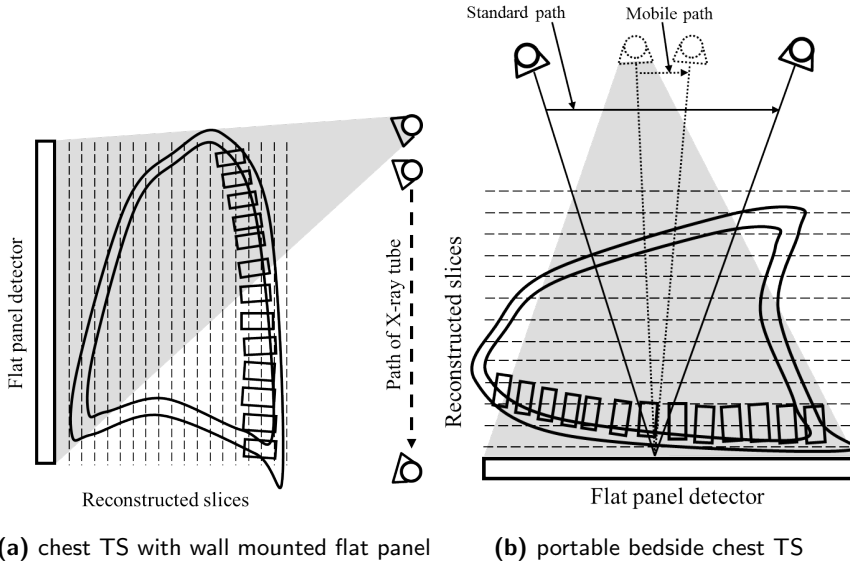


Figure 4.3: (a) Schematic drawing of chest tomosynthesis (TS). Several low dose postero-anterior tomosynthesis X-ray images (TSXRs) are acquired with a wall mounted flat panel. A motorized X-ray tube moves on a (typically straight) path with respect to a stationary flat panel detector. Next, coronal slices are computed using a reconstruction algorithm, indicated by the dashed lines. (b) Portable chest TS in antero-posterior direction in a bedridden supine patient. Note the reduced X-ray tube path length for portable acquisition geometries.

ing and Communication System (PACS) who underwent both a CXR and a chest CT scan within a time frame of one hour. The need for informed consent was waived by the Ethical Committee. From the anonymized CT data, which consisted of voxels of $0.5 \times 0.5 \times 0.84\text{mm}$ size, 15 TSXRs were simulated using the ASTRA tomography toolbox [?], which contains algorithms for simulating X-ray radiographs. The source image distance was set to 120cm. The total tube travel distance was set to 14cm. This corresponds to an angular range of 6° , which is substantially less than the typical 35° angular range in chest TS with a dedicated wall mounted flat panel detector as illustrated in Fig. 4.3b. Simulated TSXR images were 831×1012 pixels of 0.42mm size. Next, from the simulated TSXRs, 55 coronal section images of 5mm depth were computed by TS reconstruction using 50 iterations of the simultaneous iterative reconstruction technique (SIRT) [?]. Finally, the reconstructed TS section images were compared to the original CXR and interpreted for ICU-related abnormalities.

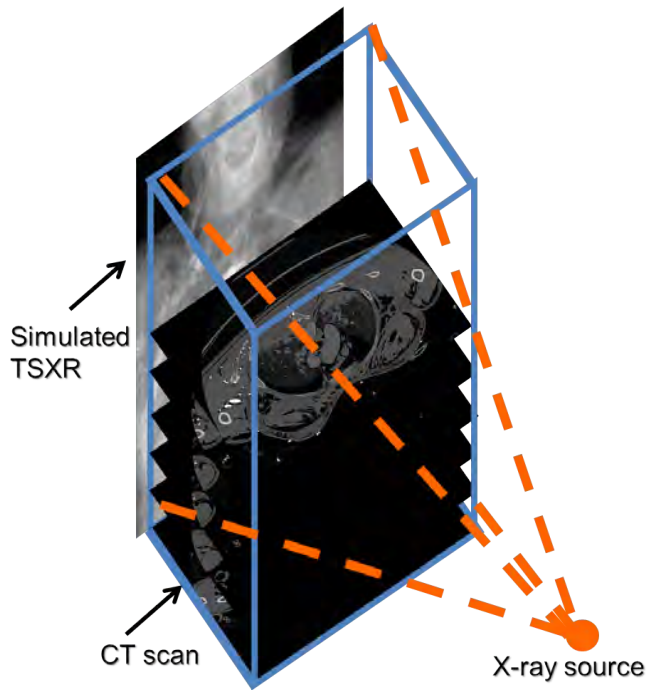


Figure 4.4: A CT exam was used for the simulation of TSXRs. CT slices were stacked together into a three dimensional volume, after which a simulated TSXR was computed using the ASTRA toolbox.

4.2. MATERIAL AND METHODS

To validate the TS simulation approach based on CT scans, a simulated TS exam was compared with an experimentally acquired TS exam of an anthropomorphic chest phantom (Humanoid Systems, Carson, USA). For the experimental TS exam, 15 chest TSXRs were acquired manually —(i.e. without motorized tube motion) with a mobile X-ray unit (Agfa Healthcare DXD-100), from the same angles and source image distance as in the ICU simulations above (Fig. 4.5). All TSXRs were obtained at 90kV and 0.1mAs, which was the lowest possible tube current of the mobile unit. Subsequently, 55 coronal section images of 5mm depth were computed by TS using 30 iterations of SIRT. For the simulated TS exam, 15 TSXRs were simulated from a CT scan of the anthropomorphic phantom and a simulated TS reconstruction was computed. Reconstructions from the experimental TS exam and CT based simulated TS exam were compared visually by an experienced thoracic radiologist.

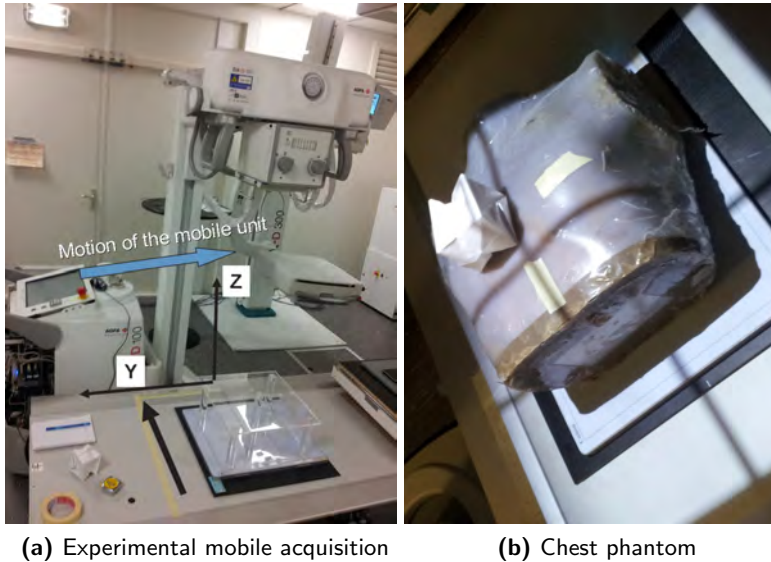


Figure 4.5: Experimental acquisition of mobile chest TSXRs. (a) The mobile X-ray unit was advanced manually. A tape (black arrow) was attached to the table, on which centimeters were marked. The collimator light of the X-ray tube was used to manually progress the unit based on these markings. (a) Image of the chest phantom, used in this experimental setup.

4.3 Results

Patient 1

The patient was 26-year old woman, who was admitted to the ICU after a cardiac arrest. Shortly after admission, she developed severe subcutaneous emphysema.

The bedside CXR (Fig. 4.6a) confirms subcutaneous emphysema in the neck, axillae and lateral chest walls. The symmetric dense areas which overly the mid-section of both lung fields are caused by bilateral breast prosthesis. There is no deep sulcus sign, and no clear delineation of a pneumothorax. The left diaphragm is clearly delineated due to a large amount of air in the stomach. The heart contour is relatively sharp, but symmetric on both sides.

A CT-examination was performed 30 minutes later, which was used to simulate TSXR acquisitions (Fig. 4.6b) and compute a simulated TS reconstruction. A slice of the simulated TS reconstruction near the back of the patient (Fig. 4.6c) shows symmetric findings with normal parenchyma on both sides, without areas of consolidation or hyperlucency.

The more anterior simulated TS slice (Fig. 4.6d) shows two triangular areas with absence of lung markings; these findings are consistent with a bilateral pneumothorax. Note that the triangular areas have a similar translucency as compared to the large amount of air in the stomach. A coronal reformatted CT image (Fig. 4.7a) at the same level of Fig. 4.6d, confirms a bilateral pneumothorax and extensive subcutaneous emphysema. The slice locations of the TS and CT slices are shown in Fig. 4.7b.

Patient 2

The second selected patient was a 49-year old man who was admitted to the ICU after a neurosurgical intervention with removal of a 4th ventricular ependymoma. Five days after surgery he developed respiratory insufficiency.

The bedside chest radiograph (CXR) (Fig. 4.8a) shows subcutaneous emphysema in the neck and pulmonary consolidations bilaterally in the basal parts of both lungs.

A CT-examination was performed 1 hour later, because of the discrepancy between respiratory function and findings on CXR, to rule out pulmonary embolism. Simulated TSXRs were computed from this CT exam (Fig. 4.8b).

A slice of the TS reconstruction from the simulated TSXRs at the level of the heart (Fig. 4.8c) shows linear areas of hyperlucency around the heart and in the paravertebral region (black arrow). Also note an area of relative hyperlucency in the left lung with a clear delineation of the adjacent consolidation (white arrows). These findings are consistent with pneumomediastinum. A slice of the

simulated TS reconstruction more posteriorly than TS reconstruction A, shows a large retrocardiac consolidation with air bronchogram (Fig. 4.8d).

A coronal reformatted CT image confirms the pneumomediastinum (Fig. 4.9a) and a large consolidation (Fig. 4.9b) with air bronchogram, consistent with subtotal atelectasis of the left lower lobe. Due to the retrocardiac location, the consolidation is not visible on the CXR. Moreover, the extent of the pneumomediastinum is better appreciated on the TS reconstructions, compared to the bedside radiograph.

Experimental vs simulated exam

The resulting TS reconstruction from the experimentally acquired images of the anthropomorphic phantom are displayed in Fig. 4.10, together with the simulated TS reconstructions from a CT scan. Despite differences in visual appearance and small discrepancies between slice location, both experimental and simulated TS show similar structures and level of depth resolution. This strengthens our belief that the conducted experiments are at least indicative of the expected performance of mobile chest TS.

4.4 Discussion

Chest imaging is under active investigation as a potentially useful application area of TS. The main focus of research on the use of chest TS is on improving the detection of lung nodules as compared to conventional CXR [? ? ? ? ?] and on visualizing other findings related to various pulmonary diseases [? ? ? ? ?]. Additionally, chest TS has the potential to optimize the use of CT resources and reduce the effective dose to the patient population [? ?].

To our knowledge, no portable chest TS application is on the market yet. Whereas the clinical use of chest TS with a dedicated wall mounted flat panel detector can be evaluated against CT, MRI and other modalities, far less alternatives exist for the mobile examination of bedridden patients. Compared to portable chest TS, the cost of performing ultrasound as a daily follow up is relatively high since this exam takes longer to perform and requires a high level of expertise. Mobile CT scanners exist, but are not widespread and they are mainly limited to dedicated applications such as imaging of the head [? ? ?].

Portable chest TS could be implemented on a mobile CXR device, which is already widely accepted as a mobile examination device. Portable TS might also hold potential to improve bedside exams in the emergency room, sterile rooms in hematology wards or transplantation units, burn units, surgical departments, etc. The radiation dose for a chest TS exam on a dedicated wall mounted flat

panel is around 0.12mSv for a typical acquisition of 60 images [? ?]. In our experiment however, only 15 TSXRs were taken at 90kV and 0.1mAs. To compute the effective dose of the portable chest TS exam as described in this study, the PCXMC[?] simulation software was used. This resulted in a total effective dose of 0.029mSv, which corresponds to approximately 1.5 times the dose of a portable CXR, obtained at 90kV and 1mAs.

Portable chest TS, as described in this study, can be implemented with a mobile X-ray unit and a portable detector panel. To minimize the risk of collisions with other equipment in the ICU, the tube travel distance, and thus the angular range, was significantly reduced as compared to TS exams in a dedicated X-ray room. Söderman et al [?] showed that decreasing the angular range has a positive effect on the reproduction of the trachea and paratracheal tissue, vessels and aorta. However, a smaller angular range resulted in decreased image quality related to following vessels through the volume. Image quality for findings more specifically related to critically ill patients, such as pneumothorax/pneumomediastinum and the capability of separating overlapping devices into different slices, were not discussed. Also, the aforementioned study investigated different configuration parameters for chest TS with an effective dose comparable to a standard TS exam. Our simulations show that portable chest TS in the ICU with a small angular scanning range (only 6°) and a low radiation dose of only 0.029mSv, is feasible.

Our results, as illustrated in Figs.4.6 and 4.8, clearly show advantages of mobile chest TS over CXR. However, our study was based on simulations and there are obviously some differences with real acquisitions. Obviously, our simulation provides better image quality than real TS acquisitions due to the absence of patient motion. In a real-life situation, the acquisition of 15 TSXRs will take a few seconds, during which time breathing or other types of patient motion might occur. Many ICU patients might not be able to hold their breath, although for intubated patients, a short interruption in mechanical ventilation could be considered in some cases. Patient motion during the acquisition of the TSXRs is a well-known cause of degradation of TS image quality. Thus, reconstruction and motion correction methods will need to be incorporated and improved in a portable chest TS device [? ? ?].

Secondly, the quality of the reconstruction heavily relies on the accuracy of the position of the X-ray source and detector at the time the TSXRs are taken. In a real-life situation, errors in the relative position of tube and detector are to be expected, especially for bedside examinations where X-ray source and detector are not mechanically connected. Misalignment errors in the positioning will result in reconstruction artifacts, and alignment algorithms as were described in Chapter 5 will have to be applied to correct this misalignment.

On the other hand, the simulation in our experiment also has a disadvantage over real TS acquisitions, as it was derived from a CT scan with a relatively high voxel size of 0.5mm, leading to simulated TSXRs with a pixel size of 0.42mm. A real TSXR, acquired with a flat panel detector, typically has a pixel size of 0.150mm or lower, which will have a substantial positive impact on the in plane resolution of the reconstructions.

In conclusion, we have shown that portable chest TS holds potential to improve the diagnostic accuracy of bedside radiographic imaging in the ICU. Possible benefits include: improved localization of parenchymal consolidations (anterior vs posterior), detection of pneumothorax/pneumomediastinum in supine patients, verification of the correct position of drains and lines, differentiation between pleural effusions vs. consolidations, and other applications. It is technically feasible to perform mobile chest TS with a (modified) mobile X-ray unit, which is already widely accepted as a mobile examination tool.

Acknowledgments

The authors would like to thank prof. dr. Paul M. Parizel and dr. Annemie Snoeckx of the University Hospital of Antwerp, for their kind cooperation on the collection of the relevant ICU patient cases, and their meaningful comments and insights on the topics discussed in this chapter.

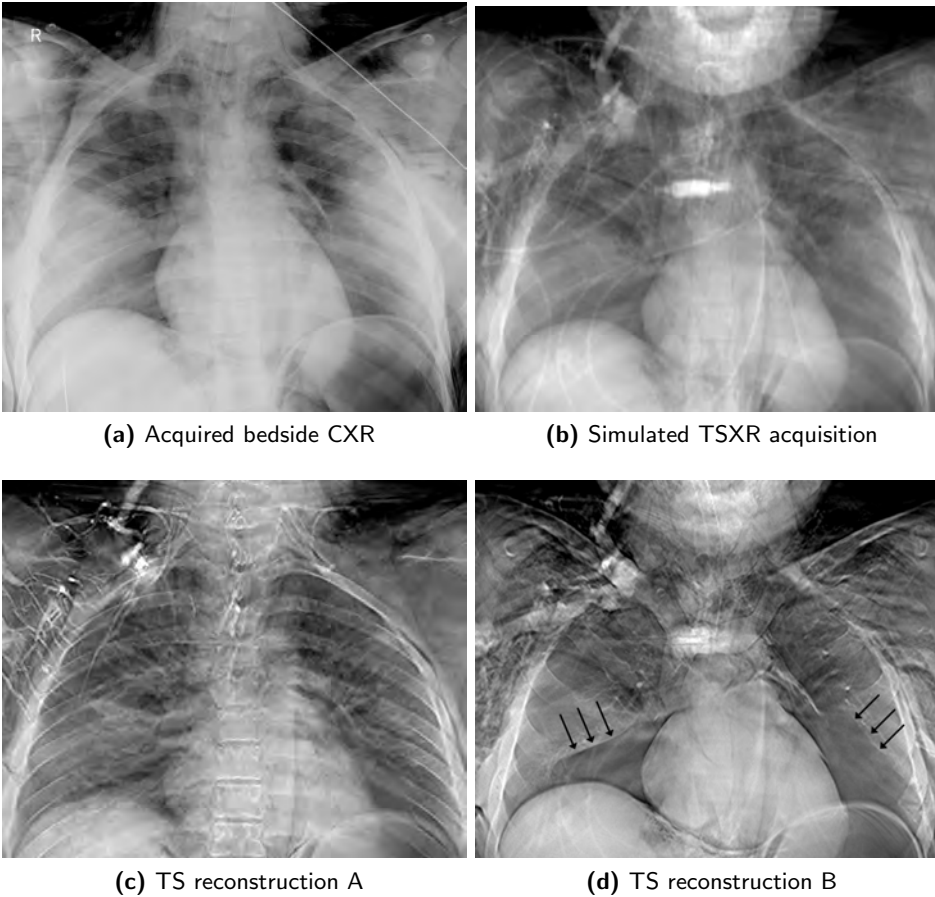


Figure 4.6: 26-year old woman, who was admitted to the ICU after a cardiac arrest. Shortly after admission, she developed severe subcutaneous emphysema. Whereas the bedside CXR (a) shows no clear delineation of a pneumothorax, the more anterior simulated TS slice (d) shows triangular areas with absence of lung parenchyma (black arrows), which are consistent with bilateral pneumothorax.

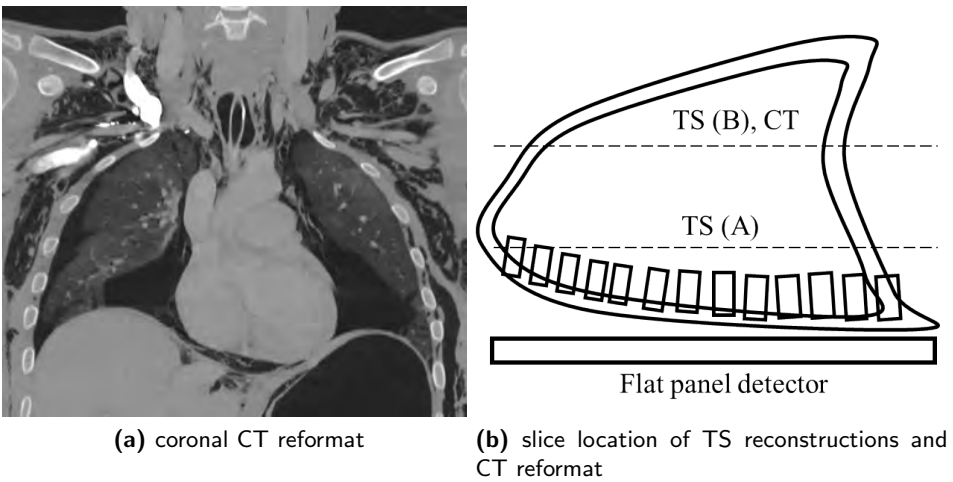


Figure 4.7: (a) Coronal reformat of the CT scan of the first selected patient, confirming the bilateral pneumothorax. (b) slice locations of the CT reformat and the two selected TS reconstructions from Fig. 4.6.

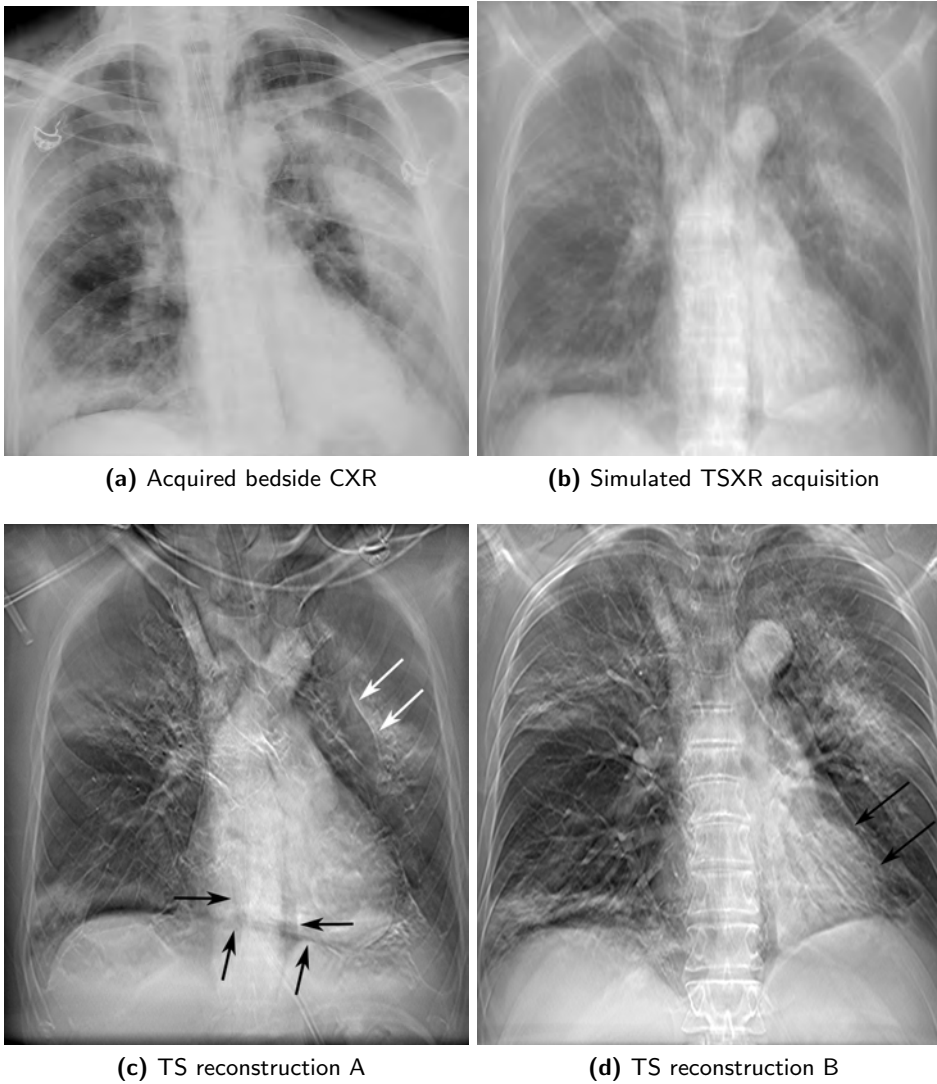


Figure 4.8: 49-y-old man who was admitted to the ICU after a neurosurgical intervention with removal of a 4th ventricular ependymoma. Five days after surgery he developed respiratory insufficiency. A CT exam was performed to rule out pulmonary embolism because of the discrepancy between respiratory function and findings on the CXR. Due to the retrocardiac location, a consolidation detected on the TS slices (c),(d) was not visible on the CXR (a). Moreover, the extent of the pneumomediastinum could be better appreciated on the TS reconstructions.

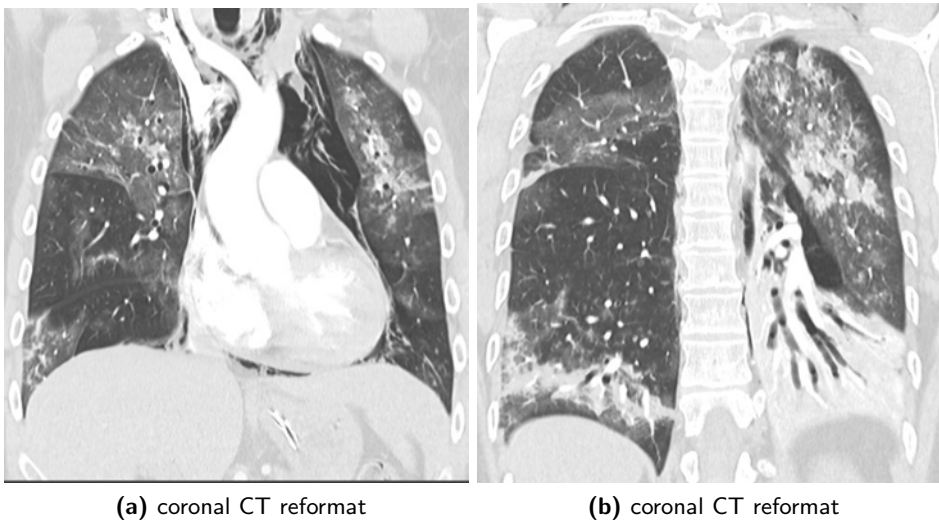


Figure 4.9: Coronal reformatted CT images of the second patient, confirming the pneumomediastinum (a) and a large consolidation (b) with air bronchogram, consistent with subtotal atelectasis of the left lower lobe.

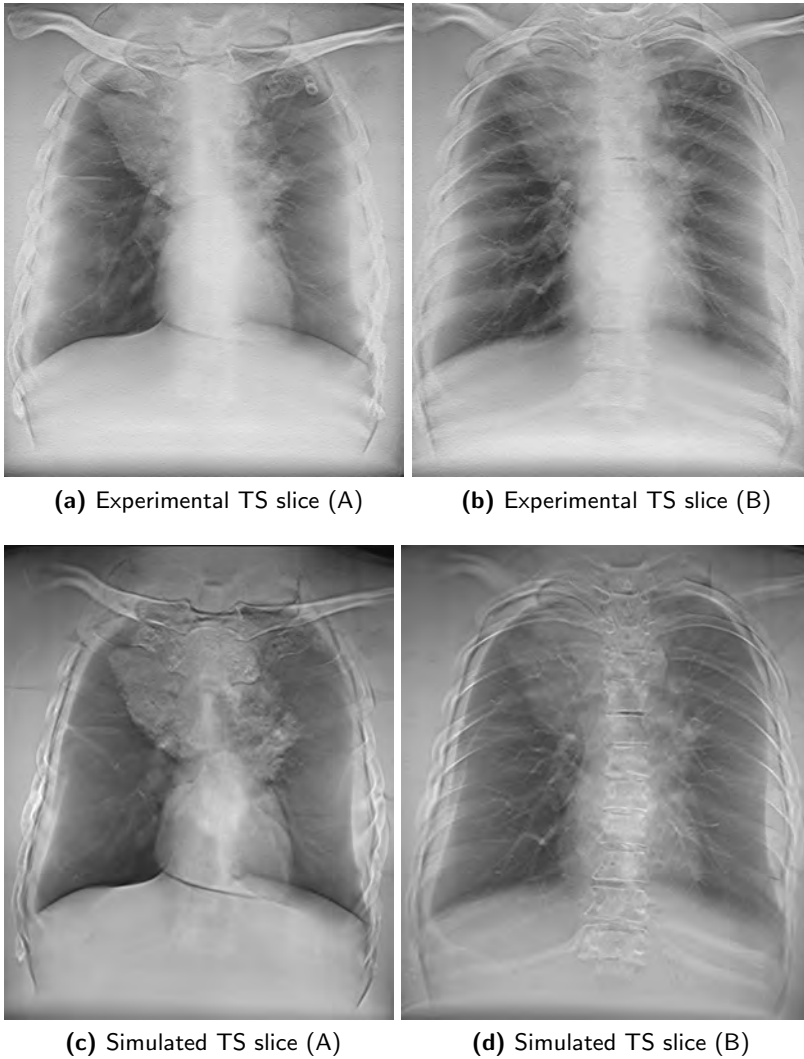


Figure 4.10: Comparison between experimental and simulated tomosynthesis reconstructions of a phantom. (a), (b) show a reconstruction from experimentally acquired TSXRs. (c), (d) show a reconstruction from simulated TSXRs, based on a CT scan of the phantom. Note the similar depth resolution between experimental and simulated TS exams. Although the simulated TS slices show a higher visual contrast, all structures present in the simulated images can also be appreciated in the experimentally acquired TS slices.

5

Geometry parameter estimation

Contents

5.1	Introduction	74
5.2	Geometric inaccuracies	75
5.3	Method	82
5.3.1	Plane-based raw data redundancy criterion	82
5.3.2	Truncation weighting	84
5.3.3	Robust cost function for linear tube motion	85
5.4	Experiments	86
5.4.1	XCAT simulations	86
5.4.2	Experimental data	87
5.5	Discussion	89
5.6	Conclusion	92
	References	92

In this chapter, a method is described to accurately estimate the acquisition geometry of a chest tomosynthesis exam, which is crucial in order to reconstruct high quality TS images. Inaccuracies in the assumed acquisition geometry lead to errors in the reconstruction such as striping and blurring and a general loss of resolution. Moreover, the method is critical for the implementation of mobile tomosynthesis, as the geometry for a portable flat panel cannot be calibrated up front with a calibration phantom.

Section 5.1 provides an introduction on geometric alignment in chest tomosynthesis. In Section 5.2, the effect of inaccuracies in the geometry of a chest tomosynthesis exam is first studied for the different geometric parameters. Subsequently, in Section 5.3, a method for automatic geometric alignment is described, based on dataset consistency conditions. The method is evaluated with experiments on simulations and experimental acquisitions in Section 5.4. Discussion and conclusion can be found in Section 5.5 and Section 5.6, respectively.

5.1 Introduction

In chest tomosynthesis systems, a stationary flat panel detector is placed behind a patient and a motorized X-ray source is used to create a set of projection images from a limited angular range. Subsequently, section images are reconstructed in planes parallel to the detector using a reconstruction algorithm[?]. In order to obtain high quality reconstructions, accurate knowledge of the positions of X-ray source and detector is required. Inaccuracies in the assumed geometry are a cause of reconstruction artifacts such as striping and blurring.

In tomosynthesis systems with a reproducible mechanical motion, the geometry can be calibrated up front using a calibration phantom[?]. Examples are systems where a flat panel detector is mounted in a fixed wall stand and an X-ray tube is mounted on a ceiling suspended motorized column, or an integrated table system where the X-ray source and detector are both mechanically connected to the table on which the patient is positioned. However, small deviations from the calibrated geometry might still occur due to unforeseen motion of the different components in time, for example if a portable detector is placed in a tray inside the X-ray table or wall stand from which it can be removed.

In a future mobile system for bedside tomosynthesis, a portable flat panel detector could be placed behind a bedridden patient and X-ray exposures could be performed with a mobile X-ray unit. In this case, the relative locations of X-ray source and panel will vary with each exam and can therefore not be calibrated upfront with a calibration phantom. If the geometry is measured online during the acquisition using sensors or other devices, errors are to be expected in the assumed geometry as well.

Both forementioned examples illustrate the need for a calibration algorithm that can be applied online, using the information present in the acquired projection images rather than upfront acquisitions of a phantom image or secondary measurements with peripheral sensors. For online calibration, radiopaque markers can be used to derive the acquisition geometry [?]. The disadvantage of using fiducial markers is that they are present in the projection images and thus also in the reconstructed image. Moreover, fully automatic robust detection of the markers can be challenging, especially in complex images such as X-ray projections of the chest. Alternatively, a calibration object can be attached to the X-ray source housing and be detected in the projection images for geometric calibration [?].

Another type of online calibration relies on data consistency conditions, which describe redundancies between projection images based on the information present in the projection images themselves, without the need for markers or calibration objects in the projections. From these conditions, a cost function can be formulated that, after minimization, leads to the optimal geometric parameters such as detector orientation and position. Such a technique was developed for estimating and correcting the geometric parameters in a cone beam computed tomography setup for a straight-line trajectory [?], and recently for a free trajectory based on epipolar consistency conditions (ECC) [?]. However, the existing methods are not robust enough to deal with truncation, which is substantially present in chest tomosynthesis acquisitions.

To deal with truncation, a heuristic weighting function was introduced in recent work to weigh the gray values in the projection images, depending on the fraction of the ray passing the part of the object that is visible on all projections and an estimation of the maximal object thickness [?]. In this chapter, an improved automatic online geometric calibration algorithm is proposed for chest tomosynthesis, with a truncation weighting function which is independent from the estimated object thickness and which applies prior knowledge about the X-ray source motion to increase the robustness of the cost function.

5.2 Geometric inaccuracies

In this section, the effect of different types of errors in the acquisition geometry on the reconstructed image quality is studied in more detail and the practical effect on the clinical image quality of tomosynthesis is discussed. It will be shown that the relative rotation of the detector with respect to the path of the X-ray source causes the most disturbing artifacts.

In algebraic reconstruction algorithms, the unknown attenuation coefficients

CHAPTER 5. GEOMETRY PARAMETER ESTIMATION

$\mathbf{x} \in \mathbb{R}^n$ of an object are estimated from measured projections \mathbf{p} :

$$\mathbf{W}\mathbf{x} = \mathbf{p} \quad (5.1)$$

The projection is modeled by a forward projection matrix \mathbf{W} , which depends on the relative positions of the object, X-ray source and detector during the projections. If the acquisition geometry is not known exactly, \mathbf{W} does not model the projection correctly and it can be intuitively understood that this will have an effect on the correctness of the estimation of \mathbf{x} .

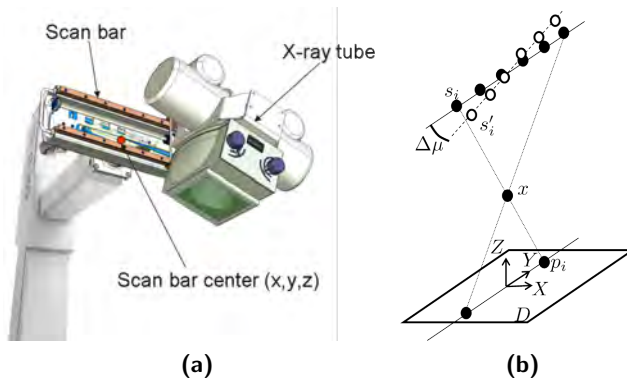


Figure 5.1: (a) Illustration of a modality with a moving X-ray source. During acquisition of the images, the X-ray tube moves along a scanbar. The flat panel detector is placed behind the patient and does not move. The location of the scanbar is measured relative to the detector panel. (b) Illustration of geometric inaccuracy. X-ray source positions s_i are placed on a line and generate projections p_i of a point x on detector D . The white circles represent incorrectly measured X-ray source positions s'_i . In this figure, the measured angle between the panel heading and X-ray motion path is $\mu + \Delta\mu$, with $\Delta\mu$ the measurement error.

In this section, the effects of inaccuracies in the assumed acquisition geometry are studied for the specific case of (chest) tomosynthesis, in which an X-ray source moves on a straight line with a fixed detector. The setup with a linearly moving X-ray source can be found in common chest tomosynthesis setups, but also in mobile tomosynthesis as illustrated in Fig. 5.1a. The tube is mechanically moved along a straight line on the scanbar, which is attached to a mobile X-ray unit. Assuming that the scanbar itself remains stationary, the entire acquisition geometry can be defined by the location of the center point of the bar and its orientation, both relative to the detector, and the distance between consecutive X-ray tube locations.

To study the effects of inaccuracies in the geometry, a theoretical tomosynthesis X-ray system is simulated with an infinitely small focal spot size and a detector

with infinitely small pixels. All other physical parameters that affect resolution such as a finite focal spot size, detector pixel blur, scatter, discretization, ... are ignored in the simulation.

The X-ray source moves along a straight line, and projects a virtual point \mathbf{x} from positions \mathbf{s}_i onto positions \mathbf{p}_i on a fixed detector, as illustrated by the black dotted lines in Fig. 5.1b. The detector has size $430 \times 430\text{mm}$ and the X-ray tube moves at a source-image distance (SID) of 1000mm . The object \mathbf{x} is placed 300mm above the detector center.

The reconstruction algorithm (e.g. SIRT [?]) will subsequently perform a backprojection of these measured points \mathbf{p}_i , towards \mathbf{s}_i . The strongest signal will be present in the reconstructed image at the point where these backprojection rays intersect, and hence determine the position of the reconstructed point \mathbf{x} .

However, if the X-ray source positions are measured incorrectly, the assumed positions \mathbf{s}'_i are affected by an error on the center position of the line and the angle with respect to the panel. The projected points \mathbf{p}_i will therefore be backprojected along incorrectly defined lines by the reconstruction algorithm.

Two effects can be observed. First, the location of the reconstructed point \mathbf{x}' can have moved from the correct location \mathbf{x} , as illustrated in Fig. 5.2 which shows an X-ray tube path that was slightly rotated and translated in the YZ -plane. The amount of translation of \mathbf{x}' is dependent on the distance of \mathbf{x} to the detector D and the translation of the X-ray source path. Secondly, in some cases the rays will not intersect in a single point anymore, which can be seen in the zoomed image of the region around \mathbf{x}' in Fig. 5.2b. If backprojected rays do not intersect in a single point, the sharpness of the reconstructed image will be affected.

In this section, the main focus will be on sharpness or resolution. Displacement and or scaling of objects in the reconstructed image is of secondary concern, as tomosynthesis images are not used for measuring exact dimensions of objects. However, a loss of sharpness affects image quality and needs thus to be measured and corrected.

Resolution measurements

The theoretical resolution R is defined as the minimal width of the bundle of backprojected rays. Different panel orientations with respect to the X-ray source path were chosen to simulate a patient lying in bed and sitting less or more upright until an angle of 45° . A practical threshold for the resolution is the pixel size. As long as the computed resolution remains smaller than the in-plane pixel size of the reconstruction, it is safe to assume that the loss of resolution will not be visible. In our simulation, we assume the detector has a pixel size of $150\mu\text{m}$.

Note that as tomosynthesis reconstructions are computed in slices parallel to the detector, the in plane sharpness and its representative R is also measured

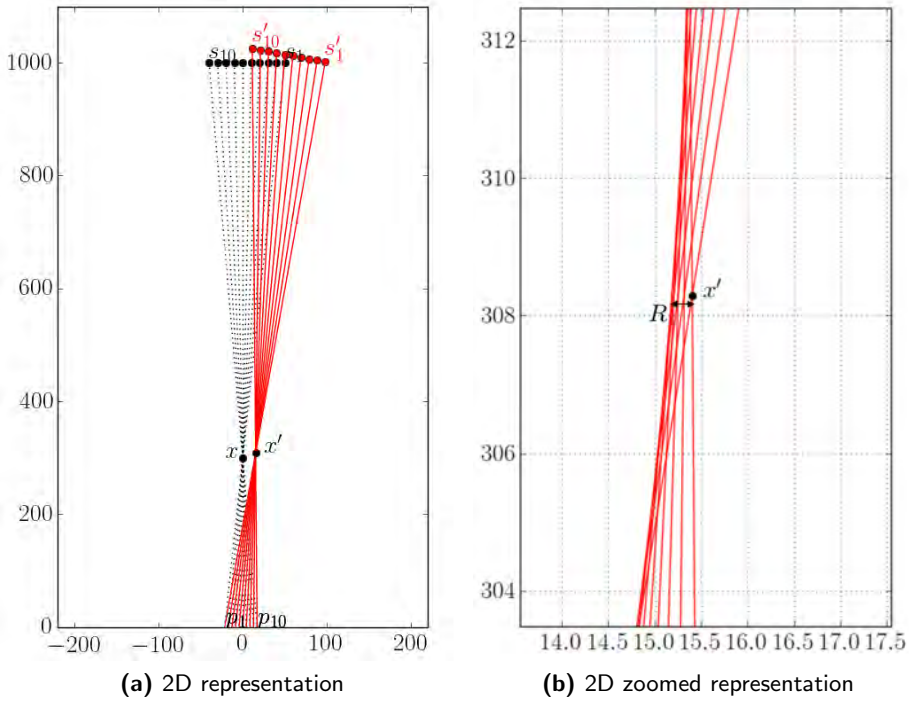


Figure 5.2: Example of geometric inaccuracy. Stationary detector is placed at $y = 0$ and X-ray tube moves at $y = 1000$, units are in mm. (a) shows source positions s_i , object x and projections p_i . The red lines represent backprojections towards inaccurately measured source positions s'_i . The backprojection rays intersect at a displaced point x' (red lines), and seem to intersect at x' . (b) Enlarged view around x' . The backprojection rays in the incorrect acquisition geometry do no longer intersect at a single point, but in a region of width R , which illustrates the decrease of reconstruction resolution.

parallel to the detector.

SID (Source Image Distance)

The effect on the reconstruction resolution of an incorrectly measured SID is displayed in Fig. 5.3. Even for relatively large errors $> 100\text{mm}$, the resolution remains well below the typical pixel size of $150\mu\text{m}$, and will therefore not be noticed. Note how the resolution remains unaffected by errors in the SID if the panel is aligned parallel with the X-ray source path.

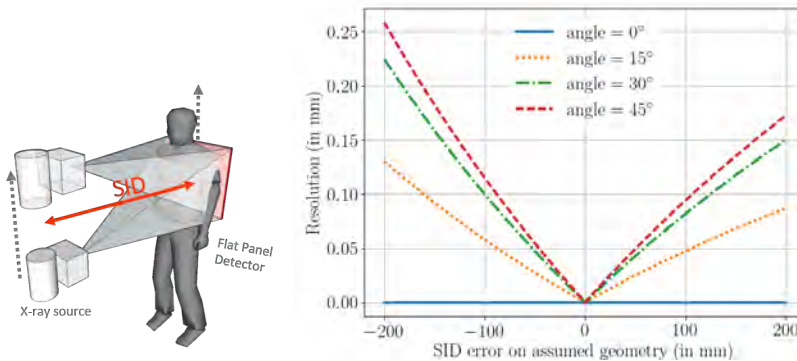


Figure 5.3: Theoretical resolution of reconstructions under vertical errors in the measured X-ray path center position. The vertical distance represents the source image distance (SID). The different angles represent different panel orientations with respect to the X-ray tube path. Note how errors in the SID have no effect if panel and X-ray path are aligned parallel.

Translation

Similarly, an unmeasured horizontal translation of the center of the X-ray path also affects the reconstruction resolution slightly, as shown in Fig. 5.4.

Panel orientation angle

The effect of inaccuracies on the panel orientation in the ZY plane is shown in Fig. 5.5. This panel orientation can be measured with simple electronic devices with an accuracy of less than 1° , which also proves sufficient to keep the resolution beneath the threshold of the pixel size.

CHAPTER 5. GEOMETRY PARAMETER ESTIMATION

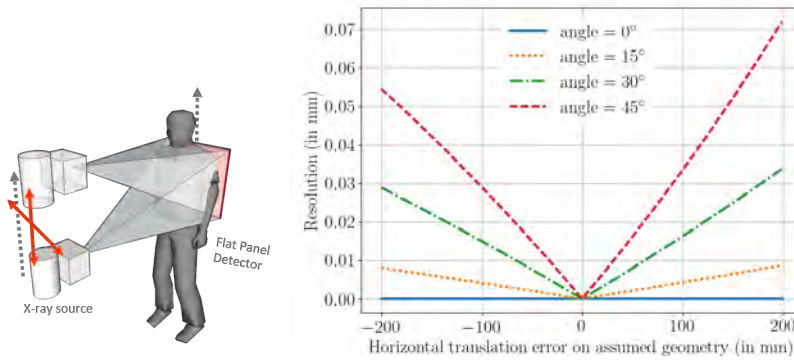


Figure 5.4: Theoretical resolution of reconstructions under horizontal errors in the measured X-ray path center position. The different angles represent different panel orientations with respect to the X-ray tube path. Note how, similar to vertical errors, horizontal errors on the X-ray tube center have no effect if panel and X-ray path are aligned parallel.

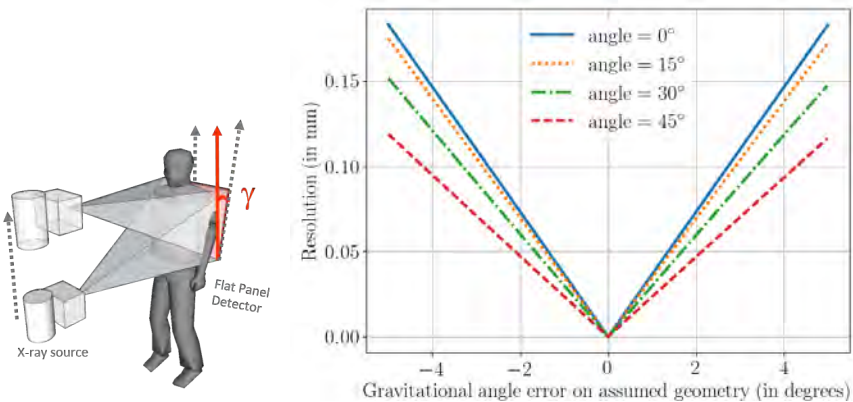


Figure 5.5: Theoretical resolution of reconstructions, performed with errors on the assumed panel orientation γ .

Panel heading angle

The last simulation involves the relative orientation μ of the panel and the X-ray source path. This angle cannot be measured with simple gyroscopic devices, as the rotation occurs in planes with equal gravity (for a bedridden patient). As can be seen in Fig. 5.6, even small inaccuracies in this measured angle μ cannot be neglected and will have an effect on system sharpness. The method described in the next section will therefore focus on correcting this angle μ first. Note that the angle μ itself does not affect the loss of resolution, only the inaccuracy $\Delta\mu$ affects R .

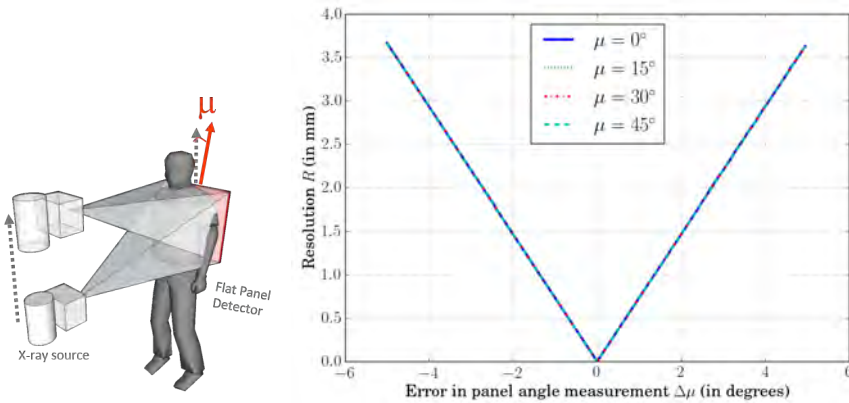


Figure 5.6: Theoretical resolution of reconstructions under errors $\Delta\mu$ in the measured angle μ between the X-ray path and the panel heading (columns). Note how even small errors of $\Delta\mu < 1^\circ$ cause the resolution to exceed the pixel size of $150\mu\text{m}$, and that the effect on the resolution R is not affected by the orientation γ of the panel.

5.3 Method

In this chapter, modifications to the original epipolar consistency criterion (ECC) based estimation of geometrical parameters of Debbeler [?] are presented, specifically designed for chest tomosynthesis. We present a weighting function that does not depend on the patient thickness, and additional modifications to increase robustness against geometrical parameter outliers.

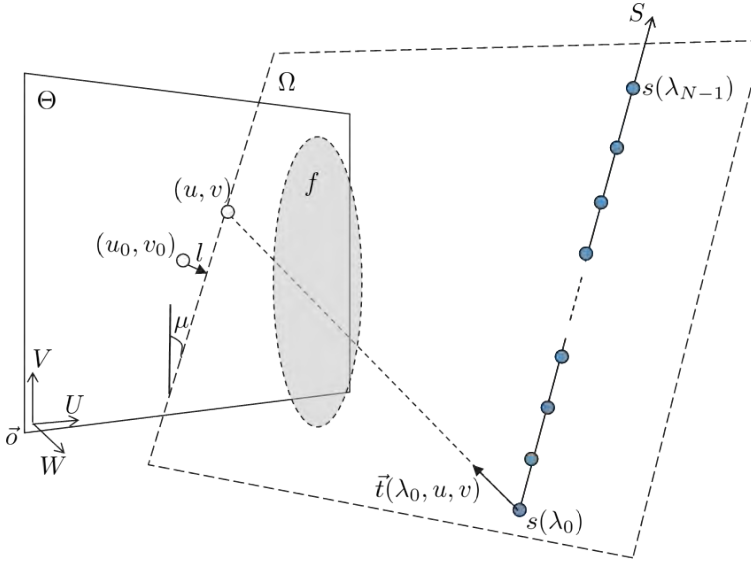


Figure 5.7: Illustration of a chest tomosynthesis acquisition. N X-ray images are acquired on a stationary flat panel detector Θ with an X-ray tube that moves on a straight line S . The angle μ represents the orientation of the detector, relative to the X-ray tube path. Most chest tomosynthesis systems are designed such that $\mu = 0$.

5.3.1 Plane-based raw data redundancy criterion

A schematic representation of chest tomosynthesis is illustrated in Fig. 5.7. Projections are acquired of a patient f with a stationary detector Θ . The N subsequent positions of the X-ray source are indicated as $s(\lambda_i)$. Note that in our setup, the X-ray source moves on a linear path S . In other tomosynthesis setups the source might move on a circular path over a limited angle, which is not considered in this work. The coordinate frame attached to the detector has axes (U, V, W) .

The epipolar consistency criterion describes a redundancy between two projec-

tion images $\mathbf{p}(\lambda_n)$ and $\mathbf{p}(\lambda_{\hat{n}})$, corresponding to the source points $s(\lambda_n)$ and $s(\lambda_{\hat{n}})$ respectively. Multiple planes Ω can be drawn that intersect both source points and the detector. The intersection of Ω and the detector can be parameterized by an angle μ and a distance l from the detector center (u_0, v_0) , as illustrated in Fig. 5.7. For noiseless acquisitions without truncation, the redundancy criterion states that the derivatives of the line integrals along angle μ of the cosine-weighted projection images \mathbf{p} are equal:

$$g_3(\lambda_n, \mu, l) = g_3(\lambda_{\hat{n}}, \mu, l) \quad (5.2)$$

with g_3 defined as:

$$g_3(\lambda_n, \mu, l) = \frac{\partial}{\partial l} g_2(\lambda_n, \mu, l) \quad (5.3)$$

where

$$g_2(\lambda_n, \mu, l) = \int_{-\infty}^{\infty} g_1(\lambda_n, l \cos \mu - t \sin \mu, l \sin \mu + t \cos \mu) dt \quad (5.4)$$

and

$$g_1(\lambda_n, u, v) = \frac{1}{|\mathbf{w} \cdot \mathbf{t}(\lambda_n, u, v)|} p(\lambda_n, u, v) \quad (5.5)$$

with \mathbf{p} the projection data, \mathbf{w} the normal of the detector and $\mathbf{t}(n, u, v)$ the direction of the ray arriving in detector pixel (u, v) of the n^{th} projection. This is illustrated in Fig. 5.8.

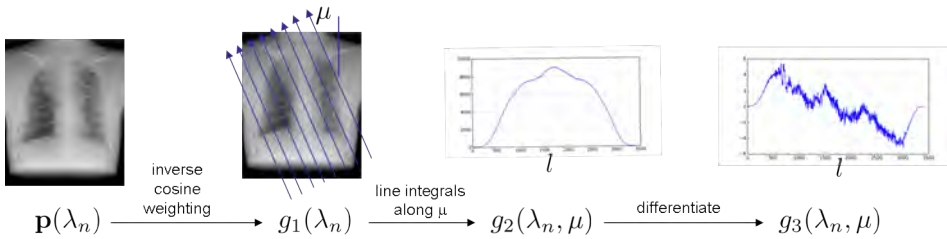


Figure 5.8: Schematic representation of the epipolar consistency criterion. For two projection images $\mathbf{p}(\lambda_n)$ and $\mathbf{p}(\lambda_{\hat{n}})$, $g_3(\lambda_n, \mu, l) = g_3(\lambda_{\hat{n}}, \mu, l)$ with μ the angle of the X-ray path with respect to the detector.

In this work, we will focus on the estimation of the detector orientation μ , relative to the linear motion path of the X-ray tube. Assuming noiseless projections without truncation, the equality in Eq. (5.2) holds for a correctly assumed geometry (and hence μ). A redundant planes cost function c_{RP} can thus be derived

which reaches a minimum for the correctly estimated panel orientation μ :

$$c_{RP} = \sqrt{\sum_{n=0}^{N-1} \sum_{\mu=-\pi/2}^{\pi/2} \sum_{l=-L_{\max}}^{L_{\max}} (g_3(\lambda_n, \mu, l) - g_3(\lambda_{\hat{n}}, \mu, l))^2} \quad (5.6)$$

In the next section, modifications are presented to make c_{RP} more robust against truncation.

5.3.2 Truncation weighting

In the presence of noise and moderate truncation in the acquisitions, minimizing the cost function c_{RP} in Eq. (5.6) has been reported to still provide a good indication for estimating parameters of the acquisition geometry in Cone Beam CT [?]. However, in chest TS, substantial truncation of the object is present in the projections both in the horizontal and vertical direction, as illustrated in Fig. 5.9.

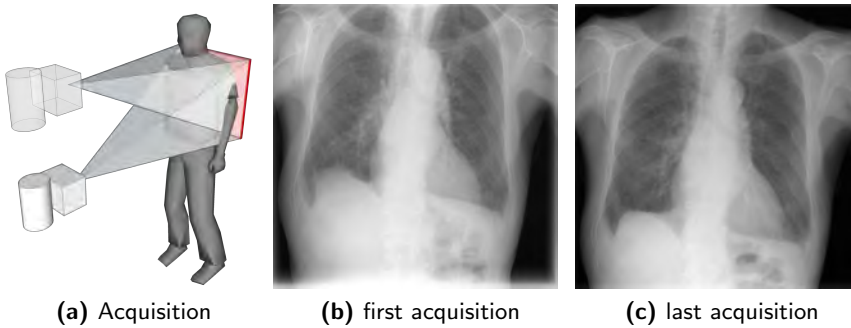


Figure 5.9: (a) Tomosynthesis (TS) acquisition with vertically moving X-ray source and fixed flat panel detector in red (b) first TS acquisition image (c) last acquisition image shows less information from the abdomen and more information from the neck region, due to the vertical truncation. Note also the horizontal truncation of the arms (for more obese patients also the sides of the thorax might be truncated horizontally).

If the X-ray source moves on a linear path with a very small angle μ relative to the detector, the largest inconsistencies between the projections can intuitively be expected to be at the top and bottom regions of the projections as certain parts of the patient will not be imaged, depending on the acquisition angle of the tube. Intuitively, the horizontal truncation would cause less inconsistencies. In previous work, a weighting function was therefore derived to reduce the weight in the cost

function c_{RP} of pixels that were suspected to contain information that was not present in all projections [?].

However, Eq. (5.4) is very sensitive for pixels near the upright image edges, even if an object would have been imaged that fitted perfectly on the detector without horizontal truncation. A small deviation from 0 in μ would cause a large part of the image pixels in the image border to fall off the intersection with the plane Ω , causing a large discontinuity in g_3 and thus making the entire cost function c_{RP} unstable.

Therefore, we propose to use a truncation filter which gradually reduces the weight of the pixels near the horizontal image borders (Fig. 5.10), with w the relative width of the left and right regions of the image where the weight is reduced using a Gaussian function. The same filter is also proposed to compensate vertical truncation.

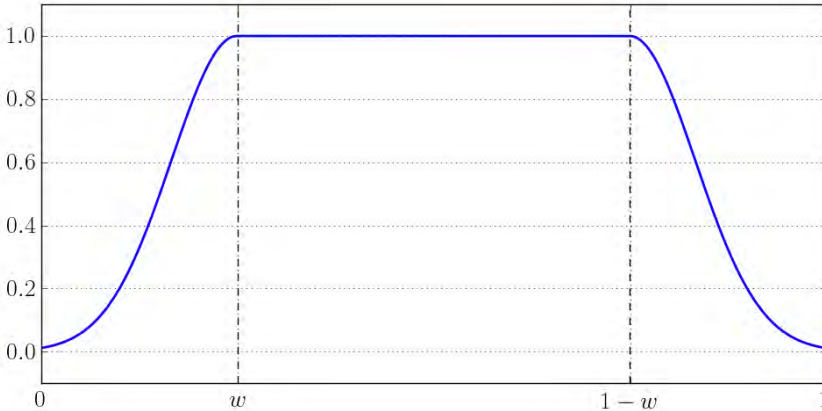


Figure 5.10: To reduce the impact of pixels near the edge of the projections on the cost function, a weighting functions is applied. In the regions of relative width w , weights are increased from 0 to 1 according to a Gaussian distribution with $3\sigma = w$.

5.3.3 Robust cost function for linear tube motion

In case of linear source motion along a path S , the plane Ω intersects all source positions $s(\lambda_i)$ simultaneously, with $i \in [0..N - 1]$. Moreover, the detector remains fixed throughout the entire acquisition in tomosynthesis. The epipolar redundancy of Eq. (5.2) can thus be generalized to

$$g_3(\lambda_i, \mu, l) = g_3(\lambda_j, \mu, l) \quad (5.7)$$

with $0 \leq i < j < N$. The cost function c_{RPL} for linear source motion can be written as

$$c_{RPL}(\mu) = \sum_l \sum_{i=0}^N (g_3(\lambda_i, \mu, l) - \bar{g}_3(\mu, l))^2 \quad (5.8)$$

with $\bar{g}_3(\mu, l) \equiv \frac{1}{N} \sum_n g_3(\lambda_n, \mu, l)$.

5.4 Experiments

In a first series of experiments, the presented method was evaluated on the XCAT phantom[?]. Subsequently, experimental projections were acquired of an anthropomorphic phantom (Humanoid Systems, Carson, USA) with a tomosynthesis modality.

5.4.1 XCAT simulations

A chest tomosynthesis exam was simulated using the XCAT [?] phantom. The ASTRA [?] toolbox was used to compute 11 projections of the XCAT phantom with a source image distance of 120 cm and a linear X-ray tube motion path of 20 cm. The first and last projection image are displayed in Fig. 5.11. Detector size was set to 360×420 pixels of 1 mm size. Moderate Poisson noise was added to the projections, corresponding to an unattenuated photon count $I_0 = 10^5$. The detector was placed at a relative rotation of $\mu_0 = 10^\circ$ with the motion path of the X-ray tube. Experiments were performed to estimate this simulated detector rotation.

The error ϵ on the estimation of the detector orientation angle μ can be written as

$$\epsilon = \mu_0 - \arg \min_{\mu} c_{RPL}(\mu)$$

The maximum achievable accuracy of the estimation is related to the detector size. In Eq. (5.4), line integrals are computed of the projection images along rays with orientation μ . The maximum accuracy Δ is defined as the angle increment for which a rays passes through a neighboring pixel at the edge of the image: $\Delta = \tan^{-1}(1/210) = 0.27^\circ$.

In a first experiment, the effect of the truncation filtering as described in section 5.3.2 was studied. Without truncation filtering, c_{RPL} reached a minimal value for $\mu = 12.7^\circ$ which is well above the true rotation angle of the detector (Fig. 5.12a). Subsequently, the use of the proposed truncation filtering was studied. Gaussian truncation filters were used with varying values w .

Despite vertical truncation causing the largest data inconsistencies between the projections, c_{RPL} does not reach a minimal value around 10° if only vertical

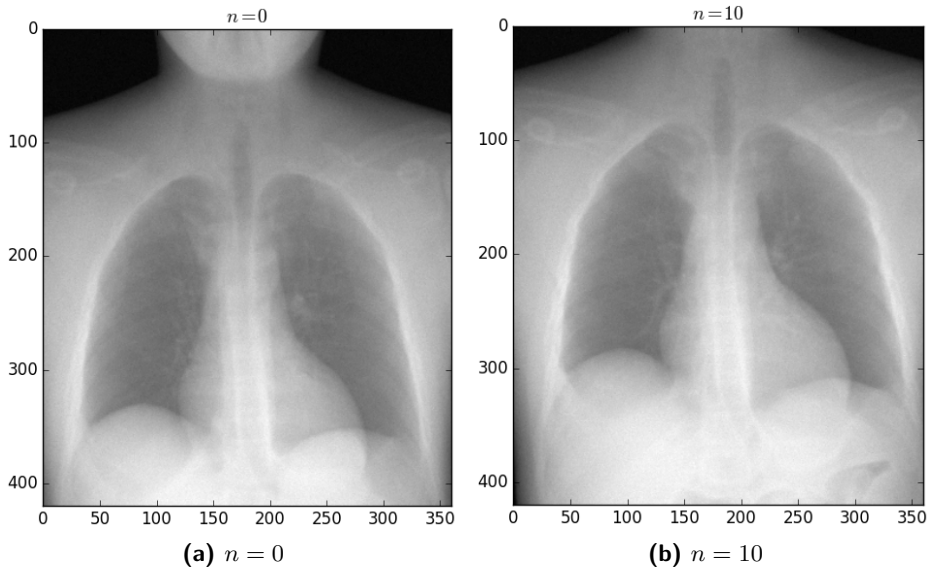


Figure 5.11: First (a) and last (b) simulated XCAT projection.

filtering is applied (Fig. 5.12b). However, horizontal filtering causes the minimum of c_{RPL} to move towards 10° for filter widths $w > 0.10$ (Fig. 5.12c). Combining both horizontal and vertical filters more or less produces the same results, confirming the need for horizontal filtering despite the mainly vertical truncation inconsistencies (Fig. 5.12d).

The estimation errors are displayed in Fig. 5.13. Truncation filters along horizontal and both directions produce a stable estimated angle within the maximal accuracy of the experiment, for filter widths $w > 0.10$. Vertical filtering only does not result in a correct estimation of the rotation angle μ .

5.4.2 Experimental data

To evaluate the effect of the correction of the relative detector orientation, experimental tomosynthesis projections were acquired of an anthropomorphic phantom. Corrected and uncorrected reconstructions were computed with 45 iterations of the Simultaneous Algebraic Reconstruction Technique (SIRT) and compared visually. A motorized X-ray modality was used to acquire 66 projection images using a flat panel detector of 2208×2668 pixels of $160\mu m$ width. The first and last image of the acquisition are displayed in Fig. 5.14. The X-ray tube moved on an arc above the detector center with a radius of 148cm along the longitudinal axis,

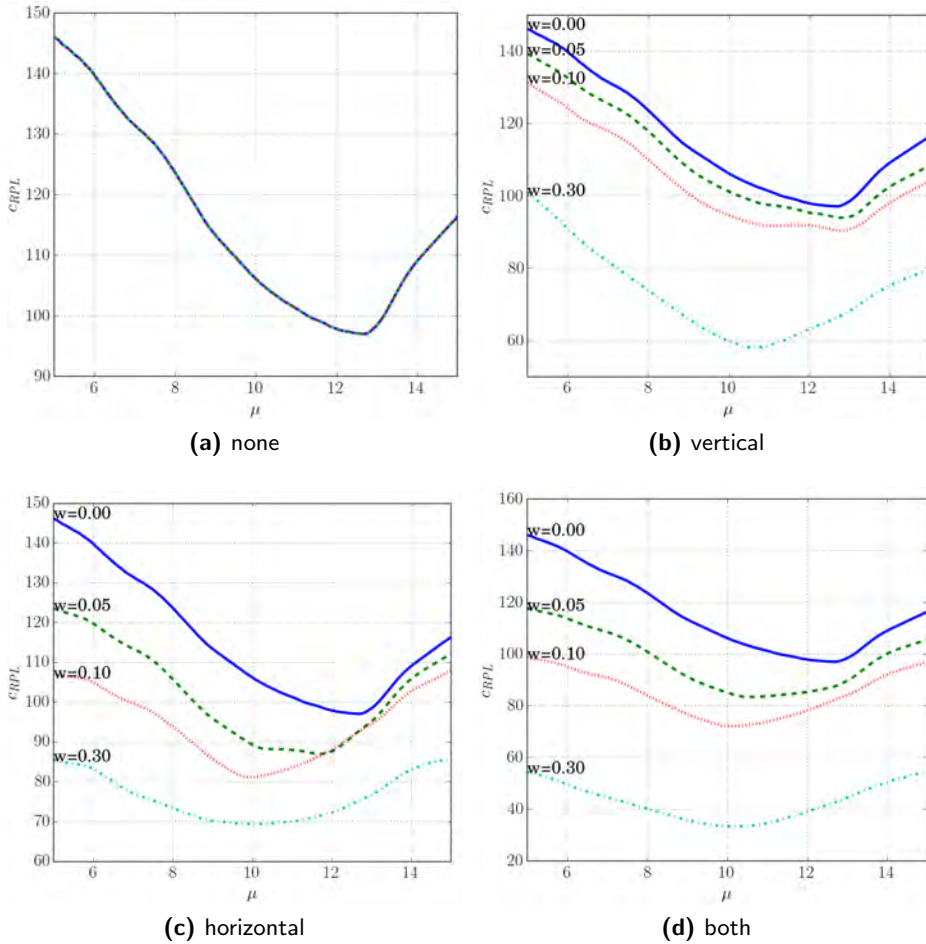


Figure 5.12: Cost function c_{RPL} for estimated detector angle μ (true orientation = 10°). (a) c_{RPL} without truncation filtering (b) c_{RPL} with vertical truncation filtering, for different filter widths w (c) c_{RPL} with horizontal truncation filtering (d) c_{RPL} using both horizontal and vertical truncation filtering.

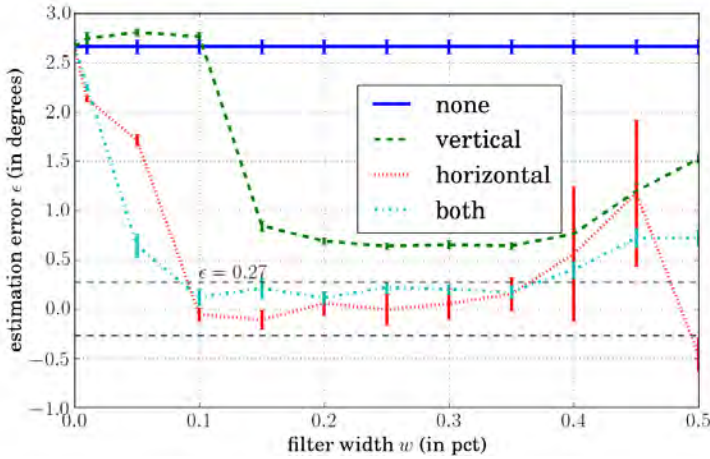


Figure 5.13: Error on estimated detector orientation angle (in degrees) for different truncation filter directions and filter widths w .

as illustrated by the white arrow. Due to X-ray beam collimation, regions near the left, right and bottom edges of the projections contained unexposed pixels and were therefore cropped as illustrated by the red dashed lines. Projection angles were distributed equiangularly from -20° to 21° . The cost function c_{RPL} reached a minimum for $\mu = 0.57^\circ$. The striping artifacts and geometrical distortions in the uncorrected reconstruction (Fig. 5.15a) are not present anymore in the corrected reconstruction (Fig. 5.15b).

5.5 Discussion

The experiments show that the optimal width of the truncation filter is primarily depending on the orientation angle of the detector and the range around which the function g_2 is computed.

With filter widths $w > 0.35$, the cost function becomes unstable. A possible explanation could be that more than 70% of the projections has been weighted down, leaving too little useful information in the projections to compute a cost function robustly.

In the experimental setup, the X-ray tube moved on an arc in stead of a linear path, as assumed in the robust cost function c_{RPL} of Section 5.3.3. No plane Ω could therefore be fitted exactly through all the tube positions, for all intersection

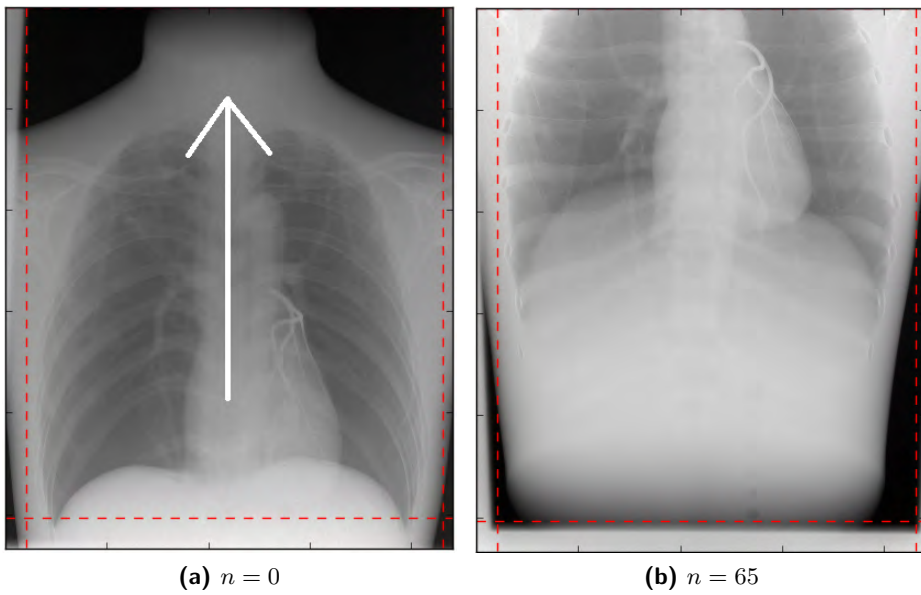


Figure 5.14: First (a) and last (b) image of the tomosynthesis acquisition of the anthropomorphic phantom. The red dashed lines indicate border regions with incomplete radiation due to X-ray beam collimation. The white arrow indicates the path of the X-ray tube.

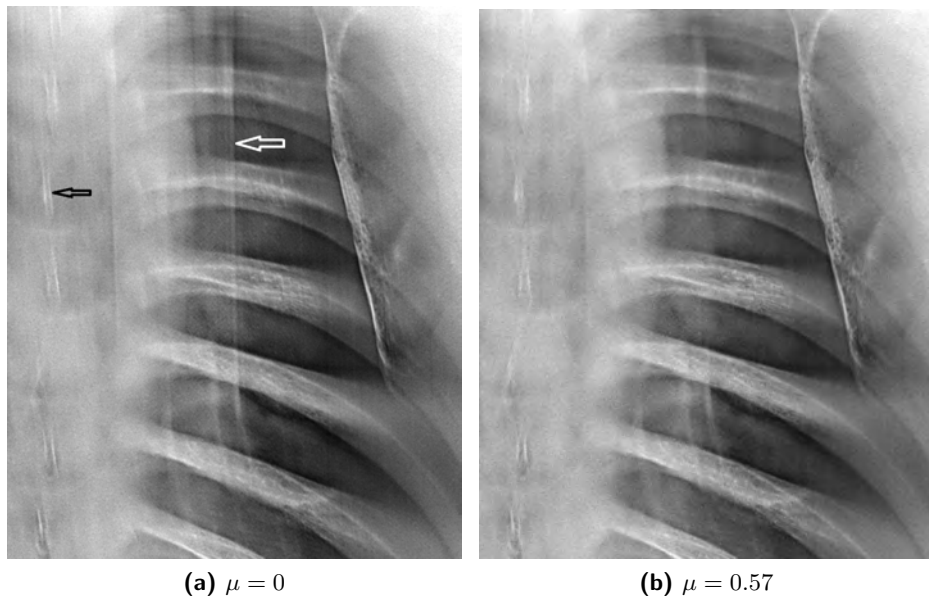


Figure 5.15: 5.15a cropped region of a slice of the tomosynthesis reconstruction of the anthropomorphic phantom, without correction of the acquisition geometry. The white arrow shows a large stripe artifact. The black arrow shows a distorted representation of the vertebrae. 5.15b The same slice, corrected for a detector rotation $\mu = 0.57^\circ$. Note the absence of the stripes and geometrical distortions.

lines with the detector. Nevertheless, the cost function c_{RPL} still showed a clear minimum around 0.57° , which improved reconstruction quality substantially.

5.6 Conclusion

In this work, truncation filtering was presented to increase the performance of the epipolar consistency conditions (ECC) for estimating the relative detector orientation in chest tomosynthesis. Corrected reconstructions showed substantial increase in reconstruction quality and reduction of striping artifacts and geometrical distortions.

6

Conclusions

Chest tomosynthesis (CTS) has been used in clinical practice for more than a decade. CTS has shown to improve detection of lung nodules and various other abnormalities in the chest compared to a standard chest X-ray (CXR) exam. However, whereas a portable modality is on the market for a bedside CXR, a bedside CTS modality is not available yet.

In this work, attempts were made to facilitate the transfer of CTS out of the dedicated X-ray rooms onto a mobile X-ray modality, which could be used in other departments in the hospital such as the Emergency Rooms or Intensive Care Units.

Chapter 2 - Limited view reconstruction

A reduction of the number of views would simplify the workflow and reduce the risk of radiation exposure for other patients and medical staff. In this Chapter, a classical method based on Total Variation (TV) regularization was evaluated, to deal with limited view reconstruction in chest tomosynthesis. Although good results were obtained for CT imaging, TV seems not to be ideally suited to reduce the ringing and streak artifacts that are caused by insufficient angular sampling in chest tomosynthesis.

Chapter 3 - Continuous tomosynthesis

In this Chapter, an entirely different approach was taken to reduce the artifacts caused by insufficient angular sampling. Projections were acquired in a continuous mode, i.e. with a continuously moving and radiating X-ray source, and the motion was modeled in the reconstruction algorithm (ARTIC). The resolution of the reconstructed images improved near the center of the rotation, and hence the method offers a trade off between number of projections and relative size of the central region with good reconstruction quality. A simulation was performed with a tomosynthesis system in a table, in which the detector and X-ray source move in

CHAPTER 6. CONCLUSIONS

opposite directions and hence the rotation center could be located in the center of the patient. ARTIC could not be evaluated on real tomosynthesis exams yet, because it would require changes to the panel readout electronics which was outside the scope of this work.

On the other hand, in some existing imaging techniques such as synchrotron imaging, projections are already acquired in a continuous mode. The motion is typically ignored or kept small enough to avoid artifacts in the reconstructions. Using ARTIC, the motion could be modeled and resulted in improved image quality compared to the regular reconstructions.

Chapter 4 - Mobile chest tomosynthesis in the ICU

In this Chapter, preliminary simulations were made of mobile CTS in an Intensive Care Unit. Whereas other 3D X-ray imaging techniques require transport of the patient to a CT or MRI modality, a mobile TS exam can be performed bedside, with a motorized mobile device for plain X-ray imaging. Clinical examples were presented in which mobile CTS offers increased diagnostic value compared to a regular bedside chest X-ray exam. The simulations suggest a protocol with only 15 projection images, taken over a distance of 14cm to minimize the risk of collisions. The mobile CTS projection images were simulated with 0.1mAs instead of the typical 1mAs of the bedside CXR, leading to a total effective dose of 0.03mSv or 1.5 times the dose of a bedside CXR. A radiation dose comparable to the CXR is critical for the mobile CTS to become clinically accepted. Future experiments with animals and eventually human cadavres will further have to confirm that the proposed dose is sufficient for adequately performing the CTS.

A second technical challenge in performing the CTS exam is keeping the motion (due to patient breathing) under control, as the motion leads to artifacts in the reconstruction. In the proposed mobile CTS protocol, only 15 images are taken which can be realised in less than 3 seconds, hence reducing the risk of patient motion.

Chapter 5 - Geometry parameter estimation

Chest tomosynthesis requires a controlled mechanical motion of the X-ray source. In order to acquire projection images from different angles, the X-ray source on the mobile unit must be motorized to enable efficient and ergonomic motion of the tube. Designing such a motorization should be possible, although reconstruction algorithms require high accuracy of the positioning information, which might still be challenging for sensors to capture with sufficient precision. If the combination of mechanical design and electronic sensors does not deliver the positions of the X-ray source and detector with sufficient accuracy, they can be derived with algorithms

as presented in this Chapter.

A

List of common abbreviations and symbols

Common symbols

i	$\in \{1, \dots, m\}$	Indexing variable for data in the projection domain.
j	$\in \{1, \dots, n\}$	Indexing variable for data in the reconstruction domain.
k	$\in \mathbb{N}$	Iteration number.
\mathcal{R}	$:\mathbb{R} \times \mathbb{R} \rightarrow \mathbb{R}$	Radon transform.

B

Scientific contribution

Journal articles

- Wim van Aarle, Willem Jan Palenstijn, Jeroen Cant, Eline Janssens, Folkert Bleichrodt, Andrei Dabravolski, Jan De Beenhouwer, K. Joost Batenburg, Jan Sijbers “*Fast and Flexible X-ray Tomography Using the ASTRA Toolbox*”, Optics Express, vol 24, no.22, 25129-25147, 2016
- Jeroen Cant, Gert Behiels, Jan Sijbers, “*Modeling blurring effects due to continuous gantry rotation: application to region of interest tomography*”, Medical Physics, vol.42, no.5, pp. 2709-2717, May 2015.

Patents

- Jeroen Cant, Jan Sijbers, “*Method and system for correcting geometric misalignment during image reconstruction in chest tomosynthesis*”, EP16173767.1, June 2016.
- Jeroen Cant, Walter Exelmans, “*Display of depth location of computed tomography slice images relative to an object to be imaged*”, EP15175174.0, July 2015.
- Jeroen Cant, Jan Sijbers, “*Computerized tomographic image exposure and reconstruction method*”, EP14167902.7, May 2014.

Conference proceedings (extended abstract)

- Jeroen Cant, Gert Behiels, Jan Sijbers, “*Automatic geometric calibration of chest tomosynthesis using data consistency conditions*”, The fourth international

APPENDIX B. SCIENTIFIC CONTRIBUTION

- conference on image formation in X-ray computed tomography, pp. 161-164, Bamberg, DE, July 2016.
- Jeroen Cant, Gert Behiels, Jan Sijbers, “*Continuous digital laminography*”, International Conference on Industrial Computed Tomography (ICT), pp. 84-85, Wels, Austria, February 2016
 - Wim van Aarle, Jeroen Cant, Jan De Beenhouwer, Jan Sijbers, “*Discrete tomographic reconstruction from deliberately motion blurred X-ray projections*”, International Conference on Industrial Computed Tomography (ICT), pp. 77-79, Wels, Austria, February 2016
 - Jeroen Cant, Willem Jan Palenstijn, Gert Behiels, Jan Sijbers, “*Tomographic image reconstruction from continuous projections*”, The third international conference on image formation in X-ray computed tomography, pp. 295-298, Utah, USA, July 2014.

Presentations without Proceedings

- Jeroen Cant, “*Continuous projections: from chest tomosynthesis to synchrotron imaging*”, International Workshop on Industrial Tomography, Antwerp, Belgium, November 2015
- Jeroen Cant, “*Jeroen Cant on IWT Baekeland*”, iMinds Researchers in Residence Infosession, Brussels, Belgium, November 2014
- Jeroen Cant, “*Introduction to chest tomosynthesis*”, Dag van de Wetenschap @Agfa HealthCare, Mortsels, Belgium, November 2012

